Centriolar satellites assemble via a hierarchical pathway driven by PCM1 multimerization

Efe Begar[1], Ece Seyrek[1], Selin Yilmaz-Karaoglu[1], Melis D. Arslanhan[1], Ezgi Odabasi[1], Elif Nur Firat-Karalar[1,2]

[1]Department of Molecular Biology and Genetics, Koç University, Istanbul, Turkey 34450

[2]School of Medicine, Koç University, Istanbul, Turkey 34450

Corresponding Author:

Elif Nur Firat-Karalar

Department of Molecular Biology and Genetics

Koç University

Tel: (212) 3381677

E-mail: ekaralar@ku.edu.tr

eTOC summary: Begar et al. show that PCM1 multimerization nucleates centriolar satellite assembly and drives stepwise client recruitment. They further show that disrupting satellite homeostasis impairs ciliary signaling and mitotic progression. Together, these findings reveal how this membrane-less organelle forms and remodels.

Abstract

Centriolar satellites (CS) are ubiquitous membrane-less organelles with diverse functions and links to developmental and neuronal diseases. However, the molecular principles governing their assembly and regulation remain poorly understood. To

address this, we developed cellular and *in vitro* biogenesis assays that enable spatiotemporal quantification of CS granule properties during assembly, remodeling and maintenance. Using these tools, we show that CS assemble via a hierarchical pathway initiated by PCM1 scaffold formation and followed by client recruitment. PCM1 intrinsically assembles into granules through multimerization, a process modulated by the cytoskeleton. High-resolution imaging revealed that PCM1 and its clients occupy distinct subdomains with different compositions and dynamics. Perturbing PCM1 multimerization impaired ciliary signaling and mitotic progression, underscoring its functional importance. Together, these findings define the molecular basis of CS biogenesis, establish tools to probe CS regulation, and provide a framework for understanding how CS deregulation contributes to disease. More broadly, these may extend to other membrane-less organelles and help explain their specificity and plasticity.

Introduction

The dynamic organization of the cytoplasm through membrane-less organelles is an emerging mechanism for spatiotemporal control of cellular functions essential for development and physiology (Banani et al., 2017, Hyman et al., 2014, Li et al., 2024, Woodruff et al., 2018). Organelles such as stress granules, P-bodies, and germ granules form when scaffolding proteins multimerize to create structures that concentrate macromolecules required for their functions (Gomes and Shorter, 2019, Li et al., 2012). These organelles rapidly assemble, disassemble and remodel in response

to intrinsic and extrinsic stimuli, enabling cells to sense and adapt to changes in their environment. However, the absence of a delimiting membrane poses challenges in regulating size, composition, dynamics, and function.

Centriolar satellites (CS) are ubiquitous membrane-less organelles marked by the scaffolding protein Pericentriolar Material-1 (PCM1), which is essential for their assembly (Begar et al., 2024, Hall et al., 2023, Kubo et al., 1999, Odabasi et al., 2019, Wang et al., 2016). They were first discovered in epithelial cells as ~100 nm PCM1-marked granules that cluster and move around the centrosomes in a microtubule-dependent manner (Kubo et al., 1999). They function as a membrane-less trafficking pathway that stores, modifies, and transports proteins to structures such as centrosomes, cilia, and autophagosomes (Aydin et al., 2020, Joachim et al., 2017, Lopes et al., 2011, Odabasi et al., 2019, Wang et al., 2016). PCM1 interacts with over 200 proteins, collectively referred to as clients, some of which are mutated in developmental and neurodegenerative disorders (Aydin et al., 2020, Gheiratmand et al., 2019, Gupta et al., 2015, Quarantotti et al., 2019). Through these activities, CS regulate diverse cellular processes, including cell signaling (e.g., Hedgehog), cell division, motility, stress responses, proteostasis, and neurogenesis (Aydin et al., 2020, Begar et al., 2024, Hall et al., 2023, Odabasi et al., 2019, Wang et al., 2016, Zhao et al., 2021). Consistent with these roles, $PCM1^{-/-}$ mice exhibit developmental defects and psychomotor and cognitive abnormalities, mirroring those observed in ciliopathies and schizophrenia (Hall et al., 2023, Monroe et al., 2020). These findings highlight CS as critical regulators of development and differentiation.

Although defined by PCM1, CS are highly heterogenous across cell types and states (Gheiratmand et al., 2019, Kubo and Tsukita, 2003, Odabasi et al., 2020, Prosser and Pelletier, 2020). In multiciliated epithelial cells, they appear as granules ranging from 1-6 μm, while in myotubes, they form a matrix surrounding the nuclear envelope, and in oocytes, they are part of a liquid-like spindle domain (So et al., 2019, Sorokin, 1968, Srsen et al., 2009, Zhao et al., 2021). CS also remodel dynamically in response to diverse stimuli. They disassemble during mitosis and reassemble upon mitotic exit (Dammermann and Merdes, 2002, Odabasi et al., 2020), and their size and composition change during primary cilium assembly and under cellular stress (Nachury et al., 2007, Odabasi et al., 2023, Tollenaere et al., 2015a, Villumsen et al., 2013). In addition, individual CS granules within the same cell differ in size and composition (Firat-Karalar et al., 2014, Gheiratmand et al., 2019). This intercellular and intracellular heterogeneity reflects their plastic and adaptive nature.

Despite their broad significance, the mechanisms underlying CS assembly, and homeostasis remain poorly understood. In particular, how PCM1 and its clients assemble into functional CS granules with defined size, number, architecture and biochemical properties is unknown. Previous studies provided initial evidence that PCM1 acts as a scaffold, and domain analyses showed that its N-terminal half, which contains two self-association domains, can form granules in cells, whereas the C-terminal half cannot (Kubo et al., 1999). These observations implicated PCM1 multimerization in scaffold assembly, but how this property drives CS formation and how it is regulated in cells remain unclear. Moreover, the heterogeneity and dynamic remodeling of CS suggest additional layers of regulation, likely through subdomain organization and regulated client recruitment. Defining these mechanisms requires tools to monitor CS biogenesis step by step with high spatiotemporal resolution, which has been challenging because CS are constitutively present in cells, except during mitosis, and are small relative to the resolution of conventional microscopy.

To overcome these challenges, we developed cellular and *in vitro* CS biogenesis assays that enable spatiotemporal analysis of the compositional, morphological and dynamic properties of CS granules throughout biogenesis and maintenance. Using these assays, we show that CS assemble through a hierarchical pathway initiated by PCM1 multimerization and followed by client recruitment. We further show that microtubule interactions regulate CS properties, and that perturbing CS granule properties impairs Hedgehog pathway activation and mitotic progression. Together, our findings provide mechanistic insight into CS biogenesis and heterogeneity, introduce new tools to probe their regulation, and establish a framework for understanding how CS contribute to development and disease.

Results

Cellular reconstitution reveals PCM1 multimerization in granule assembly and regulation

A first step in elucidating CS assembly mechanisms is to define the role of PCM1, a 2024 amino acid protein enriched in IDRs and containing two self-association domains (Fig. 1A) (Begar et al., 2024). Based on this domain organization, we hypothesized that PCM1 multimerization drives CS scaffold assembly. To test this, we generated GFP fusions of full-length PCM1 and deletion mutants that included or excluded one or both self-association domains and examined their ability to form

granules, their solubility, and their association with endogenous PCM1. These constructs included PCM1, PCM1-N (1-1200 aa), PCM1-NS (1-700 aa), PCM1-M (700-1200 aa), and PCM1-C (1200-2024 aa) (Fig. 1B).

We first performed cellular reconstitution experiments in HeLa::PCM1 KO cells to identify the PCM1 regions required for granule assembly (Fig. 1C, Fig. S1A). GFP-PCM1 formed granules similar to endogenous PCM1, clustering around centrosomes and, to a lesser extent, throughout the cytoplasm (Fig. 1C). GFP-PCM1-N and GFP-PCM1-M also formed granules, but these were larger and more variable in size than those formed by full-length PCM1 (Fig. 1C, 1D, Fig. S1A). In contrast, GFP-PCM1-NS, despite containing a self-association domain, and GFP-PCM1-C did not form granules in these cells (Fig. 1C, Fig. S1A). Solubility analysis showed that PCM1-M and PCM1-N were less soluble compared to PCM1 and PCM1-C, consistent with their tendency to form larger, irregular granules (Fig. 1E). To assess the influence of endogenous PCM1 on granule formation, we performed similar experiments in wild-type HeLa cells. All constructs behaved similarly except PCM1-NS, which formed granules, likely through multimerization with endogenous PCM1 (Fig. 1C, Fig. S1A). Consistent with this, granules formed by PCM1-N, PCM1-M, and PCM1-NS recruited endogenous PCM1, whereas PCM1-C did not (Fig. S1B).

We next examined the concentration-dependent behavior of PCM1 and its deletion mutants by quantifying the threshold expression levels required for granule formation and how granule properties changed with increasing expression. Using transiently transfected PCM1 KO cells, we measured relative protein concentrations in granules and cytoplasm by fluorescence intensity per volume after 3D reconstruction (Fig. 1F, 1G, S1C) (Jiang et al., 2021). GFP-PCM1 formed granules once it reached a threshold concentration, but these granules dissolved at higher expression levels, indicating regulation of CS size and number (Fig. 1F, 1G). In contrast, once GFP-PCM1-N and GFP-PCM1-M granules formed, they did not dissolve at higher concentrations but instead became larger and brighter (Fig. 1F, 1G). In wild-type cells, we could also estimate a threshold expression level for GFP-PCM1-NS. Relative thresholds differed between full-length PCM1 and the mutants, and between KO and wild-type cells, suggesting that endogenous PCM1 contributes differently to granule formation through multimerization (Fig. S1D, S1E).

Together, these findings support a modular organization of PCM1 in which PCM1-M is the primary multimerization region required for CS granule formation,

whereas PCM1-C modulates granule size, number, and solubility without being essential for assembly.

Manipulation of PCM1 multimerization deregulates CS properties and leads to signaling defects

Having established that PCM1 is modular, with PCM1-M driving multimerization and PCM1-C modulating granule properties, we next asked whether altering PCM1's multimerization state could change CS granule properties and lead to aberrant assembly or disassembly. To manipulate PCM1 multimerization in cells, we adapted a chemically inducible dimerization system using a modified FKBP protein (FKBP-F36V mutant), which dimerizes upon addition of AP20187 (dimerizer) and whose effect can be reversed with AP22542 (washout ligand) (Fig. 2A) (Inobe and Nukina, 2016, Rollins et al., 2000).

To adapt this system for CS, we generated RPE1::PCM1 KO cells stably expressing mNeonGreen (mNG)-PCM1 fused at its C-terminus to FKBP-F36V and compared CS granule number and size in these cells before and after dimerization, and following dimer dissociation (Fig. 2B, 2C). Dimerizer treatment reduced granule number and increased their size, which were reversed by washout ligand, confirming that regulated dimerization can control CS size and number (Fig. 2B, 2C). Live imaging of mNG-PCM1-FKBP after inducing dimerization and its reversal revealed the spatiotemporal dynamics of these changes (Fig. S2A). To probe internal molecular exchange within PCM1 granules after induced dimerization, we performed fluorescence recovery after photobleaching (FRAP) on mNG-PCM1-FKBP granules 2 h or 16 h after dimerizer treatment. Fluorescence recovery was minimal in both conditions, yielding a small mobile fraction of about 5% at both time points (Fig. S2B). Moreover, 1,6-hexanediol treatment (1,6-HD), a small aliphatic alcohol that disrupts weak hydrophobic interactions (Alberti et al., 2019, Itoh et al., 2021), did not measurably change granule number or fluorescence intensity after dimerization (Fig. S2C).

Because this inducible system altered CS size, number and internal molecular mobility, it provided a way to directly examine the functional consequences of disrupting CS regulation. Given well-characterized functions of CS at the cilium in loss-of-function studies (Aydin et al., 2020, Begar et al., 2024, Odabasi et al., 2019, Wang et al., 2016), we asked whether induced dimerization would affect CS functions in cilium assembly and ciliary signaling. Ciliogenesis and cilium length were comparable between control cells and those treated with dimerizer or washout ligand (Fig. S2D-F). However, cilia

formed after dimerizer treatment did not respond efficiently to the Hedgehog agonist SAG, as shown by a significant decrease in ciliary SMO concentration (Fig. 2D, 1E). Importantly, this phenotype was reversed by dissociating the mNG-PCM1-FKBP dimers with the washout ligand (Fig. 2D, 2E). These results demonstrate that manipulating PCM1 multimerization disrupts the formation of functional cilia.

We next examined how inducible PCM1 dimerization affects CS behavior and function during mitosis. In untreated cells, the majority of mNG-PCM1-FKBP granules dissolved upon mitotic entry, whereas granules persisted throughout mitosis in dimerizer treated cells (Fig. 2F, 2G, Video 1). Notably, live imaging revealed heterogeneity in granule organization and distribution. Most cells contained multiple granules of varying sizes that typically partitioned into both daughter cells, whereas a smaller fraction (~9.7% ± 3.67%) formed a single large granule that was often retained in only one daughter cell, resulting in unequal inheritance (Fig. 2G, Video 2). Importantly, population level analyses did not reveal global defects in chromosome segregation or overall cell cycle stage distribution (Fig. S2G, S2H). However, cells in the single granule group exhibited a modest increase in mitotic duration (Fig. 2H, 2I, Video 3, Video 4) and a higher frequency of mitotic defects (Fig. 2H, 2I). These defects typically occurred after spindle formation and were associated with failure to complete anaphase and/or initiate cytokinesis, leading to binucleated cells (Fig. 2H, S2I). Together, these observations suggest that coalescence of PCM1 into a single large granule can compromise mitotic progression.

Development and validation of the *de novo* CS biogenesis assay

To enable spatiotemporal analysis of CS assembly, we developed a *de novo* CS biogenesis assay based on inducible expression of GFP-tagged PCM1 and the granule-forming deletion mutants PCM1-N and PCM1-M in RPE1::PCM1 KO cells. Immunofluorescence after 16 h of induction confirmed formation of PCM1, PCM1-N, and PCM1-M granules (Fig. S3A). Immunoblotting before induction and at 1, 2, 4, 8, and 16 h showed that PCM1 expression increased progressively from 1 h onward (Fig. S3B-D). Full-length GFP-PCM1 reached levels comparable to endogenous PCM1 by 8 h, whereas PCM1-N and PCM1-M accumulated to higher steady-state levels by 16 h, reaching ~4-fold and ~8.5-fold endogenous PCM1 levels, respectively (Fig. S3B-D).

We next examined the extent to which the *de novo* formed granules by GFP-tagged PCM1, PCM1-N and PCM1-M were functional. To this end, we performed phenotypic rescue experiments for CS-linked ciliary functions, including cilium assembly

and length, recruitment of IFT88 to the basal body and cilium, and Hedgehog pathway activation after SAG stimulation (Aydin et al., 2020, Begar et al., 2024, Odabasi et al., 2019, Wang et al., 2016). Induced expression of PCM1 rescued defects in ciliogenesis efficiency, cilium length, and ciliary IFT88 and SMO recruitment in PCM1 KO cells, thereby validating that the *de novo* assay recapitulates physiological CS functions (Fig. S4A-G). Expression of PCM1-N also rescued ciliogenesis but only partially restored cilium length and IFT88/SMO recruitment, indicating that PCM1-N granules are partially functional (Fig. S4A-G). In contrast, GFP-PCM1-M expression failed to rescue any of the ciliary phenotypes, indicating that granule formation alone is not sufficient to support CS-dependent ciliary functions (Fig. S4A-C). Taken together, these results validate the *de novo* biogenesis assay as a tool to examine CS assembly.

Spatiotemporal dynamics of PCM1 scaffold formation during CS biogenesis

CS may assemble either stochastically or through an ordered pathway in which a scaffold forms first and then recruits clients in a regulated manner. The controlled granule properties and heterogeneity of CS are more consistent with the latter model (Begar et al., 2024, Prosser and Pelletier, 2020). To test this, we examined PCM1 scaffold assembly using the *de novo* assay and complemented this analysis with mitotic remodeling, a physiological context in which CS disassemble and reassemble during the cell cycle (Rai et al., 2018). For quantification, we developed an image-analysis pipeline that measured CS number, volume, intensity and distance from the centrosome (Fig. S5A).

Using the *de novo* CS biogenesis assay, we first performed fixed 3D confocal imaging to quantify PCM1 scaffold properties before and after doxycycline (dox) induction (Fig. 3A, 3B). Cells were imaged at 10, 20 and 30 minutes, and 1, 2, 4, 6 and 16 hours post-induction. Staining for the centriole marker centrin showed that GFP-PCM1, GFP-PCM1-N, and GFP-PCM1-M granules initially appeared at or near the centrosome. Over time, additional granules of variable size formed in the cytoplasm and gradually clustered around centrosomes, as reflected by decreasing average distance to centrioles. Notably, GFP-PCM1 granules were smaller, more uniform, and more numerous, whereas PCM1-N and PCM1-M formed fewer, larger, and more heterogeneous granules (Fig. 3A, 3B).

We next performed time-lapse confocal imaging to define the assembly dynamics of GFP-PCM1, GFP-PCM1-N, and GFP-PCM1-M. Analysis of 3D movies confirmed the fixed-cell observations and revealed three phases of PCM1 assembly (Fig. 3C, 3D,

Video 5, Video 6, Video 7). In cells expressing PCM1, an initiation phase (10–30 min, typically at centrosomes) was followed by a growth phase (30 min–2 h, when granule number, size, and intensity increased), and then by a steady-state phase (after ~2 h, when granule properties plateaued with modest variation) (Fig. 3C, 3D). PCM1-N and PCM1-M granules also underwent initiation and growth but did not reach a steady state; instead, their size and intensity continued to increase while their numbers decreased, consistent with fusion events. Plotting granule volume against number confirmed these three phases and showed that PCM1 formed many smaller granules, while PCM1-N and PCM1-M formed fewer, larger ones (Fig. 3E). These analyses define a stepwise process of initiation, growth, and steady state during CS biogenesis and show that full-length PCM1 and its truncations generate scaffolds with distinct properties.

We next analyzed CS remodeling during mitosis. Live-cell imaging of GFP-PCM1, GFP-PCM1-N, and GFP-PCM1-M granules with SIR-tubulin labeling revealed a rapid decline in granule number, volume, and intensity at mitotic entry, consistent with disassembly (Fig. S5B, S5C, Video 8, Video 9, Video 10). During cytokinesis, prominent PCM1 granules reappeared around centrosomes of daughter cells, followed by gradual accumulation of cytoplasmic granules, marking CS reassembly. These dynamics paralleled those observed in the *de novo* biogenesis assay.

Dynamic behavior of PCM1 scaffold during CS biogenesis

We next examined whether PCM1 scaffolds, once formed, maintain dynamic exchange or instead undergo a gradual reduction in dynamics, as reported for other membrane-less structures such as RNP and pericentrin granules (Bose et al., 2022, Jiang et al., 2021, Patel et al., 2015). Understanding this distinction is important, because the properties of membrane-less organelles often depend on whether their components exchange continuously or are retained in a more static configuration.

To assess the internal dynamic properties of PCM1 granules, we performed FRAP analysis. Because the diffraction-limited size of full-length PCM1 granules prevented reliable measurements, we first examined PCM1-N and PCM1-M. Time-dependent FRAP showed progressively reduced mobile fractions and slower recovery, indicating that these granules gradually lose dynamic exchange (Fig. 4A). Live imaging of GFP-PCM1-N granules revealed occasional fusion and splitting events, but most interactions were transient “kiss-and-run” contacts in which granules briefly touched and then separated (Fig. 4B). This behavior supports the idea that most PCM1-N granules become less dynamic after assembly.

To extend these findings to full-length PCM1, we examined granules at steady state using chemical and enzymatic perturbations. 1,6-HD treatment reduced the total volume and intensity of PCM1 granules, indicating that a small fraction remains sensitive and dynamic (Fig. 4C, 4D). However, the majority of granules persisted, suggesting that most adopt a non-dynamic state after assembly. As a control, 1,6-HD almost completely dissolved stress granules marked by G3BP1, confirming the sensitivity of the assay (Fig. 4E) (Wheeler et al., 2016, Yang et al., 2020, Zhang et al., 2019). We also treated cells with RNase, as RNA has recently been identified as a CS component and RNA-dependent interactions often contribute to membrane-less organelle assembly (Banani et al., 2017, Hyman et al., 2014). PCM1 granules remained intact, whereas stress granules dissolved (Fig. 4C-E). Finally, to determine how PCM1 dynamics change during biogenesis, we compared 1,6-HD sensitivity at early (2 h) and late (16 h) induction time points (Fig. 4F). PCM1 granules were more sensitive at 2 h, with larger reductions in number and volume than at 16 h, indicating that they become progressively less responsive to disruption as they mature (Fig. 4G, 4H).

Together, FRAP, live imaging and chemical perturbation assays show that while a minor fraction of PCM1 granules retains dynamic properties, the majority progressively adopt a predominantly non-dynamic state during biogenesis.

Clients are recruited hierarchically to the PCM1 scaffold

Having established that PCM1 initiates CS scaffold assembly, we next asked how client proteins are incorporated. One possibility is that PCM1 first forms a scaffold and then recruits clients stepwise to generate functional CS granules with distinct composition. Alternatively, the scaffold and clients may co-assemble from the beginning. To distinguish between these possibilities, we examined the timing of client recruitment relative to PCM1 scaffold formation.

Using the *de novo* biogenesis assay with GFP-PCM1, we fixed cells at defined time points after induction, stained clients with specific antibodies and quantified their colocalization with PCM1 (Fig. 5A). We selected nine established CS clients involved in ciliogenesis, centriole duplication, and microtubule organization, several of which were also linked to human disease including microcephaly, ciliopathies, and oral–facial–digital syndrome (Begar et al., 2024, Chevrier et al., 2016, Firat-Karalar et al., 2014, Kim et al., 2008, Kim et al., 2012, Lopes et al., 2011, Wang et al., 2016). We limited our analysis to proteins for which available antibodies reliably detected the CS pool, in addition to their centrosomal pool.

To quantify recruitment, we calculated Pearson correlation coefficients (PCC) between PCM1 and each client before induction and at 10 min, 30 min, 2 h, 8 h, and 16 h post-induction (Fig. 5A). Control measurements established the detection range. PCM1 stained with Alexa 488- and Alexa 568-conjugated secondary antibodies gave a PCC of 0.89 (upper limit), whereas PCM1 and the non-CS protein G3BP1 gave a PCC of 0.03 (lower limit). For each client, we plotted PCC values over time (Fig. 5B) and compared changes between consecutive time points to infer relative recruitment order (Fig. 5C).

No clients were detectable at PCM1 granules at 10 min, supporting that CS granule formation is driven by PCM1 and does not involve immediate co-assembly with clients (Fig. 5A). By 30 min, several clients including CEP131, CEP290, MIB1, OFD1, and PIBF1 could be detected at the PCM1 granules near centrosomes (Fig. 5A-C). Among these, CEP131 consistently showed the strongest correlation, suggesting it is among the earliest recruited clients. By 2 h, all tested clients were detectable at PCM1 granules, although with different PCC levels (Fig. 5B, 5C). Client-PCM1 PCCs increased further at 8 and 16 h, reaching values between 0.3 and 0.6, consistent with intracellular CS compositional heterogeneity (Fig. 5B, 5C). Across time points, CEP131, MIB1, and PIBF1 showed higher colocalization with PCM1; CCDC14, OFD1, KIAA0753, and CEP290 showed intermediate association; and CEP72 and BBS4 consistently showed the lowest. Importantly, even when clients reached similar PCCs at 30 min or 16 h, their recruitment trajectories differed. For example, CEP131 and PIBF1 both reached high PCCs by 16 h but had distinct initial rates of accumulation (Fig. 5B, 5C). Together, these results indicate that client recruitment is progressive and client-specific, contributing to intracellular heterogeneity. Although antibody sensitivity may affect apparent recruitment order, reproducible PCC profiles across replicates supports the conclusion that clients are not incorporated simultaneously but instead associate with PCM1 scaffolds in distinct patterns over time.

To determine how scaffolds formed by different PCM1 domains influence client recruitment, we examined cells expressing GFP-PCM1-N or GFP-PCM1-M at the same time points. Recruitment to PCM1-N largely mirrored that of full-length PCM1 (Fig. S6A–C). Because PCM1-N formed larger granules, additional clients such as ninein, likely below detection threshold with PCM1, were detected at PCM1-N granules. BBS4, which requires the C-terminus of PCM1, was absent from PCM1-N but recruited to full-length PCM1 (Nachury et al., 2007, Wang et al., 2016). Most clients showed higher PCCs with PCM1-N compared to PCM1, consistent with stronger recruitment to larger granules. By

contrast, client recruitment to PCM1-M was highly restricted: only CEP290 localized to PCM1-M granules, and only at later time points (16 h) and in the largest granules, suggesting weak affinity (Fig. S6D). These results indicate that PCM1-M contributes primarily to PCM1 self-association rather than client recruitment, consistent with its inability to restore ciliary defects in PCM1 KO cells (Fig. S4B, S4C).

PCM1 and clients are organized into subdomains within CS granules

Internal organization has been described for several membrane-less organelles, including paraspeckles and the pericentriolar material, where core-shell or layered architectures help coordinate protein function (Mennella et al., 2012, West et al., 2016) . Given the multistep assembly and regulated heterogeneity of CS granules, we hypothesized that they also contain internal subdomains. To test this, we mapped the spatial arrangement of PCM1 and selected clients using ultrastructure expansion microscopy (U-ExM) and structured illumination microscopy (SIM).

First, we analyzed the distribution of different PCM1 domains by U-ExM using antibodies against the N-terminal (1-254 aa), middle (700-1200 aa), and C-terminal (1664-2024 aa) regions of PCM1. We validated antibody specificity using deletion mutants (Fig. S7A-D). U-ExM revealed extensive but incomplete overlap between PCM1-N and PCM1-M. In contrast, PCM1-C showed minimal overlap with either region and localized to a distinct spatial domain. These results show that PCM1 domains occupy partially distinct positions within CS granules (Fig. 6A).

We next examined the relationship between PCM1 scaffold and clients. Using U-ExM in RPE1 (Fig. 6B, 6C) and U2OS (Fig. S7E, S7F) cells, we mapped the localization of OFD1, MIB1, KIAA0753, CEP290, and CEP131 within CS granules. To define the PCM1-occupied volume within CS granules, we combined signals from antibodies recognizing different PCM1 regions, specifically the PCM1-N/M and PCM1-C/M domains. In both cell types, clients were distributed heterogeneously throughout the granule and showed distinct, partially overlapping spatial relationship with the PCM1 scaffold. Pairwise analyses further revealed that clients could occupy separate regions within the same granule, as observed when comparing CEP131 with OFD1, KIAA0753, MIB1 or CEP290 (Fig. 6B, 6C; Fig. S7E, S7F). Even within larger satellite clusters, individual granules remained structurally distinct and maintained this organization. Together, these results show that CS granules exhibit internal spatial organization across different cell types.

To build a quantitative spatial map of client organization, we used larger PCM1-N granules, which reach up to 1 μm in diameter, provide more binding sites, and retain partial functionality during cilium formation and signaling (Fig. S4A-G). RPE1::PCM1 KO cells expressing GFP-PCM1-N were fixed, stained for the nine clients analyzed in the biogenesis assay (Fig. 6D) and imaged by SIM, as the large granule size provided sufficient spatial resolution for quantitative analysis without requiring U-ExM. Because granules increase in size during assembly, we analyzed structures 0.1 to 1 μm to determine when client spatial organization emerges and whether it is maintained during granule growth (Fig. S8A).

GFP-PCM1-N formed spheroidal scaffolds with an internal organization that could be resolved in granules larger than 0.4 μm (Fig. S8A). In smaller granules, PCM1-N and clients were distinguishable, but their relative positions were less clear. We therefore quantified subdomain organization in larger granules by measuring the distance between fluorescence intensity peaks of each client and normalizing it to the PCM1-N diameter (Fig. 6D-F). Using the PCM1 scaffold as a reference (normalized to 1.0), we empirically grouped clients into five spatial zones based on these relative distances. These included an “inner core” (0.5–0.75; PIBF1, CEP131), an “intermediate core” (0.75–0.80; KIAA0753, CCDC14, MIB1), a “core–shell interface” (0.80–0.90; OFD1), a “shell” overlapping with PCM1 (0.90–1.1; CEP290, CEP72), and an “outer shell” extending beyond the scaffold (1.1–1.5; Ninein) (Fig. 6D-F).

To determine when spatial organization emerges during granule growth, we tracked the recruitment of the outer-shell client Ninein over a 16 h induction time course (Fig. S8B). At 30 min, PCM1 scaffolds had assembled but lacked detectable Ninein. By 1 h, Ninein was recruited but had not yet adopted a defined sub-domain compartmentalization, instead localizing close to the inner scaffold rather than forming its characteristic outer shell. By 2 h, however, Ninein established its mature spatial distribution, which was maintained through 16 h despite granule expansion. These data support a stepwise biogenesis model in which initial client binding is followed by establishment of spatial organization that is then maintained as the granule grows.

Together, these analyses suggest that CS granules exhibit a core–shell–patch arrangement in which PCM1 and clients occupy distinct subdomains. While antibody availability and resolution limit the breadth of this analysis, the reproducible localization patterns indicate that CS granules are not homogeneous and suggest a basis for compartmentalization and regulation of client proteins.

CS subdomains differ in client interaction dynamics and composition

The identification of distinct CS subdomains and the predominantly non-dynamic nature of the PCM1 scaffold raised the question of whether scaffold–client interactions differ in their dynamics and whether CS composition remodels in different cellular states. To probe interaction dynamics, we perturbed weak hydrophobic interactions among the scaffold and clients with 1,6-HD. Co-immunoprecipitation showed that the association of CEP131, MIB1, and KIAA0753 with PCM1 decreased after treatment, whereas the PCM1–CEP290 interaction was largely unaffected (Fig. 7A). This suggests that some clients interact with PCM1 more dynamically than others.

We then asked whether these differences contribute to compositional heterogeneity within cells. PCC analysis showed that colocalization of all tested clients with PCM1 decreased after 1,6-HD treatment, but to different extents (Fig. 7B, 7C). CEP131, KIAA0753, OFD1, and CCDC14 showed moderate reductions (30–55%), PIBF1, CEP290, and MIB1 were more strongly affected (60–80%), and CEP72 and BBS4 showed the largest decreases (80–99%). These graded responses likely reflect differences in interaction dynamics. Notably, CEP72 and BBS4 were also the last clients to be recruited during CS biogenesis (Fig. 5), consistent with more transient associations. In contrast, RNase treatment had little effect on client-PCM1 association, except for CEP131, which may partially depend on RNA for recruitment (Fig. 7D).

We next asked whether CS composition remodels in response to specific cellular cues. Comparing unciliated and ciliated RPE1 cells, we found that the colocalization of several positive ciliogenesis regulators (CCDC66, CSPP1, CEP104, and CEP290) with PCM1 was reduced upon ciliation (Frikstad et al., 2019, Kim et al., 2008, Odabasi et al., 2023). In contrast, association of MIB1, a negative regulator of ciliogenesis remained unchanged (Fig. 7E, 7F). This selective reduction suggests that CS may preferentially release positive regulators to function at the newly formed cilium. To test whether this remodeling varies depending on the stimulus, we examined CS under genotoxic stress induced by etoposide treatment, another context known to trigger CS reorganization (Tollenaere et al., 2015b, Villumsen et al., 2013) (Fig. S9A). Etoposide produced a distinct remodeling profile. Although CCDC66 association was again reduced and MIB1 remained unchanged, changes in other clients were more modest than during ciliation, indicating that the pattern and extent of client release differ between conditions (Fig. S9A, S9B). Together, these results suggest that scaffold-client interactions are differentially regulated and that CS adapt their composition to cellular requirements.

This signal-dependent remodeling may also help explain the partial rescue activity of GFP-PCM1-N (Fig. S4). Because GFP-PCM1-N granules are only partially functional in ciliogenesis assays, we asked whether they undergo normal compositional remodeling during cilium formation. In cells expressing GFP-PCM1, colocalization of CEP290 with PCM1 was significantly reduced upon ciliogenesis, whereas MIB1 association remained unchanged (Fig. S9C-F). In contrast, GFP-PCM1-N granules did not show detectable changes in colocalization of either CEP290 or MIB1 upon ciliation (Fig. S9C-F). Thus, unlike full-length PCM1 granules, GFP-PCM1-N granules did not undergo normal client remodeling during ciliogenesis. This defective remodeling, particularly the failure to reduce CEP290 association, may contribute to their limited ability to fully rescue ciliary phenotypes.

In vitro reconstitution reveals scaffold formation, client recruitment and microtubule interaction as intrinsic PCM1 properties

CS functions depend on microtubule-based positioning and transport and selective client recruitment. Our cellular assays showed that PCM1 multimerization drives scaffold assembly and that this scaffold recruits clients during CS biogenesis. To test whether these properties are intrinsic to PCM1 or require additional cellular factors, we performed *in vitro* reconstitution experiments with purified PCM1, clients, and microtubules.

We expressed and purified His-MBP-mNeonGreen-PCM1 (referred to as mNG-PCM1) from insect cells and verified the presence of full-length protein by Coomassie staining, immunoblotting and immunostaining with antibodies specific to its N- and C-terminal regions (Fig. S10A, S10B). These antibodies are bound to labeled distinct regions within the precipitated PCM1 protein, consistent with the modular organization of PCM1 (Fig. S10B). Mass spectrometry confirmed that mNG-PCM1 was the dominant protein in the purified sample (Fig. S10C, S10D, Table S1). Apart from low-abundance tubulin isoforms, consistent with previous reports of PCM1-tubulin interaction, we did not detect enrichment of known centrosomal proteins or microtubule regulators (Yu et al., 2016).

We next tested whether purified PCM1 forms granules under near-physiological buffer conditions. At 1 μM, mNG-PCM1 assembled into spherical granules in a buffer containing 150 mM NaCl (Fig. 8A). This protein concentration approximates intracellular PCM1 levels (~700–900 nM in mammalian cells) (Geiger et al., 2013, Hein et al., 2015, Wang et al., 2015). Notably, the N-terminal mNG tag often showed a spheroidal

distribution, particularly in larger granules, suggesting internal spatial organization (Fig. 8A inset). Increasing PCM1 concentration from 1 to 4 μM increased granule number without significantly changing average granule volume (Fig. 8B, 8C). As a negative control, mNG alone did not form granules (Fig. S10E).

We next asked whether PCM1 granules formed *in vitro* recapitulate two key cellular properties of CS, selective client recruitment and microtubule interaction. To test client recruitment, we used MIB1 because of its established role in CS homeostasis and its characterization in our biogenesis assays (Douanne et al., 2019, Wang et al., 2016) (Fig. S10F). Purified His-MBP–mScarlet–MIB1, added at ~100 nM (reflecting cellular levels) (Geiger et al., 2013, Hein et al., 2015, Wang et al., 2015), could form granules on its own, but it was also selectively incorporated into pre-formed PCM1 granules (Fig. 8D). In contrast, GST–mScarlet was not (Fig. 8D). These results show that PCM1 scaffold can directly and selectively recruit client proteins *in vitro*.

We next tested microtubule interaction, given that CS are transported along microtubules and this is required for their functions (Conkar et al., 2019, Kubo et al., 1999). TIRF microscopy showed that mNG-PCM1 granules bound directly to taxol-stabilized, rhodamine-labeled microtubules immobilized on coverslips (Fig. 8E). In addition, the addition of free fluorescent tubulin to these reactions resulted in its recruitment into mNG-PCM1 granules (Fig. 8F). When mNG-PCM1 was incubated with rhodamine-labeled microtubules in solution, microtubules reorganized into denser bundles with larger PCM1 granules associated along them (Fig. 8G, 8H, S8G, S10H). These granules were larger than PCM1-only controls and often showed spheroidal organization, suggesting that microtubules may promote scaffold assembly (Fig. 8G). Tubulin recruitment into PCM1 granules further supports its role as a CS client.

To determine whether microtubules similarly regulate CS biogenesis in cells, we treated RPE1::PCM1 KO cells expressing GFP-PCM1 with nocodazole. Treated cells had fewer and smaller PCM1 granules with reduced fluorescence intensity and a more dispersed cytoplasmic distribution compared to controls (Fig. 8I, 8J). These effects were strongest at 2 h, with partial recovery by 16 h. Strikingly, in nocodazole-treated cells, scaffold formation was no longer initiated at the centrosome. Instead, PCM1 granules formed stochastically throughout the cytoplasm, suggesting that microtubules help concentrate PCM1 at the centrosome to promote the initial scaffolding event (Fig. S10I).

Discussion

In this study, we combined cellular and *in vitro* assays to define how CS granules assemble. Our findings support a model in which CS assembly begins with PCM1 scaffold formation and is followed by regulated client recruitment. We identify mechanisms that control assembly, show that CS granules are spatially organized into subdomains and link CS granule properties to cellular signaling and mitotic progression. Collectively, these findings provide a framework and a set of tools to study CS homeostasis across biological and disease contexts.

Cellular reconstitution with PCM1 deletion mutants showed that PCM1-M, which contains the second self-association domain, is sufficient for granule formation, whereas the C-terminal region modulates CS properties rather than directly driving assembly. These data support a model in which PCM1 functions as a modular protein, with its C terminus regulating the assembly activity of the N-terminal region, possibly through protein interactions or post-translational modifications. *In vitro* reconstitution and induced dimerization further showed that PCM1 multimerization is sufficient to drive scaffold formation and that its regulation is critical for CS granule properties. Together, these findings identify PCM1 multimerization as a core principle of CS scaffold assembly, similar to other multimerization-driven membrane-less organelles such as stress granules (Yang et al., 2020, Zhang et al., 2019).

The FKBP-based dimerization system allowed us to acutely perturb PCM1 granule properties and directly relate these changes to function. Forced dimerization generated enlarged, less dynamic granules and caused detectable but modest defects in ciliary signaling and mitotic progression. The strongest phenotypes were observed in cells containing a single large granule, suggesting that functional disruption increases with the extent of PCM1 coalescence. The modest and variable nature of these defects may reflect a limitation of the current assay, which induces dimerization but may not drive the degree of coalescence needed to generate fully dysfunctional granules. Higher-valency inducible oligomerization strategies may enable stronger PCM1 coalescence and clarify how altered assembly affects CS function (Kanekura et al., 2022, Yamanaka et al., 2021). Defining the native oligomeric state of PCM1 and its regulatory mechanisms will be important for understanding how CS properties are controlled in cells.

Combining *de novo* biogenesis assays with 3D image analysis revealed distinct stages of PCM1 scaffold assembly. PCM1 granules first appeared at or near the centrosome, followed by stochastic granule formation in the cytoplasm and subsequent pericentrosomal clustering. This pattern suggests that the centrosome provides a

favorable site for scaffold nucleation, likely by promoting local enrichment of PCM1 above a critical threshold. Consistent with this idea, nocodazole treatment abolished early centrosomal initiation and instead led to stochastic scaffold formation throughout the cytoplasm, indicating that microtubules help spatially restrict the initial nucleation event. Once formed, the scaffold became progressively less dynamic, consistent with maturation into a more stable state.

Following PCM1 scaffold formation, clients were incorporated in a regulated manner that may contribute to CS organization and function. Different clients associated with PCM1 at distinct time points after PCM1 induction, supporting a hierarchical recruitment process. Some clients, such as CEP131 and OFD1, may associate more closely with the scaffold and contribute to its regulation, whereas others appear later, likely as part of functional complexes or co-regulated groups. BBS4, for example, behaved as a late client, consistent with the idea that recruitment of late factors may diversify CS composition and function across contexts (Prasai et al., 2020, Tian et al., 2023). We also found that client association with PCM1 changes during ciliogenesis and after etoposide-induced genotoxic stress, linking client remodeling to context-dependent CS function. Together, these results suggest that hierarchical recruitment contributes to CS compositional heterogeneity and functional adaptability. Future studies, particularly time-resolved proteomic analyses, will be needed to define this process more systematically, as has been done for stress granules (Hu et al., 2023, Marmor-Kollet et al., 2020).

High-resolution imaging further revealed that CS granules are internally organized into subdomains with distinct composition and dynamics. This is important because internal organization is a defining feature of several membrane-less organelles, including PML bodies, paraspeckles, and stress granules, where spatial partitioning helps coordinate protein interactions and function (Fare et al., 2021, Jain et al., 2016, Lallemand-Breitenbach and de The, 2018, Luders, 2012, West et al., 2016). Consistent with this idea, U-ExM analyses showed that different PCM1 regions occupy partially distinct positions within endogenous granules and that multiple client proteins localize to distinct, partially overlapping regions relative to PCM1 and to one another. To generate a quantitative spatial map, we used enlarged GFP-PCM1-N granules, in which internal organization could be resolved more clearly. In this system, different clients occupied broad spatial zones relative to the PCM1 scaffold, consistent with a core-shell-like organization. Although PCM1-N granules lack the C-terminal region and may not fully reflect the architecture of endogenous CS granules, they provide a useful system to

define general principles of CS subdomain organization. This organization could allow co-regulated or functionally related proteins to cluster within specific subdomains, while subdomain-specific dynamics may regulate client exchange with other cellular compartments. Further imaging and proteomic analyses will be needed to define how this organization contributes to CS function.

The *in vitro* reconstitution system provided a powerful approach to examine PCM1 behavior under defined conditions. Earlier studies using PCM1 fragments suggested intrinsic assembly capacity but required non-physiological concentrations and additives (Yu et al., 2023, Zhao et al., 2021). In contrast, our experiments showed that full-length PCM1 forms granules at near-physiological levels and without crowding agents. PCM1 alone was sufficient to assemble an internally organized scaffold, selectively recruit MIB1 and tubulin, and bind microtubules. These findings are consistent with the microtubule-dependent positioning of CS and their role in storing and trafficking clients. This system also provides a platform to test how kinases, RNA, or cellular extracts regulate CS assembly and properties.

Together, our data define the molecular principles of CS assembly and establish PCM1 as the core scaffold for CS organization and function. PCM1 mutations have been associated with schizophrenia, and C-terminal truncations that fuse with kinases have been identified in leukemia (Bousquet and Brousset, 2006, Gurling et al., 2006, Hoeller et al., 2011). Moreover, mutations in several clients have been linked to disorders such as microcephaly and ciliopathies (Begar et al., 2024, Dammermann and Merdes, 2002, Prosser and Pelletier, 2020, Prosser et al., 2022). The framework and tools established here should help define how disease-associated mutations disrupt CS biogenesis and homeostasis.

Materials and Methods

Plasmids

Full-length cDNAs of Homo sapiens PCM1 (GenBank accession no. NP_006188.4) and Homo sapiens MIB1 (GenBank accession no. NM_020774.4) were used. Primers and all oligonucleotide sequences used in this study, including cloning primers and CRISPR guide RNAs are included in Table S2. For PCM1, full-length cDNA and deletion mutants corresponding to GFP-PCM1 (1–6072 bp), GFP-PCM1-N (1–3600 bp), GFP-PCM1-M (2100–3600 bp), GFP-PCM1-NS (1–2100 bp), and GFP-PCM1-C (3600–6072 bp) were amplified by PCR and cloned into the pDONR221 plasmid by Gateway recombination. These inserts were then transferred into pInducer20 (Addgene,

44012) and pEF-FRT-LAP DEST (pMN444, gift from Tim Stearns) vectors by Gateway recombination. To generate a FLAG expression plasmid, PCM1 was cloned into the pCDNA5.1-FRT/TO-Flag-miniTurboID vector (provided by Bettencourt-Dias laboratory, IGC Gulbenkian) using AscI and NotI restriction sites.

For protein purification, cDNAs encoding GFP, mNeonGreen, PCM1 (2100–3600 bp), and PCM1 (4993–6073 bp) were amplified by PCR and first cloned into pDONR221. These inserts were then transferred into the pDEST-His-MBP (Addgene, 11085) and pDEST-GST (Invitrogen, 11802014) expression plasmids by Gateway recombination. Full-length PCM1 was cloned into the pCDH-EF1-mNeonGreen-T2A-Puro (mNeonGreen was cloned using XbaI and EcoRI, System Biosciences, CD527A-1) lentiviral vector using BamHI and NotI restriction sites. Full-length MIB1 was cloned into the pCDH-EF1-mScarlet-T2A-Puro (mScarlet was cloned using XbaI and NheI, System Biosciences, CD527A-1) lentiviral vector using the same restriction sites. mScarlet-MIB1 was amplified from pCDH-mScarlet-MIB1 and cloned into pDEST-His-MBP by Gateway recombination. mNeonGreen-tagged PCM1 was amplified from pCDH-mNeonGreen-PCM1 and cloned into pFastBac-His-MBP by Gateway recombination.

For the inducible dimerization system, FKBP(F36V) was amplified from the pCDNA3.1(+)-miniTurboID-6xGGSGlinker-FKBPF36V-2xHA plasmid (Addgene plasmid #200641) and inserted into the pCDH-EF1-mNeonGreen-PCM1-T2A-Puro lentiviral plasmid using the NotI restriction site.

Cell culture and transfections

Human telomerase-immortalized retinal pigment epithelium cells (hTERT-RPE1, ATCC) were cultured in Dulbecco's Modified Eagle's Medium/F12 (1:1) supplemented with 10% fetal bovine serum (FBS). Human embryonic kidney 293T (HEK293T, ATCC) and human cervical carcinoma cells (HeLa, ATCC) were cultured in DMEM supplemented with 10% FBS. All mammalian cell lines were maintained in a humidified incubator at 37°C with 5% CO2 and confirmed to be mycoplasma negative using a PCR-based assay. RPE1::PCM1 KO (Odabasi et al., 2019), RPE1::mNeonGreen-CCDC66 (Odabasi et al., 2023), and RPE1::mNeonGreen-CSPP1(Frikstad et al., 2019) cell lines were previously described and validated. HeLa::PCM1 KO and HEK293T::PCM1 KO cells were generated using gRNA-containing plasmids and CRISPR/Cas9 editing as previously described (Odabasi et al., 2019).

High Five (Hi-5) insect cells (Thermo Fisher 514005, Gift from Matthew Welch, UC Berkeley) were cultured in serum-free Insect-XPRESS medium, while Spodoptera frugiperda (Sf9) insect cells (ATCC CRL-1711, gift from Monica Betttencourt-Dias, IGC Gulbenkian) were grown in Spodopan medium supplemented with 10% FBS under routine growth conditions. For transfections and baculovirus/protein production, Sf9 cells were switched to serum-free medium. Insect cell lines were maintained at 27°C either as adherent monolayers or in suspension on a rotating shelf. Sf9 cells were transfected with plasmids using FuGENE HD for baculovirus production.

Lentivirus production and cell transduction

Lentivirus was produced by transient transfection of HEK293T cells with the transfer plasmid together packaging and envelope plasmids using pInducer20-GFP-PCM1, pInducer20-GFP-PCM1-N, pInducer20-GFP-PCM1-M, and pCDH-mNG-PCM1 FL-FKBP(F36V) plasmids as transfer vectors. Viral supernatants were collected, clarified by low-speed centrifugation, and used directly for transduction. For infection, 1 × 10^5 RPE1::PCM1 KO cells were seeded into 6-well tissue culture plates one day prior to transduction and infected the next day with 1 ml of viral supernatant. At 24 h post-infection, the medium was replaced with fresh complete medium. After 48 h, the cells were split and subjected to antibiotic selection. Cells transduced with pInducer20-based lentivirus were selected in the presence of 1 mg/ml neomycin (G-418), while cells transduced with pCDH-mNG-based lentivirus were selected with 2 µg/ml puromycin. Selection was continued for 5-7 days until all uninfected control cells had died

Infection efficiency in the heterogeneous pools was assessed by immunofluorescence. Subsequently, cells were trypsinized and serially diluted into complete growth medium to obtain single colonies. Colonies appearing after 10–14 days were picked, expanded, and screened for low-level expression of fusion proteins by immunofluorescence and Western blotting.

Drug treatments

All chemicals used in this study are listed in Table S2 with supplier and catalog number..

For 1,6-hexanediol treatment, cells were incubated in complete medium containing 5% 1,6-hexanediol for 5 min, washed twice with PBS, and fixed. To induce stress granules, cells were treated with 50 mM $NaAsO_2$ for 1 h; their sensitivity to 1,6-hexanediol was then tested by subsequent incubation with 5% 1,6-hexanediol for 5 min.

For nocodazole treatment, inducible RPE1::PCM1 KO cells expressing GFP-PCM1 were subjected to two protocols. In the 2 h assay, cells were treated with 5 µg/ml nocodazole for 1 h in parallel with induction by 1 µM doxycycline for 2 h. In the 16 h assay, cells were simultaneously induced with 1 µM doxycycline and treated with 5 ng/ml nocodazole for 16 h. Following treatment, cells were washed with PBS and fixed.

For RNase treatment, cells were incubated in complete medium containing 100 µg/ml RNase I and RNase A for 1 h, then washed with PBS and fixed.

For etoposide treatment, cells were incubated in complete medium containing 25 µM etoposide or an equivalent volume of DMSO for 24 h. Cells were then washed with PBS and fixed.

For ciliation assays, cells were serum starved in medium containing 0.5% FBS for 24 or 48 h after reaching full confluency. For Hedgehog pathway activation, serum-starved cells were treated with 50 nM SAG for 24 h.

For inducible dimerization of PCM1, RPE1::PCM1 KO cells stably expressing mNG-PCM1-FKBP(F36V) were treated with 250 nM B/B Homodimerizer (AP20187) for at least 4 h. To induce dissociation of dimerized granules, cells were washed twice with PBS and subsequently treated with 1 µM wash-out ligand for a minimum of 1 h. Treatment duration varied according to the experiment, including 24 h for cilium assembly, 48 h for Sonic hedgehog stimulation, and 18 h for live-cell imaging of mitosis.

Immunofluorescence, antibodies and microscopy

Cells were grown on coverslips, washed twice with PBS, and fixed with ice-cold methanol at −20 °C for either 3 or 10 min. After two additional PBS washes, cells were blocked with 3% BSA in PBS containing 0.1% Triton X-100 and incubated with primary antibodies diluted in blocking solution for 1 h at room temperature. Cells were then washed three times with PBS, incubated with secondary antibodies and DAPI (1:2000) for 45 min at room temperature, washed again three times with PBS, and mounted in Mowiol mounting medium containing N-propyl gallate.The source, species, catalog number information and working dilution of all primary and secondary antibodies used for immunofluorescence and immunoblotting are provided in Table S2.

Confocal microscopy was performed on a Leica TCS SP8 or Stellaris 8 laser-scanning inverted confocal microscope equipped for four-color imaging with 405, 488, 561, and 633 nm laser lines, one photomultiplier tube and three hybrid detectors, HC PL APO CS2 63×/1.4 NA and 40×/1.3 NA oil objectives, and an incubation chamber. The pinhole was set to 1 Airy unit. Images were acquired as z-stacks of 20–50 optical

sections with 0.2–0.5 µm spacing, using line averaging of 2–3 and a 400 Hz unidirectional xyz scan mode. Images were collected at 1024 × 1024 pixels with an additional 2–4× optical zoom as needed. Acquisition was controlled with Leica Application Suite X (LAS X) software, and post-processing was performed using either Huygens Professional (Scientific Volume Imaging) or LAS X Lightning. Imaging was performed at room temperature for fixed-cell experiments. Any deconvolution, Lightning processing, maximum-intensity projection, three-dimensional rendering or brightness/contrast adjustment applied after acquisition was performed equally across samples within the same experiment.

3D-SIM imaging was carried out on an Elyra 7 system with Lattice SIM2 (Carl Zeiss Microscopy) using a Plan-Apochromat 63×/1.4 Oil DIC M27 objective, 405/488/561/633 nm laser illumination, and standard excitation/emission filter sets. Images were acquired with a sCMOS (version 4.2 CL HS) camera at 110 nm z-spacing over a 5–10 µm thickness. During acquisition, laser powers at the focal plane were 2–12%, exposure times were 50–250 ms, and camera gain values were 5–50. Raw images were reconstructed using the SIM module of ZEN Black software. Channel alignment was performed using calibration files generated from super-resolution Tetraspec beads (Carl Zeiss Microscopy).

Time-lapse imaging was performed using doxycycline-inducible RPE1::PCM1 KO cell lines expressing GFP-PCM1, GFP-PCM1-N, or GFP-PCM1-M, seeded on 35-mm glass-bottom dishes. Following induction with 1 µM doxycycline, live imaging was carried out on a Stellaris 8 confocal microscope equipped with an HC PL APO CS2 63×/1.4 NA oil objective, maintained at 37 °C with 5% CO_2. The same acquisition settings were used for replicate experiments. For time-lapse imaging of CS dimerization and dissociation, cells were cultured in Ibidi µ-Slide 8-well chambers and imaged at 37 °C and 5% CO_2. Images were acquired every 2 min for the first hour, followed by every 20 min up to 4 h, using a 0.5 µm z-step size and a 512 × 512 pixel format. Dimerizer and washout ligands were added between the first two frames.

Ultrastructural Expansion Microscopy

Ultrastructure Expansion Microscopy (U-ExM) was performed as previously described (Arslanhan et al., 2023). RPE1 and U2OScells were cultured on 12 mm coverslips in 24-well plates and fixed in 1.4% formaldehyde/2% acrylamide (2× FA/AA) in 1× PBS for 5 h at 37 °C. Cells were then embedded in a gel prepared from monomer

Solution (38% sodium acrylamide [w/w], 12.5 µl acrylamide, 2.5 µl BIS, and 5 µl 10× PBS), supplemented with TEMED and 0.5% APS, and polymerized for 1 h at 37 °C.

Denaturation was carried out at 95 °C for 90 min, followed by staining with primary antibodies for 3 h at 37 °C. Gels were washed three times for 10 min each in PBS-T at room temperature (RT), incubated with secondary antibodies for 2.5 h at 37 °C, and washed again three times for 10 min in PBS-T at RT.

Before imaging, gels were expanded three times in 100 ml dH_2O. The expansion factor was determined by measuring the gel diameter with a ruler and dividing it by the original 12 mm coverslip diameter. Expanded gels were cut into smaller pieces and mounted on 24 mm poly-D-lysine–coated coverslips. Imaging was performed on a Leica Stellaris confocal microscope using 0.30 µm z-intervals, and images were deconvolved with Lightning.

Mitotic timing, chromosome congression index, and cell cycle phase measurements

The chromosome congression index was calculated as the ratio of metaphase plate length to width. For multinucleation analysis, RPE1::PCM1 KO cells stably expressing mNG-PCM1-FKBP(F36V) were fixed 24 h after dimerizer treatment and stained with anti-α-tubulin and DAPI. Binucleated cells were scored based on DNA and α-tubulin staining. Cell cycle phase distribution was quantified in control and dimerizer-treated cells using DAPI and α-tubulin staining. Mitotic timing was measured as the interval between nuclear envelope breakdown and anaphase onset, determined from the SiR-tubulin signal. After dimerizer treatment, mitotic cells were further classified by granule number, and cells containing a single granule were analyzed separately from those containing multiple granules. Mitotic defects were scored as mitotic events in which cells entered mitosis but failed before or during anaphase and did not initiate cytokinesis, resulting in binucleation.

Image Analysis

1. Quantification of granule properties and threshold concentrations

Granule properties, including number, size, and intensity, were quantified from GFP-PCM1 or endogenous PCM1 signals using the Surface Creation function in Imaris software (Bitplane, Oxford Instruments). Surfaces were detected by intensity thresholding, and diameters were estimated using the software's built-in algorithm. Manual corrections were applied as needed to ensure accurate segmentation.

Centrosomes were analyzed with the Spot Detection module in Imaris, based on γ-tubulin or centrin 2 signals. Spot size was set to ~1 µm, and automatic detection was performed with an intensity threshold. False positives were removed by manual curation. For each cell, parameters including volume (µm³), average volume (µm³), intensity sum, average intensity, distance to spots, sphericity, and surface count were exported to Excel files and analyzed in GraphPad Prism.

Threshold concentrations were determined from relative protein concentrations, calculated using total fluorescence intensities and volumes. PCM1 granules were segmented from the GFP signal without using the smoothing option, and the *Split Touching Objects* function was used to separate adjoining granules. Different thresholds were applied to distinguish granular from cytoplasmic PCM1. Both were rendered in 3D, and total intensity and volume values were exported. Intensity values were normalized to the maximum fluorescence intensity within each biological replicate. Granule concentration was calculated by dividing total intensity by total volume (µm³) for each cell. Cytoplasmic PCM1 concentration was obtained by subtracting the granule intensity and volume from the whole-cell values, and dividing the remaining intensity by the remaining volume. The threshold concentration of PCM1 granules was defined as the average concentration across all granules in each cell line.

Colocalization was quantified using Pearson's correlation coefficient in the Imaris *Coloc* module. Endogenous PCM1 or GFP-PCM1 was assigned as channel 1, and client proteins as channel 2. Thresholding parameters were chosen to specifically identify PCM1 granules, and a new channel was generated using the *Build Coloc Channel* function. Results were exported via the Image Properties tab and analyzed in GraphPad Prism.

For *in vitro* experiments, granule quantification was performed using Aivia software (Leica Microsystems). Prior to analysis, raw 3D image stacks were background subtracted to improve segmentation by the machine learning tool. Granules were detected using the Object Detection module with optimized intensity thresholding and size filtering to exclude non-specific signals. Segmentation parameters were fine-tuned to eliminate background objects and accurately detect individual granules. Granule volume values were exported and analyzed in GraphPad Prism, with radii calculated assuming a spherical shape.

2. Line profile calculations

3D images were opened in ImageJ in their native format, and z-stacks were projected using the *3D Project* function (Image > Stacks > 3D Project). A line was drawn across

each granule, and intensity values along the line were measured with *Analyze* > *Plot Profile*. Exported values were plotted in GraphPad Prism.

3. Analysis of centrosomal and ciliary protein levels

Centrosomal and ciliary protein levels were quantified in ImageJ. Regions of interest (ROIs) were drawn around centrosomes (marked by γ-tubulin or centrin 2) or primary cilia (marked by Arl13b, acetylated tubulin, or glutamylated tubulin). Corresponding signals were measured, and cytoplasmic background was subtracted for each cell. Values were normalized to the mean intensity of each biological replicate for statistical analysis.

4- Average diameter measurement of clients

Relative client diameter was quantified by line profile analysis in ImageJ. For each granule, a line was drawn across the center of the granule. Intensity values along the line were obtained using the Plot Profile function. Peak positions corresponding to PCM1 and client proteins were identified from the resulting intensity profiles. The distance between peak maxima was used to determine the relative diameter of each client with respect to PCM1. To allow comparison between granules of different sizes, diameter values were normalized to PCM1 (=1) within the same granule.

Fluorescence recovery after photobleaching analysis

Stable RPE1::PCM1 KO cell lines expressing mNG-PCM1-FKBP,GFP-PCM1-N or GFP-PCM1-M were cultured in glass-bottom dishes (Lab-Tek II Chambered Coverglass) and induced with 1 µM doxycycline for 20 min, 1 h, or 16 h. Photobleaching was performed on a Leica SP8 confocal laser scanning microscope equipped with a Plan-Apo 63×/1.4 NA oil objective and a scan zoom of 2.5. Cells were maintained at 37 °C with 5% CO_2 throughout imaging. z-stacks spanning 2.7 µm with a 0.3 µm step size were acquired before and after bleaching. A single pre-bleach image stack was captured, followed by bleaching of defined ROIs using a 488-nm argon laser at 100% power for 10 iterations. Post-bleach image stacks were acquired every 8 s for 5 min. Relative fluorescence intensities were calculated from maximum intensity projections using Fiji, and plotted as a function of time. Quantification of recovery curves, half-time (t½), and mobile fractions was performed using previously described equations (Conkar et al., 2019, Trembecka et al., 2010).

Cell lysis and immunoblotting

Cells were lysed in RIPA buffer containing 50 mM Tris-HCl, 150 mM NaCl, 1.0% (v/v) Triton X-100, 0.5% (w/v) sodium deoxycholate, 1.0 mM EDTA, 0.1% (w/v) SDS,

and protease inhibitors. Lysis was carried out for 30 min at 4°C, followed by centrifugation at 13,000 g for 15 min. Protein concentration in the supernatant was determined using the Bradford assay (Bio-Rad Laboratories). For immunoblotting, equal amounts of protein were loaded and separated by SDS-PAGE, transferred onto nitrocellulose membranes, and blocked with 5% milk in TBS-T for 1 h at room temperature. Membranes were incubated overnight at 4°C with primary antibodies diluted in 5% BSA in TBS-T, followed by three 5-minute washes in TBS-T. They were then incubated with secondary antibodies for 1 h at room temperature, washed again, and visualized using the LI-COR Odyssey Infrared Imaging System at 680 and 800 nm (LI-COR Biosciences). A full list of primary antibodies used for western blot experiments is provided in Table S2. Secondary antibodies used for Western blotting experiments were Alexa Fluor 680- and 800-conjugated antibodies used at 1:15,000 (Invitrogen). Immunoblotting images were acquired using LI-COR acquisition software. Band intensities were measured from raw images using ImageJ signal intensity measurement. Brightness and contrast were applied uniformly across the entire image and did not alter the original bands.

Solubility assay

HEK293T::PCM1 KO cells were co-transfected with GFP-PCM1, GFP-PCM1-N, GFP-PCM1-C, GFP-PCM1-M, or GFP-PCM1-NS. After 48 h, cells were lysed in buffer containing 50 mM HEPES (pH 8), 100 mM KCl, 2 mM EDTA, 10% glycerol, 0.1% Nonidet™ P40, and a protease inhibitor cocktail. Lysates were incubated on ice for 30 min and centrifuged at 18,000 xg for 15 min at 4 °C. Protein concentrations in the supernatants were measured using the Bradford assay. Both the soluble supernatant and the insoluble pellet fractions were resuspended in SDS sample buffer and analyzed by immunoblotting.

Pulldown experiments

For FLAG pulldown experiments, HEK293T::PCM1 KO cells were co-transfected with Flag-PCM1 together with GFP, GFP-PCM1-N, GFP-PCM1-C, GFP-PCM1-M, or GFP-PCM1-NS. After 48 h, cells were washed and lysed in FLAG pulldown buffer (50 mM HEPES, pH 8; 100 mM KCl; 2 mM EDTA; 10% glycerol; 0.1% NP-40; freshly supplemented with 1 mM DTT and protease inhibitors: 10 µg/ml leupeptin, pepstatin, and chymostatin, plus 1 mM PMSF) for 30 min on ice. Lysates were centrifuged at 16,000 xg for 10 min at 4 °C, and supernatants were collected. A 100 µl aliquot of each

sample was reserved as input, and the remaining supernatant was incubated overnight at 4 °C with Anti-FLAG M2 agarose beads for immunoprecipitation. After overnight incubation, the beads were washed with FLAG pulldown buffer, and bound proteins were eluted by boiling in SDS sample buffer. Input and pulldown fractions were resolved by SDS-PAGE and analyzed by immunoblotting.

Protein expression and purification

For the expression of His-MBP-mNG-PCM1, 500 ml of Hi5 cells at a density of 1 × 10^6 cells/ml were infected with P1/P2 baculovirus produced in Sf9 cells at an MOI of 1 and harvested 48 h post-infection. For the expression of His-MBP-mScarlet-MIB1, BL21 Rosetta cells were induced at an OD_{600} of 0.5 with 0.5 mM IPTG, incubated at 18 °C for 18 h, and then harvested.

For protein purification, cells were lysed in ice-cold lysis buffer (50 mM NaH_2PO_4, 500 mM NaCl, 20 mM imidazole, 0.5% Triton, 10% glycerol, 0.5 mM arginine, pH 7.0) supplemented with 1 mM PMSF, 5 mM β-mercaptoethanol, and a protease inhibitor cocktail. Lysates were sonicated and clarified by centrifugation at 18,000 xg for 45 min at 4 °C. Proteins were bound to Ni-NTA beads, eluted with 300 mM imidazole, and dialyzed overnight at 4 °C into storage buffer.

MIB1 was dialyzed into a buffer containing 20 mM HEPES (pH 7.0), 500 mM NaCl, and 1 mM DTT. PCM1 was dialyzed into the same buffer using a PD-10 desalting column. Proteins were then concentrated with Amicon Ultra 30K centrifugal filter devices. Finally, 10 µl aliquots were snap-frozen in liquid nitrogen and stored at −80 °C.

***In vitro* PCM1 granule reconstitution**

Purified His-MBP-mNG-PCM1 was diluted to 0.5 µM, 1 µM or 2 µM in low-salt assay buffer (10 mM HEPES, 0.1 mM EDTA, 2 mM DTT, 150 mM NaCl). After a 5 min incubation, 25 µL of each mixture was loaded into an imaging chamber constructed by mounting HCl-treated glass coverslips onto slides with strips of double-sided tape, as previously described (Alberti et al., 2018). Imaging was performed using a Leica SP8 confocal microscope with an HC PL APO CS2 63× 1.4 NA oil objective. Additional reactions containing 0.15 µM His-MBP-mScarlet-MIB1 were analyzed under the same buffer, imaging, and acquisition conditions, with His-MBP-mScarlet-MIB1 was added to the reaction mix.

For examining microtubule association and the regulation of CS by microtubules, 1 µM Taxol-stabilized microtubules were analyzed in BRB80 buffer (80 mM PIPES pH

6.8, 1 mM EGTA, 1 mM MgCl2) using the same setup. To generate taxol-stabilized microtubules, purified bovine tubulin was first precleared at 440,000 xg for 5 min at 4 °C using a Beckman Coulter Optima MAX-XP ultracentrifuge with a TLA110 rotor. The cleared tubulin was diluted to 2 mg/mL and polymerized at 37 °C for 30 min in the presence of 20 μM Taxol added stepwise at 0.02, 0.2, and 2 μM. After polymerization, purified His-MBP-mNG-PCM1 granule reconstitution assays were performed in BRB80 buffer to maintain microtubule integrity. Reactions with or without microtubules were prepared by mixing purified His-MBP-mNG-PCM1 in BRB80 buffer in the presence or absence of Taxol-stabilized microtubules. After a 5 min incubation, 25 μL of each mixture was loaded into an imaging chamber constructed by mounting HCl-treated glass coverslips onto slides with strips of double-sided tape.

For TIRF analysis, HCl-treated coverslips were mounted onto slides with double-sided tape. Rhodamine-labeled microtubules (1 μM) were polymerized from bovine brain tubulin containing 10% Alexa Fluor™ 568–labeled tubulin mixed with 90% unlabeled tubulin. Microtubules were immobilized on silanized coverslips coated with anti–β-tubulin antibody, prepared by trichloroethylene/dichloromethylsilane treatment. Excess antibody was blocked with 0.2 mg/mL κ-casein and Pluronic-127. After attachment of the microtubules to the slides, microtubules were sequentially washed with 2 mg/mL κ-casein and then 0.05 mg/mL κ-casein. A solution containing 140 nM His-MBP–mNG-PCM1, κ-casein, and an oxygen scavenger system (glucose oxidase, catalase, β-mercaptoethanol, and glucose in BRB80) was introduced and incubated for 3 min to allow PCM1 binding to microtubules. Samples were sealed with nail polish and imaged at 30 °C on a Zeiss ELYRA 7 microscope using a 100× TIRF objective. For the TIRF assay with soluble tubulin, free tubulin supplemented with GMPCPP and DTT was flowed into the chamber.

Statistical analysis

Statistical significance and P values were assessed using Prism 7 software (GraphPad Software, La Jolla, CA). Statistical test used for each experiment is indicated in the corresponding figure legend. For comparisons between two groups with a normal distribution, a two-tailed Student's t-test was used, while one-way analysis of variance (ANOVA) was applied for comparisons involving more than two groups. The sample size (n) represents the number of experimental replicates for each sample and condition. Biological replicate number is also indicated in each figure legend. Error bars in the graphs indicate the standard deviation (SD), and statistical significance levels

were denoted as follows: ns: P>0.05, *:P<0.05, **:P<0.01, ***:P<0.001 and ****:P<0.0001. Individual data points from multiple biological replicates were plotted together, large symbols denote the mean of each biological replicate and small symbols denote individual measurements. SuperPlots were used to visualize both data distribution and reproducibility across biological replicates.

Supplementary materials

Fig. S1 shows the characterization of distinct PCM1 domains; Fig. S2 shows characterization of CS spatiotemporal dynamics and function in the chemically inducible dimerization system; Fig. S3 shows generation and validation of inducible cells for de novo CS biogenesis assay and their functional characterization in ciliogenesis and signaling; Fig. S4 shows phenotypic rescue assays in ciliation efficiency and cilium length; Fig. S5 shows spatiotemporal analysis of CS granule properties during mitosis; Fig. S6 shows spatiotemporal analysis of client recruitment to scaffolds formed by PCM1-N and PCM1-M during CS biogenesis.; Fig. S7 shows PCM1 and client organization into subdomains in U2OS cells; Fig. S8 shows PCM1 scaffold and its clients organization into subdomains within CS granules; Fig. S9 shows colocalization index of PCM1 and clients after DNA damage and different client colocalization of GFP-PCM1 and GFP-PCM1-N during ciliogenesis; and Fig. S10 shows the characterization of biophysical properties of CS. Table S1 shows proteins identified with mass spectrometry analysis purified His-MBP-mNeonGreen-PCM1 and Table S2 shows all antibodies, reagents, plasmids and primers used in the study.

Video 1. Time-lapse confocal microscopy imaging of CS granule (green) behavior during mitosis in control RPE1::PCM1 KO cells stably expressing mNG-PCM1-FKBP(F36V).

Videos 2-4. Time-lapse confocal microscopy imaging of CS granule (green) behavior during mitosis in dimerizer treated RPE1::PCM1 KO cells stably expressing mNG-PCM1-FKBP(F36V) with multiple granules.

Videos 5-10. Time-lapse confocal imaging of RPE1::PCM1 KO cells inducibly expressing GFP-PCM1 (green).

Data availability

All data supporting the findings of this study are available in the manuscript, its supplemental material, or from the corresponding author upon reasonable request.

Acknowledgements

We thank members of CytoLab for feedback on this work, Dila Gulensoy for cloning GFP-tagged PCM1-NS, PCM1-N, and PCM1-C constructs, Dr. Jovana Deretic for assistance with TIRF experiments, and Serra Doğanata for generating the MS coverage map. We acknowledge the Koç University and Istanbul University Animal Facilities. This work was supported by the European Research Council Starting Grant SatelliteHomeostasis under Grant Agreement 101078097, TÜBİTAK 1001 Grant 124Z240, and Istanbul Development Agency YEP-0057 Grant, all awarded to E.N.F.K.

Author contributions: E. Begar: Conceptualization, Methodology, Investigation, Formal analysis, Visualization, Writing – original draft, and Writing – review and editing; E. Seyrek: Methodology, Investigation, Formal analysis, Visualization, and Writing – review and editing; S. Yilmaz-Karaoglu: Methodology, Investigation, Formal analysis, Visualization, and Writing – review and editing; M.D. Arslanhan: Investigation, Visualization, and Writing – review and editing; E. Odabasi: Investigation, Visualization, and Writing – review and editing; E.N. Firat-Karalar: Conceptualization, Supervision, Funding acquisition, Project administration, Writing – original draft, and Writing – review and editing.

Competing interest

The authors declare no competing interests.

References

ALBERTI, S., GLADFELTER, A. & MITTAG, T. 2019. Considerations and Challenges in Studying Liquid-Liquid Phase Separation and Biomolecular Condensates. *Cell,* 176**,** 419-434.

ALBERTI, S., SAHA, S., WOODRUFF, J. B., FRANZMANN, T. M., WANG, J. & HYMAN, A. A. 2018. A User's Guide for Phase Separation Assays with Purified Proteins. *J Mol Biol,* 430**,** 4806-4820.

ARSLANHAN, M. D., CENGIZ-EMEK, S., ODABASI, E., STEIB, E., HAMEL, V., GUICHARD, P. & FIRAT-KARALAR, E. N. 2023. CCDC15 localizes to the centriole inner scaffold and controls centriole length and integrity. *J Cell Biol,* 222.

AYDIN, O. Z., TAFLAN, S. O., GURKASLAR, C. & FIRAT-KARALAR, E. N. 2020. Acute inhibition of centriolar satellite function and positioning reveals their functions at the primary cilium. *PLoS Biol,* 18**,** e3000679.

BANANI, S. F., LEE, H. O., HYMAN, A. A. & ROSEN, M. K. 2017. Biomolecular condensates: organizers of cellular biochemistry. *Nat Rev Mol Cell Biol,* 18**,** 285-298.

BEGAR, E., SEYREK, E. & FIRAT-KARALAR, E. N. 2024. Navigating centriolar satellites: the role of PCM1 in cellular and organismal processes. *FEBS J*.

BOSE, M., LAMPE, M., MAHAMID, J. & EPHRUSSI, A. 2022. Liquid-to-solid phase transition of oskar ribonucleoprotein granules is essential for their function in Drosophila embryonic development. *Cell,* 185**,** 1308-1324 e23.

BOUSQUET, M. & BROUSSET, P. 2006. Myeloproliferative disorders carrying the t(8;9) (PCM1-JAK2) translocation. *Hum Pathol,* 37**,** 500; author reply 500-2.

CHEVRIER, V., BRUEL, A. L., VAN DAM, T. J., FRANCO, B., LO SCALZO, M., LEMBO, F., AUDEBERT, S., BAUDELET, E., ISNARDON, D., BOLE, A., BORG, J. P., KUENTZ, P., THEVENON, J., BURGLEN, L., FAIVRE, L., RIVIERE, J. B., HUYNEN, M. A., BIRNBAUM, D., ROSNET, O. & THAUVIN-ROBINET, C. 2016. OFIP/KIAA0753 forms a complex with OFD1 and FOR20 at pericentriolar satellites and centrosomes and is mutated in one individual with oral-facial-digital syndrome. *Hum Mol Genet,* 25**,** 497-513.

CONKAR, D., BAYRAKTAR, H. & FIRAT-KARALAR, E. N. 2019. Centrosomal and ciliary targeting of CCDC66 requires cooperative action of centriolar satellites, microtubules and molecular motors. *Sci Rep,* 9**,** 14250.

DAMMERMANN, A. & MERDES, A. 2002. Assembly of centrosomal proteins and microtubule organization depends on PCM-1. *J Cell Biol,* 159**,** 255-66.

DOUANNE, T., ANDRE-GREGOIRE, G., THYS, A., TRILLET, K., GAVARD, J. & BIDERE, N. 2019. CYLD Regulates Centriolar Satellites Proteostasis by Counteracting the E3 Ligase MIB1. *Cell Rep,* 27**,** 1657-1665 e4.

FARE, C. M., VILLANI, A., DRAKE, L. E. & SHORTER, J. 2021. Higher-order organization of biomolecular condensates. *Open Biol,* 11**,** 210137.

FIRAT-KARALAR, E. N., RAUNIYAR, N., YATES, J. R., 3RD & STEARNS, T. 2014. Proximity interactions among centrosome components identify regulators of centriole duplication. *Curr Biol,* 24**,** 664-70.

FRIKSTAD, K. M., MOLINARI, E., THORESEN, M., RAMSBOTTOM, S. A., HUGHES, F., LETTEBOER, S. J. F., GILANI, S., SCHINK, K. O., STOKKE, T., GEIMER, S., PEDERSEN, L. B., GILES, R. H., AKHMANOVA, A., ROEPMAN, R., SAYER, J. A. & PATZKE, S. 2019. A CEP104-CSPP1 Complex Is Required for Formation of Primary Cilia Competent in Hedgehog Signaling. *Cell Rep,* 28**,** 1907-1922 e6.

GEIGER, T., VELIC, A., MACEK, B., LUNDBERG, E., KAMPF, C., NAGARAJ, N., UHLEN, M., COX, J. & MANN, M. 2013. Initial quantitative proteomic map of 28 mouse tissues using the SILAC mouse. *Mol Cell Proteomics,* 12**,** 1709-22.

GHEIRATMAND, L., COYAUD, E., GUPTA, G. D., LAURENT, E. M., HASEGAN, M., PROSSER, S. L., GONCALVES, J., RAUGHT, B. & PELLETIER, L. 2019. Spatial and proteomic profiling reveals centrosome-independent features of centriolar satellites. *EMBO J*.

GOMES, E. & SHORTER, J. 2019. The molecular language of membraneless organelles. *J Biol Chem,* 294**,** 7115-7127.

GUPTA, G. D., COYAUD, E., GONCALVES, J., MOJARAD, B. A., LIU, Y., WU, Q., GHEIRATMAND, L., COMARTIN, D., TKACH, J. M., CHEUNG, S. W., BASHKUROV, M., HASEGAN, M., KNIGHT, J. D., LIN, Z. Y., SCHUELER, M., HILDEBRANDT, F., MOFFAT, J., GINGRAS, A. C., RAUGHT, B. & PELLETIER, L. 2015. A Dynamic Protein Interaction Landscape of the Human Centrosome-Cilium Interface. *Cell,* 163**,** 1484-99.

GURLING, H. M., CRITCHLEY, H., DATTA, S. R., MCQUILLIN, A., BLAVERI, E., THIRUMALAI, S., PIMM, J., KRASUCKI, R., KALSI, G., QUESTED, D., LAWRENCE, J., BASS, N., CHOUDHURY, K., PURI, V., O'DALY, O., CURTIS, D., BLACKWOOD, D., MUIR, W., MALHOTRA, A. K., BUCHANAN, R. W., GOOD, C. D., FRACKOWIAK, R. S. & DOLAN, R. J. 2006. Genetic association and brain

morphology studies and the chromosome 8p22 pericentriolar material 1 (PCM1) gene in susceptibility to schizophrenia. *Arch Gen Psychiatry,* 63**,** 844-54.
HALL, E. A., KUMAR, D., PROSSER, S. L., YEYATI, P. L., HERRANZ-PEREZ, V., GARCIA-VERDUGO, J. M., ROSE, L., MCKIE, L., DODD, D. O., TENNANT, P. A., MEGAW, R., MURPHY, L. C., FERREIRA, M. F., GRIMES, G., WILLIAMS, L., QUIDWAI, T., PELLETIER, L., REITER, J. F. & MILL, P. 2023. Centriolar satellites expedite mother centriole remodeling to promote ciliogenesis. *Elife,* 12.
HEIN, M. Y., HUBNER, N. C., POSER, I., COX, J., NAGARAJ, N., TOYODA, Y., GAK, I. A., WEISSWANGE, I., MANSFELD, J., BUCHHOLZ, F., HYMAN, A. A. & MANN, M. 2015. A human interactome in three quantitative dimensions organized by stoichiometries and abundances. *Cell,* 163**,** 712-23.
HOELLER, S., WALZ, C., REITER, A., DIRNHOFER, S. & TZANKOV, A. 2011. PCM1-JAK2-fusion: a potential treatment target in myelodysplastic-myeloproliferative and other hemato-lymphoid neoplasms. *Expert Opin Ther Targets,* 15**,** 53-62.
HU, S., ZHANG, Y., YI, Q., YANG, C., LIU, Y. & BAI, Y. 2023. Time-resolved proteomic profiling reveals compositional and functional transitions across the stress granule life cycle. *Nat Commun,* 14**,** 7782.
HYMAN, A. A., WEBER, C. A. & JULICHER, F. 2014. Liquid-liquid phase separation in biology. *Annu Rev Cell Dev Biol,* 30**,** 39-58.
INOBE, T. & NUKINA, N. 2016. Rapamycin-induced oligomer formation system of FRB-FKBP fusion proteins. *J Biosci Bioeng,* 122**,** 40-6.
ITOH, Y., IIDA, S., TAMURA, S., NAGASHIMA, R., SHIRAKI, K., GOTO, T., HIBINO, K., IDE, S. & MAESHIMA, K. 2021. 1,6-hexanediol rapidly immobilizes and condenses chromatin in living human cells. *Life Sci Alliance,* 4.
JAIN, S., WHEELER, J. R., WALTERS, R. W., AGRAWAL, A., BARSIC, A. & PARKER, R. 2016. ATPase-Modulated Stress Granules Contain a Diverse Proteome and Substructure. *Cell,* 164**,** 487-98.
JIANG, X., HO, D. B. T., MAHE, K., MIA, J., SEPULVEDA, G., ANTKOWIAK, M., JIANG, L., YAMADA, S. & JAO, L. E. 2021. Condensation of pericentrin proteins in human cells illuminates phase separation in centrosome assembly. *J Cell Sci,* 134.
JOACHIM, J., RAZI, M., JUDITH, D., WIRTH, M., CALAMITA, E., ENCHEVA, V., DYNLACHT, B. D., SNIJDERS, A. P., O'REILLY, N., JEFFERIES, H. B. J. & TOOZE, S. A. 2017. Centriolar Satellites Control GABARAP Ubiquitination and GABARAP-Mediated Autophagy. *Curr Biol,* 27**,** 2123-2136 e7.
KANEKURA, K., YAMANAKA, Y., MIYAGI, T. & KURODA, M. 2022. Chemically oligomerizable TDP-43: a novel chemogenetic tool for studying the pathophysiology of amyotrophic lateral sclerosis. *Neural Regen Res,* 17**,** 2434-2436.
KIM, J., KRISHNASWAMI, S. R. & GLEESON, J. G. 2008. CEP290 interacts with the centriolar satellite component PCM-1 and is required for Rab8 localization to the primary cilium. *Hum Mol Genet,* 17**,** 3796-805.
KIM, K., LEE, K. & RHEE, K. 2012. CEP90 is required for the assembly and centrosomal accumulation of centriolar satellites, which is essential for primary cilia formation. *PLoS One,* 7**,** e48196.
KUBO, A., SASAKI, H., YUBA-KUBO, A., TSUKITA, S. & SHIINA, N. 1999. Centriolar satellites: molecular characterization, ATP-dependent movement toward centrioles and possible involvement in ciliogenesis. *J Cell Biol,* 147**,** 969-80.
KUBO, A. & TSUKITA, S. 2003. Non-membranous granular organelle consisting of PCM-1: subcellular distribution and cell-cycle-dependent assembly/disassembly. *J Cell Sci,* 116**,** 919-28.

LALLEMAND-BREITENBACH, V. & DE THE, H. 2018. PML nuclear bodies: from architecture to function. *Curr Opin Cell Biol,* 52**,** 154-161.

LI, P., BANJADE, S., CHENG, H. C., KIM, S., CHEN, B., GUO, L., LLAGUNO, M., HOLLINGSWORTH, J. V., KING, D. S., BANANI, S. F., RUSSO, P. S., JIANG, Q. X., NIXON, B. T. & ROSEN, M. K. 2012. Phase transitions in the assembly of multivalent signalling proteins. *Nature,* 483**,** 336-40.

LI, Y., LIU, Y., YU, X. Y., XU, Y., PAN, X., SUN, Y., WANG, Y., SONG, Y. H. & SHEN, Z. 2024. Membraneless organelles in health and disease: exploring the molecular basis, physiological roles and pathological implications. *Signal Transduct Target Ther,* 9**,** 305.

LOPES, C. A., PROSSER, S. L., ROMIO, L., HIRST, R. A., O'CALLAGHAN, C., WOOLF, A. S. & FRY, A. M. 2011. Centriolar satellites are assembly points for proteins implicated in human ciliopathies, including oral-facial-digital syndrome 1. *J Cell Sci,* 124**,** 600-12.

LUDERS, J. 2012. The amorphous pericentriolar cloud takes shape. *Nat Cell Biol,* 14**,** 1126-8.

MARMOR-KOLLET, H., SIANY, A., KEDERSHA, N., KNAFO, N., RIVKIN, N., DANINO, Y. M., MOENS, T. G., OLENDER, T., SHEBAN, D., COHEN, N., DADOSH, T., ADDADI, Y., RAVID, R., EITAN, C., TOTH COHEN, B., HOFMANN, S., RIGGS, C. L., ADVANI, V. M., HIGGINBOTTOM, A., COOPER-KNOCK, J., HANNA, J. H., MERBL, Y., VAN DEN BOSCH, L., ANDERSON, P., IVANOV, P., GEIGER, T. & HORNSTEIN, E. 2020. Spatiotemporal Proteomic Analysis of Stress Granule Disassembly Using APEX Reveals Regulation by SUMOylation and Links to ALS Pathogenesis. *Mol Cell,* 80**,** 876-891 e6.

MENNELLA, V., KESZTHELYI, B., MCDONALD, K. L., CHHUN, B., KAN, F., ROGERS, G. C., HUANG, B. & AGARD, D. A. 2012. Subdiffraction-resolution fluorescence microscopy reveals a domain of the centrosome critical for pericentriolar material organization. *Nat Cell Biol,* 14**,** 1159-68.

MONROE, T. O., GARRETT, M. E., KOUSI, M., RODRIGUIZ, R. M., MOON, S., BAI, Y., BRODAR, S. C., SOLDANO, K. L., SAVAGE, J., HANSEN, T. F., MUZNY, D. M., GIBBS, R. A., BARAK, L., SULLIVAN, P. F., ASHLEY-KOCH, A. E., SAWA, A., WETSEL, W. C., WERGE, T. & KATSANIS, N. 2020. PCM1 is necessary for focal ciliary integrity and is a candidate for severe schizophrenia. *Nat Commun,* 11**,** 5903.

NACHURY, M. V., LOKTEV, A. V., ZHANG, Q., WESTLAKE, C. J., PERANEN, J., MERDES, A., SLUSARSKI, D. C., SCHELLER, R. H., BAZAN, J. F., SHEFFIELD, V. C. & JACKSON, P. K. 2007. A core complex of BBS proteins cooperates with the GTPase Rab8 to promote ciliary membrane biogenesis. *Cell,* 129**,** 1201-13.

ODABASI, E., BATMAN, U. & FIRAT-KARALAR, E. N. 2020. Unraveling the mysteries of centriolar satellites: time to rewrite the textbooks about the centrosome/cilium complex. *Mol Biol Cell,* 31**,** 866-872.

ODABASI, E., CONKAR, D., DERETIC, J., BATMAN, U., FRIKSTAD, K. M., PATZKE, S. & FIRAT-KARALAR, E. N. 2023. CCDC66 regulates primary cilium length and signaling via interactions with transition zone and axonemal proteins. *J Cell Sci,* 136.

ODABASI, E., GUL, S., KAVAKLI, I. H. & FIRAT-KARALAR, E. N. 2019. Centriolar satellites are required for efficient ciliogenesis and ciliary content regulation. *EMBO Rep*.

PATEL, A., LEE, H. O., JAWERTH, L., MAHARANA, S., JAHNEL, M., HEIN, M. Y., STOYNOV, S., MAHAMID, J., SAHA, S., FRANZMANN, T. M., POZNIAKOVSKI, A., POSER, I., MAGHELLI, N., ROYER, L. A., WEIGERT, M., MYERS, E. W., GRILL, S., DRECHSEL, D., HYMAN, A. A. & ALBERTI, S. 2015. A Liquid-to-Solid Phase Transition of the ALS Protein FUS Accelerated by Disease Mutation. *Cell,* 162**,** 1066-77.

PRASAI, A., SCHMIDT CERNOHORSKA, M., RUPPOVA, K., NIEDERLOVA, V., ANDELOVA, M., DRABER, P., STEPANEK, O. & HURANOVA, M. 2020. The BBSome assembly is spatially controlled by BBS1 and BBS4 in human cells. *J Biol Chem,* 295**,** 14279-14290.

PROSSER, S. L. & PELLETIER, L. 2020. Centriolar satellite biogenesis and function in vertebrate cells. *J Cell Sci,* 133.

PROSSER, S. L., TKACH, J., GHEIRATMAND, L., KIM, J., RAUGHT, B., MORRISON, C. G. & PELLETIER, L. 2022. Aggresome assembly at the centrosome is driven by CP110-CEP97-CEP290 and centriolar satellites. *Nat Cell Biol,* 24**,** 483-496.

QUARANTOTTI, V., CHEN, J. X., TISCHER, J., GONZALEZ TEJEDO, C., PAPACHRISTOU, E. K., D'SANTOS, C. S., KILMARTIN, J. V., MILLER, M. L. & GERGELY, F. 2019. Centriolar satellites are acentriolar assemblies of centrosomal proteins. *EMBO J*.

RAI, A. K., CHEN, J. X., SELBACH, M. & PELKMANS, L. 2018. Kinase-controlled phase transition of membraneless organelles in mitosis. *Nature,* 559**,** 211-216.

ROLLINS, C. T., RIVERA, V. M., WOOLFSON, D. N., KEENAN, T., HATADA, M., ADAMS, S. E., ANDRADE, L. J., YAEGER, D., VAN SCHRAVENDIJK, M. R., HOLT, D. A., GILMAN, M. & CLACKSON, T. 2000. A ligand-reversible dimerization system for controlling protein-protein interactions. *Proc Natl Acad Sci U S A,* 97**,** 7096-101.

SO, C., SERES, K. B., STEYER, A. M., MONNICH, E., CLIFT, D., PEJKOVSKA, A., MOBIUS, W. & SCHUH, M. 2019. A liquid-like spindle domain promotes acentrosomal spindle assembly in mammalian oocytes. *Science,* 364.

SOROKIN, S. P. 1968. Reconstructions of centriole formation and ciliogenesis in mammalian lungs. *J Cell Sci,* 3**,** 207-30.

SRSEN, V., FANT, X., HEALD, R., RABOUILLE, C. & MERDES, A. 2009. Centrosome proteins form an insoluble perinuclear matrix during muscle cell differentiation. *BMC Cell Biol,* 10**,** 28.

TIAN, X., ZHAO, H. & ZHOU, J. 2023. Organization, functions, and mechanisms of the BBSome in development, ciliopathies, and beyond. *Elife,* 12.

TOLLENAERE, M. A., MAILAND, N. & BEKKER-JENSEN, S. 2015a. Centriolar satellites: key mediators of centrosome functions. *Cell Mol Life Sci,* 72**,** 11-23.

TOLLENAERE, M. A. X., VILLUMSEN, B. H., BLASIUS, M., NIELSEN, J. C., WAGNER, S. A., BARTEK, J., BELI, P., MAILAND, N. & BEKKER-JENSEN, S. 2015b. p38- and MK2-dependent signalling promotes stress-induced centriolar satellite remodelling via 14-3-3-dependent sequestration of CEP131/AZI1. *Nat Commun,* 6**,** 10075.

TREMBECKA, D. O., KUZAK, M. & DOBRUCKI, J. W. 2010. Conditions for using FRAP as a quantitative technique--influence of the bleaching protocol. *Cytometry A,* 77**,** 366-70.

VILLUMSEN, B. H., DANIELSEN, J. R., POVLSEN, L., SYLVESTERSEN, K. B., MERDES, A., BELI, P., YANG, Y. G., CHOUDHARY, C., NIELSEN, M. L., MAILAND, N. & BEKKER-JENSEN, S. 2013. A new cellular stress response that triggers centriolar satellite reorganization and ciliogenesis. *EMBO J,* 32**,** 3029-40.

WANG, L., LEE, K., MALONIS, R., SANCHEZ, I. & DYNLACHT, B. D. 2016. Tethering of an E3 ligase by PCM1 regulates the abundance of centrosomal KIAA0586/Talpid3 and promotes ciliogenesis. *Elife,* 5.

WANG, M., HERRMANN, C. J., SIMONOVIC, M., SZKLARCZYK, D. & VON MERING, C. 2015. Version 4.0 of PaxDb: Protein abundance data, integrated across model organisms, tissues, and cell-lines. *Proteomics,* 15**,** 3163-8.

WEST, J. A., MITO, M., KUROSAKA, S., TAKUMI, T., TANEGASHIMA, C., CHUJO, T., YANAKA, K., KINGSTON, R. E., HIROSE, T., BOND, C., FOX, A. & NAKAGAWA, S. 2016. Structural, super-resolution microscopy analysis of paraspeckle nuclear body organization. *J Cell Biol,* 214**,** 817-30.

WHEELER, J. R., MATHENY, T., JAIN, S., ABRISCH, R. & PARKER, R. 2016. Distinct stages in stress granule assembly and disassembly. *Elife,* 5.

WOODRUFF, J. B., HYMAN, A. A. & BOKE, E. 2018. Organization and Function of Non-dynamic Biomolecular Condensates. *Trends Biochem Sci,* 43**,** 81-94.

YAMANAKA, Y., MIYAGI, T., HARADA, Y., KURODA, M. & KANEKURA, K. 2021. Establishment of chemically oligomerizable TAR DNA-binding protein-43 which mimics amyotrophic lateral sclerosis pathology in mammalian cells. *Lab Invest,* 101**,** 1331-1340.

YANG, P., MATHIEU, C., KOLAITIS, R. M., ZHANG, P., MESSING, J., YURTSEVER, U., YANG, Z., WU, J., LI, Y., PAN, Q., YU, J., MARTIN, E. W., MITTAG, T., KIM, H. J. & TAYLOR, J. P. 2020. G3BP1 Is a Tunable Switch that Triggers Phase Separation to Assemble Stress Granules. *Cell,* 181**,** 325-345 e28.

YU, F., YANG, S., NI, H., HENG, D., WU, X., YANG, M., ZHANG, X., CAO, Y., PEI, Y., AN, D., LI, D., LIU, D., LIU, L., PAN, L., CHEN, Q., ZHU, X. & ZHOU, J. 2023. O-GlcNAcylation Regulates Centrosome Behavior and Cell Polarity to Reduce Pulmonary Fibrosis and Maintain the Epithelial Phenotype. *Adv Sci (Weinh),* 10**,** e2303545.

YU, N., SIGNORILE, L., BASU, S., OTTEMA, S., LEBBINK, J. H. G., LESLIE, K., SMAL, I., DEKKERS, D., DEMMERS, J. & GALJART, N. 2016. Isolation of Functional Tubulin Dimers and of Tubulin-Associated Proteins from Mammalian Cells. *Curr Biol,* 26**,** 1728-1736.

ZHANG, P., FAN, B., YANG, P., TEMIROV, J., MESSING, J., KIM, H. J. & TAYLOR, J. P. 2019. Chronic optogenetic induction of stress granules is cytotoxic and reveals the evolution of ALS-FTD pathology. *Elife,* 8.

ZHAO, H., CHEN, Q., LI, F., CUI, L., XIE, L., HUANG, Q., LIANG, X., ZHOU, J., YAN, X. & ZHU, X. 2021. Fibrogranular materials function as organizers to ensure the fidelity of multiciliary assembly. *Nat Commun,* 12**,** 1273.

Figure 1

PCM1 is a modular protein with domains important for granule formation and regulation of granule properties.

(A) Schematic representation of the domain architecture of human PCM1. The *PCM1* gene encodes a 2024 amino acid (aa) acidic protein with a molecular weight of 228 kDa and an isoelectric point (pI) of 4.99. It contains 8 coiled-coil domains, each represented by gray coils located at CC1: 270–293 aa, CC2: 493–513 aa, CC3: 652–682 aa, CC4: 732–769 aa, CC5: 826–853 aa, CC6: 989–1016 aa, CC7: 1065–1085 aa, and CC8: 1517–1537 aa. It is highly enriched in intrinsically disordered regions (IDRs) predicted by PONDR (predictor of naturally disordered regions) with the VL3 model. Scores above 0.5 indicate disordered regions, whereas scores below 0.5 are ordered. PCM1 contains two self-association domains (201–494 aa and 745–1128 aa, in green), a conserved C-terminal domain (1372–1990 aa, in blue), and an LC3-interacting region (LIR) domain (1953–1958, in yellow).

(B) Schematic representation of PCM1 truncation constructs designed based on domain analysis and the presence or absence of self-association domains. PCM1-NS contains the first self-association domain, PCM1-M contains the second, and PCM1-N includes both, whereas PCM1-C lacks them. Three antibodies targeting PCM1 at different regions are shown in red (PCM1-N-Ab targets 1-254 aa, PCM1-M-Ab targets 700-1200 aa, PCM1-C-Ab targets 1664-2024 aa).

(C) PCM1 truncation mutants and their subcellular localization. Representative confocal images show HeLa-WT and HeLa::PCM1 KO cells transfected with the indicated constructs. Cells were stained for anti-GFP. Similar results were obtained from three biological replicates. Scale bar: 10 μm.

(D) Quantification of volume (μm^3) of granules in Hela cells transfected with full length or truncation mutants of PCM1 tagged with GFP. Each point represents volume of a single granule detected by Imaris Software. Only GFP-positive cells were selected for quantification. The data represent the mean from three biological replicates, with n>300 granules per replicate, green, magenta and orange colored dots representing different replicates. Data are presented as mean ±SD. Values are in log10 scale.

(E) Solubility analysis of GFP-PCM1 and truncation mutants. Immunoblot analysis of lysates from HEK293T cells transfected with GFP, GFP-PCM1, GFP-PCM1-N, GFP-PCM1-C, and GFP-PCM1-M plasmids for 48 hours. Cells were lysed with pulldown buffer and separated as the soluble fraction (S). Remaining insoluble fraction was further lysed with 2X sample buffer. Membranes were stained with anti-GFP-Ab. S: Soluble, IS: Insoluble.

(F) Localization of PCM1 and its truncation mutants at increasing concentrations in HeLa::PCM1 KO cells. These cells are transfected with GFP fusions of PCM1, PCM1-N, PCM1-M, PCM1-NS and PCM1-C for 48 hours, fixed and stained with anti-

GFP. The images indicate the cells with increasing expression levels of PCM1 and its truncations, indicated by a green triangle at the top. Scale bar: 10 μm.

(G) Quantification of the threshold concentrations at which granules formed for PCM1 and its truncations from (E). For each transfected cell, GFP signal intensity per total cell volume and the intensity of cytoplasmic granules were quantified using Imaris software. The threshold concentration represents the mean value of the granular concentration measurements per cell for both granular and cytoplasmic PCM1. Green bars represent average concentration of granule forming cells. Pink bars represent the maximum and minimum values of granule forming cell concentration. Results are from three biological replicates, min 48 cells in total. Data are presented as mean ±SD. a.u.: arbitrary unit.

Figure 2

Effect of forced dimerization of PCM1 on CS properties and signaling.

(A) Schematic representation and validation of the chemically inducible CS dimerization system. mNeonGreen-PCM1 is fused to the FKBP(F36V) mutant, which dimerizes upon the addition of AP20187 (homodimerizer) and dimerization is reversed with AP22542 (wash-out ligand) treatment.

(B) Chemically inducible homodimerization of PCM1 alters CS granule properties. The images represent CS granules under three conditions in RPE1::PCM1 KO cells stably expressing mNG-PCM1-FKBP(F36V): no treatment (NT), with the dimerizer, and with the wash-out (W/O) ligand after dimerization. Cells were treated with the dimerizer for 4 hours and then either fixed directly or treated with the wash-out ligand for 1 hour before fixation. Cells were stained with antibodies for mNeonGreen and PCM1. Scale bars: 30 µm (main panels), 5 µm (insets)

(C) Quantification of CS granule properties from (B). Granule number per cell and mean granule volume were quantified using Imaris Software. Results are from three biological replicates, green, magenta and orange colored dots representing different replicates. n=35 cells for each replicate. Data are presented as mean ±SD.

(D) The effect of disrupting CS granule properties on ciliary signaling. The images represent CS granules under three conditions in RPE1::PCM1 KO cells stably expressing mNG-PCM1-FKBP(F36V): no treatment (NT), with the dimerizer, and with the wash-out (W/O) ligand after dimerization. Ciliation was induced by serum starvation for 24 hours. The Sonic Hedgehog pathway was activated by treating cells with 50 nM of the Smoothened agonist SAG for 24 hours. Cells were fixed and stained for mNeonGreen, SMO, and Arl13b. Scale bars: 20 µm (main panels), 5 µm (insets)

(E) Quantification of Smo recruitment to the cilium as shown in (K). Smo intensity at the cilium was calculated using ImageJ. Only mNG-PCM1-positive cells were selected for quantification. The data represent the mean from three biological replicates, green, magenta and orange colored dots representing different replicates. ns: not significant. Data are presented as mean ±SD.

(F) Characterization of CS granules following inducible dimerization at various stages of mitosis. Cells were fixed and stained for mNeonGreen and Centrin 2. Representative images show CS granules in control and dimerizer-treated cells at interphase, metaphase, anaphase, and telophase. Scale bar: 10 µm.

(G) Still images from the time-lapse movies for 3 different conditions. CS granules (green) behavior during mitosis was imaged in both control and dimerizer-treated cells and cells containing multiple granules and a single large granule after dimerization were separated for representation purposes. Both conditions were also treated with SiR-tubulin to visualize spindle microtubules (magenta). Live imaging

was conducted for at least 12 hours. Dotted lines represent cell boundaries. Scale bar: 10 µm.

(H) Quantification of mitotic time (min) of RPE1::PCM1 KO cells stably expressing mNG-PCM1-FKBP(F36V) with or without dimerizer addition. Cells containing multiple granules and a single large granule after dimerization were separated for quantification purposes. Mitotic time values were calculated using SiRtubulin signal from nuclear envelope breaktime to anaphase start. Results are from two biological replicates, n=30 cells per replicate. Green and magenta colored dots representing different replicates. Data are presented as mean ±SD. ns: not significant.

(I) Quantification of percentage of defective mitotic cells of RPE1::PCM1 KO cells stably expressing mNG-PCM1-FKBP(F36V) with or without dimerizer addition. Cells containing multiple granules and a single large granule after dimerization were separated for quantification purposes. Defective mitosis represents incomplete mitosis shown in (B). Results are from two biological replicates, n>50 cells per replicate. Green and magenta colored dots representing different replicates' mean values. Data are presented as mean ±SD.

Figure 3

Spatiotemporal dynamics of PCM1 scaffold formation during CS biogenesis.

(A) Fixed imaging of cells from the *de novo* CS biogenesis assay. Representative confocal images of PCM1 granule formation in RPE1::PCM1 KO cells inducibly expressing GFP-PCM1, GFP-PCM1-N and GFP-PCM1-M. Cells were induced by 1 µM doxycycline for 10 minutes, 30 minutes, 1 hour, 2 hours, 4 hours, 8 hours or 16 hours, fixed and stained with antibodies for GFP and Centrin-2 and DAPI for nucleus. Cyan arrowhead denotes centrosomes at each time point. Scale bars: 10 µm (main panels), 2 µm (insets)

(B) Quantification of size, fluorescence intensity and number of PCM1 granules from (A). Total volume of granules per cell (μm^3), average volume of granules per cell (μm^3), total granule intensity, average granule intensity, granule number, and average distance of granules to centrosome (µm) values were measured using Imaris software. Average values represent total values divided by the number of granules for each cell. Average distance to centrosome values were quantified from the distance between granules and centrosomes marked by centrin 2 for each cell. Results are from three biological replicates, n=48 cells per time point. Data are presented as mean ±SD.

(C) Time-lapse confocal imaging of PCM1 granules from the *de novo* CS biogenesis assay. Images represent still frames from time-lapse confocal images of RPE1::PCM1 KO cells inducibly expressing GFP-PCM1, GFP-PCM1-N, and GFP-PCM1-M. Cells were imaged following the addition of 1 µM doxycycline and SIR-tubulin. The time labeled '0 min' marks the initiation of granule nucleation. Centrosomes are indicated by cyan arrowheads at each time point, and cell boundaries are outlined with white dashed lines. Frame times (in minutes) are displayed at the top of each image. Scale bars: 5 µm.

(D) Quantification of size, fluorescence intensity and number of PCM1 granules from C as described in (B). Average distance to centrosome values were quantified from the distance between granules and SIR-tubulin staining for each cell. Images were taken in 3 minute intervals for 348 minutes. Results are from three biological replicates, data represents the mean of n=5 cells. Data are presented as mean ±SD.

(E) Relationship between average PCM1 granule volume and number during *de novo* CS biogenesis. The average granule volume per cell (μm^3) and the number of granules were quantified using Imaris software. Results are from three biological replicates, n=5 cells analyzed.. Assembly progression is categorized into three phases: (1) nucleation, (2) growth, and (3) steady-state."

Figure 4

Dynamic properties of CS

(A) FRAP analysis on GFP-PCM1-N and GFP-PCM1-M granules formed in a *de novo* biogenesis assay. RPE1::PCM1 KO cells expressing either GFP-PCM1-N or GFP-PCM1-M were induced with doxycycline for 20 minutes, 1 hour, and 16 hours. The specified regions were photobleached and subsequently imaged for 300 seconds post-bleaching. Scale bars: 1 µm. Quantification of mobile pool and half-time of fluorescence recovery from (A). Mobile fractions and half-lives times of fluorescence recovery were calculated based on granule recovery (n = 3 independent FRAP experiments from three biological replicates). Circles represent individual experiments, and triangles indicate the mean values.

(B) Representative time-lapse images show the dynamics of fusion, splitting, and kiss-and-run interactions among PCM1 granules. Representative still frames from time-lapse confocal image show there different dynamic event. Granules are marked with magenta and cyan arrowheads. Five different colors show varying levels of fluorescent intensity, ranging from blue (lowest) to white (highest). These results denote one granule as an example for each dynamic behavior and are consistent with findings from three independent experiments.

(C) Representative confocal images of RPE1 cells treated with different reagents, fixed with methanol and stained with anti-PCM1-C Ab and DAPI for nucleus. Untreated cells serve as the control. Cells were treated with 5% 1,6-hexanediol for 5 minutes, 100 µg/ml RNase A+I for 1 hour. Scale bars: 10 µm (main panels), 5 µm (insets).

(D) Total volume of granules per cell (μm^3) and total granule intensity values were measured using Imaris software. Granule intensity was normalized to control values for each replicate. Number of cells for each total intensity value was determined from relative frequency data. Statistical significance was determined by the Student's *t*-test (paired and two-tailed). Results are from three biological replicates, green, magenta and orange colored dots representing different replicates. n=30 cells for each replicate. **P*<0.05; ***P*<0.01, ****P*<0.001*****P*<0.0001; ns, not significant.

(E) Representative confocal images of RPE1 cells treated with different reagents after stress induction, fixed with methanol and stained with anti-PCM1-C Ab (green), G3BP1 (magenta) and DAPI for nucleus. Untreated cells serve as the control. Cells were treated with 50 mM sodium arsenate treatment for 1 hour for stress induction, the either 5% 1,6-hexanediol for 5 minutes or 100 µg/ml RNase A+I for 1 hour. Scale bars: 10 µm (main panels), 5 µm (insets).

(F) Experimental schematic of 1,6-Hexanediol treatment after stress induction. RPE1 cells were treated with 50 mM sodium arsenate treatment for 1 hour for stress induction, followed by 5% 1,6-Hexanediol treatment for 5 minutes. Cells were then fixed and stained for PCM1 and G3BP1 antibodies marking CS and stress granules

respectively. Cells were stained with anti-PCM1-Ab (green), anti-G3BP1 (magenta) and DAPI for nucleus (blue). Scale bars: 10 µm (main panels), 2 µm (insets).

(G) Representative confocal images of RPE1::PCM1 KO cells inducibly expressing GFP-PCM1 transfected with either control or 1,6-HD treatment after 2 h or 16 h doxycycline induction. After 2 h or 16 h doxycycline induction, cells were treated with 5% 1,6-HD for 5 minute, whereas control cells were fixed after 5 minutes. Cells were fixed and stained for anti-GFP (green), anti-centrin (magenta) and nucleus (blue). Scale bars: 10 µm for images, 5 µm for insets.

(H) Granule properties, including total volume of granules per cell (μm^3), average volume of granules per cell (μm^3), total granule intensity, granule number values were measured from (G) using Imaris software. Average values represent total values divided by the number of values for each cell. Statistical significance was determined by the Student's *t*-test (paired and two-tailed). Results are from two biological replicates, green and magenta colored dots representing different replicates. *:P<0.05; **:P<0.01, ***:P<0.001****:P<0.0001; ns: not significant.

Figure 5

Spatiotemporal analysis of client recruitment during CS biogenesis.

(A) RPE1::PCM1 KO cells inducibly expressing GFP-PCM1 were fixed before induction and 10 min, 30 min, 2 hours, 8 hours, 16 hours after induction. They were then stained with antibodies for GFP and clients denoted in magenta. Representative confocal images are shown for each client and time point. White dashed boxes highlight zoomed-in regions. Scale bars: 10 µm (main panels), 2 µm (insets)

(B) Pearson correlation coefficient (PCC) analysis of client-scaffold colocalization. PCCs between PCM1 and client proteins were calculated from 3D images using Imaris Software (intensity/voxel-based). They represent colocalization analysis across 30 cells per condition in two independent experiments. The negative control, represented by the PCC between PCM1 and G3BP1 (0.032), indicates the lower detection limit of our colocalization. The positive control, between PCM1 and PCM1 (0.887), represents the upper limit of our colocalization detection.

(C) Classification of client recruitment dynamics based on colocalization strength. Recruitment time of each client to scaffold PCM1 was determined by comparing Pearson Correlation Coefficient (PCC) values relative to the 0-minute condition. Colocalization strength was classified as positive if the PCC value at 10 minutes was at least twice that at 0 minutes. Darker magenta color represents up-to 5 times increase in the PCC value compared to 0 minutes.

Figure 6

PCM1 and clients are organized into subdomains within CS granules.

(A) Spatial organization within the PCM1 granules. RPE1 cells were processed for U-ExM and stained for combinations of PCM1-C-Ab, PCM1-M-Ab and PCM1-N-Ab in green or magenta. Scale bars shown on the images are not adjusted for the expansion factor (4.2x). Insets display 10× magnifications of the cluster or individual CS. 3D representations are rendered from Leica Software. Scale bars: 2 µm (main panels), 200 nm, respectively (insets). Line profiles were drawn across individual PCM1 granules (shown in yellow arrow) and fluorescence intensity along the line was measured using plot profile analysis in ImageJ.

(B) Representative confocal images of expanded CS showing the spatial organization of PCM1 and its clients. RPE1 cells were processed for U-ExM and stained for clients (magenta) anti-CEP131, anti-MIB1, anti-KIAA0753 or anti-OFD1, and anti-PCM1-M-Ab / PCM1-C-Ab mixture (green). Scale bars shown on the images are not adjusted for the expansion factor (4.2x). Insets display10× magnifications of the cluster or individual CS. Blue arrow heads indicate the centrioles. Scale bars: 2 µm (main panels), 200 nm (insets). Line profiles (shown in yellow arrows) represent PCM1 (green) and clients (magenta).

(C) RPE1 cells were processed for U-ExM and stained for two clients at the same time (magenta or cyan) anti-CEP131, anti-MIB1, anti-KIAA0753 or anti-OFD1, and anti-PCM1-M-Ab / PCM1-C-Ab mixture (green). Scale bars shown on the images are not adjusted for the expansion factor (4.2x). Insets display10× magnifications of the cluster or individual CS. Arrows indicate the centrioles. Scale bars: 2 µm (main panels), 200 nm (insets).

(D) Spatial organization of PCM1-N and clients within CS granules with or without 1,6-Hexanediol treatment. Images show high magnification of GFP-PCM1-N granules colocalizing with various client proteins. RPE1::PCM1 KO cells inducibly expressing GFP-PCM1-N were induced for 24 hours, either treated with nothing or 5% 1,6-Hexanediol for 15 minutes and fixed and stained with anti-GFP-Ab (green) and clients (magenta). Cells were imaged using Zeiss Elyra 7 Lattice SIM superresolution microscope. Scale bars: 0.2 µm for images, 25 nm for insets.

(E) Quantification of client protein localization relative to PCM1-N granules. Line profiles were drawn across individual PCM1 N-terminal granules and fluorescence intensity along the line was measured using plot profile analysis in ImageJ. Distance between two peaks were used to determine the apparent diameter of the PCM1 signal the clients within the granule. For each granule, client measurements were normalized to the corresponding PCM1 diameter to allow comparison across granules of different sizes. Results are from three biological replicates, n > 30 cells per replicate for each client. Data are presented as mean ±SD.

(F) Table representation of (E). Client proteins were grouped based on their normalized diameter compared to PCM1 Diameter of PCM1 was set as the reference 1 value. Color coding represents spatial areas within the PCM1-N granule. Inner core (red), intermediate core (orange), core–shell interface (yellow), shell (light yellow), PCM1 reference (gray) and outer shell (blue). Proteins with smaller diameter values localize closer to the granule center, whereas larger values indicate localization toward PCM1-defined shell.

Figure 7

CS subdomains and granules have distinct compositions and biophysical properties

(A) Control and 1,6-hexanediol-treated HEK293T::PCM1 KO cells transfected with either FLAG or FLAG-PCM1 were lysed, and proteins were pulled down by Flag beads. The initial sample (initial) and pulled down proteins were run on an SDS gel and immunoblotted with antibodies against Flag-PCM1 and clients.

(B) RPE1 cells were treated with 5% 1,6-hexanediol for 10 min, fixed with methanol, and stained with antibodies against the indicated client proteins (green), PCM1 (magenta), centrin 3 (to mark the centrosome), and DAPI (to visualize DNA). A dual-secondary antibody labeling strategy was used to confirm PCM1 detection in both channels (top left panel). Cells in the bottom right panel were additionally treated with 50 mM sodium arsenate for 1 h to induce stress granules before 1,6-hexanediol treatment. Confocal microscopy was used for imaging. White boxes indicate zoomed-in regions. Scale bars: 10 µm (main panels), 5 µm (insets).

(C) Pearson correlation coefficient quantifying colocalization between PCM1 and client proteins during ciliogenesis. Small circles represent individual cells, while large squares indicate the average per experiment. Fold change is calculated by comparing the mean value of 1,6-hexanediol -treated samples to that of the control. Results are from two biological replicates, n = 40 cells per condition. Statistical significance was determined using a t-test comparing treatment and control for each colocalization pair (ns > 0.05, ****P < 0.0001).

(D) Pearson correlation coefficient quantifying colocalization between PCM1 and client proteins during Rnase treatment. Fold change is calculated by comparing the mean value of RNase-treated samples to that of the control. Data are from 40 cells per replicate, with two independent experiments. Statistical significance was determined using a t-test comparing treatment and control for each colocalization pair (ns > 0.05, **P < 0.01).

(E) Asynchronous and serum starved RPE1::mNeonGreen-CCDC66, RPE1::mNeonGreen-CSPP1 and RPE1::mNeonGreen-CEP104 cells were fixed with methanol, and stained with antibodies against mNeonGreen (green) and PCM1 (magenta). Additionally, asynchronous and serum starved RPE1 cells were fixed with methanol, and stained with antibodies against the indicated client proteins (green), PCM1 (magenta) and acetylated tubulin (cyan) (to mark the primary cilia). White boxes indicate zoomed-in regions. Scale bars: 10 µm (main panels), 1 µm (insets).

(F) Pearson correlation coefficients for quantifying colocalization between PCM1 and client proteins. Fold change is calculated by comparing the mean value of serum starved cells to the mean of asynchronous cells. Results are from two biological replicates, n = 30 cells per condition. Statistical significance was determined using a

t-test comparing treatment and control for each colocalization pair (ns > 0.05, **P < 0.01, ****P < 0.0001).

Figure 8

PCM1 exhibits intrinsic properties for granule formation, client sequestration, and microtubule binding *in vitro.*

(A) Schematic depicts the experimental flow. mNeonGreen-PCM1 condensates in a phase separation buffer at 1 µM, flown in chambers and imaged using a confocal microscope. Scale bar, 2 µm for field of view.

(B) mNeonGreen-PCM1 condensates in phase separation buffer at concentrations 1, 2, 3, 4 µM.

(C) Quantification of the number of condensates and volumes of each granule (μm^3) in the phase separation buffer from D. Results are from three biological replicates.

(D) mNeonGreen-PCM1, mScarlet-MIB1 and GST-mScarlet were set individually and combined in phase separation buffer, flown in chambers and imaged. Scale bar, 5 µm.

(E) Schematic depicts the experimental flow. Taxol stabilized microtubules polymerized from purified bovine tubulin labeled with Alexa Fluor 568 were attached on salinized and tubulin antibody coated cover slide surface. mNeonGreen-PCM1 was flown in a chamber and imaged with TIRF microscopy. Scale bar, 10 µm (main panels); 2 µm (insets).

(F) mNeonGreen-PCM1 and taxol-stabilized Rhodamine-labeled MTs and free tubulin were mixed in BRB80 buffer. They were introduced into flow chambers and imaged. Scale bars: 10 µm (main panels), 1 µm (insets).

(G) mNeonGreen-PCM1 and taxol-stabilized microtubules, polymerized from purified bovine tubulin and labeled with Alexa Fluor 568, were prepared in BRB80 buffer both individually and in combination. These were introduced into flow chambers and imaged. Scale bars: 10 µm (main panels), 1 µm (insets).

(H) Volume of mNeonGreen-PCM1 condensates plotted for each condition, with the y-axis on a log10 scale for the mNeonGreen-PCM1 only and the additive microtubules condition. Results are from two biological replicates, green and magenta colored dots representing different replicates.

(I) Microtubules promote CS assembly. Representative confocal images of RPE1::PCM1 KO cells inducibly expressing GFP-PCM1 treated with nocodazole. Cells were either treated with 5 µg/ml nocodazole for 2 hours before 1 µM doxycycline induction for 2 hours or with 5 µg/ml nocodazole for 1 hour, then with 5 ng/ml nocodazole and 1 µM doxycycline for 16 hours. Results are from two biological replicates, n=30 cells per replicate. Cells were fixed and stained for anti-GFP (green), anti-alpha tubulin 2 (magenta) and DAPI for nucleus (blue). Scale bar: 2 µm.

(J) Quantification of CS granule properties after nocodazole treatment from (D). Granule properties, including total volume of granules per cell (μm^3), average volume

of granules per cell (μm^3), total granule intensity, granule number and average distance of granules to centrosome (µm) values were measured using Imaris software. Centrosomes were identified using centrin 2 staining to quantify the distance values. Statistical significance was determined by the Student's t-test (paired and two-tailed). Results are from two biological replicates, green and magenta colored dots representing different replicates. n=30 cells cells per replicate. Data are presented as mean ±SD. *:P<0.05, **: P<0.01, ***:P<0.001, ****:P<0.0001; ns: not significant.

Supplementary Figure 1

Characterization of distinct PCM1 domains

(A) Quantification of the percentage of HeLa-WT and HeLa::PCM1 KO cells exhibiting distinct PCM1 localization patterns: granular, cytoplasmic, granular+cytoplasmic, and endogenous-like. Granular cells display no cytoplasmic localization and exhibit higher fluorescence intensity than the background signal. Endogenous-like refers to granules similar to endogenous CS granules, whereas granular describes granules that are larger and more heterogeneous in number. Data represent the mean percentage of cells from three biological replicates, totaling 100 cells. Data are presented as mean ±SD.

(B) Recruitment of endogenous PCM1 to fragment-induced granules. Representative confocal images of HeLa-WT cells transfected with GFP-PCM1 and its truncations. Cells are stained with anti-GFP (green), PCM1-C-Ab (magenta) or PCM1-M-Ab (magenta) and DAPI (blue). GFP-PCM1-NS, GFP-PCM1-N and GFP-PCM1-M recruit endogenous PCM1 into granules. Similar results were obtained from three biological replicates. Scale bars: 10 µm.

(C) Workflow of determining the relative protein concentration and critical saturation concentration. The schematic illustrates the process of transforming z-stack confocal images into three-dimensional voxels using Imaris software. This transformation was performed for two different volumetric representations: one combining both cytoplasmic and condensate volumes, and the other representing only the condensate volumes. Following rendering, the sum of intensities and the volume of the 3D voxels were quantified. These measurements were subsequently used to determine the relative protein concentrations within the light and dense phases.

(D) Localization of PCM1 and its truncation mutants at increasing concentrations in HeLa-WT cells. These cells are transfected with GFP fusions of PCM1, PCM1-N, PCM1-M, PCM1-NS and PCM1-C for 48 hours, fixed and stained with anti-GFP. The images indicate the cells with increasing expression levels of PCM1 and its truncations, indicated by a green triangle at the top.

(E) Quantification of the threshold concentrations at which granules formed for PCM1 and its truncations from (D). For each transfected cell, intensity of GFP signal and total volume and intensity of granules and cytoplasm were measured using Imaris Software. Threshold concentration denotes the mean value of granular concentration values. Green bars represent average concentration of granule forming cells. Pink bars represent the maximum and minimum values of granule forming cell concentration. Results are from three biological replicates, min 48 cells in total. Data are presented as mean ±SD. a.u.: arbitrary unit.

Supplementary Figure 2

Characterization of CS spatiotemporal dynamics and function in the chemically inducible dimerization system.

(A) Still images depicting the behavior of CS granules upon treatment with dimerizer or washout ligand in RPE1::PCM1-KO cells stably expressing mNG-PCM1-FKBP(F36V). Live imaging was conducted at one-minute intervals for the first hour, followed by 20-minute intervals thereafter. Scale bar: 30 µm.

(B) FRAP analysis on RPE1::PCM1 KO cells inducibly expressing mNG-PCM1-FKBP(F36V) with or without dimerizer addition for either 2 hours or 16 hours. The specified regions were photobleached and subsequently imaged for 300 seconds post-bleaching. Scale bars: 1 µm. Quantification of mobile pool and half-time of fluorescence recovery is shown on graphs. Mobile fractions of fluorescence recovery were calculated based on granule recovery (n = 3 independent FRAP experiments from three biological replicates). Triangles indicate the mean values for each replicate.

(C) Representative confocal images of RPE1::PCM1 KO cells inducibly expressing mNG-PCM1-FKBP(F36V) with or without dimerizer addition to either No treatment (NT) or 1,6-HD treatment. After 1 h of dimerization, cells were treated with 5% 1,6-HD for 5 minute, whereas control cells were fixed after 5 minutes. Images show that 1,6-HD addition causes a reduction in intensity and granule number in No-treatment condition. On the other hand, 1,6-HD doesn't have an effect on dimerized granules showing the reduction in dynamicity upon dimerization. Cells were fixed and stained for anti-mNG (green) and nucleus (blue). Scale bar: 10 µm.

(D) Effects of CS dimerization on ciliogenesis and cilium length. Representative images depict ciliated RPE1::PCM1 KO cells stably expressing mNG-PCM1-FKBP(F36V) after treatment with dimerizer and subsequent wash-out ligand in serum-depleted medium for 24 hours. Cells were fixed and stained for mNeonGreen and acetylated tubulin. Scale bars: 20 µm (main panels), 5 µm (insets).

(E, F) Quantification of (E) ciliation percentage and (F) cilium length in control, dimerizer-treated, and wash-out ligand-treated cells 24 hours after serum starvation. The data represent three biological replicates, green, magenta and orange colored dots representing different replicates, with n = 35 per replicate. Data are presented as mean ±SD.

(G) Representative images and quantification of chromosome congression index for No-treatment (NT) and dimerizer conditions in RPE1::PCM1-KO cells stably expressing mNG-PCM1-FKBP(F36V). For images scale bars: 10 µm. Results are from three biological replicates, n=15 cells per replicate. Cells were fixed and stained for anti-mNeonGreen (green), anti-alpha tubulin 2 (magenta) and DAPI for nucleus (blue).

(H) Quantification of percentage of multinucleated RPE1::PCM1-KO cells stably expressing mNG-PCM1-FKBP(F36V) in each cell cycle phase in both No-treatment (NT) and dimerizer treated conditions. Quantifications were done using the images from S2F. Results are from three biological replicates, n=25 cells per replicate. Data are presented as mean ±SD.

Supplementary Figure 3

Generation and validation of inducible cells for *de novo* CS biogenesis assay and their functional characterization in ciliogenesis and signaling.

(A) Validation of inducible cell lines by immunofluorescence. Representative confocal images of RPE1::PCM1 KO cells inducibly expressing GFP-PCM1, GFP-PCM1-N and GFP-PCM1-M fixed and stained after 16 hours of induction. Cells were stained with anti-GFP-Ab (green), anti-PCM1-M-Ab (magenta) and DAPI (blue). Scale bar: 5 µm.

(B, C, D) Quantification of expression levels of inducible cell lines by immunoblotting compared to wild-type PCM1. Immunoblot analysis of RPE1::PCM1 KO inducible cell lines expressing GFP-PCM1 (B), GFP-PCM1-N (C) and GFP-PCM1-M (D). Cell lines were induced with doxycycline for 1, 2, 4, 8 and 16 hour and lysates were prepared along with non-induced control (0 h) and lysate from wild-type RPE1 cells. Proteins were detected using anti-PCM1 antibody and either vinculin or alpha-tubulin as loading controls. Quantification was done by normalizing wild-type lysate band to 1 for each replicate. Each band was also normalized to it's loading control. Results are from two biological replicates. Dotted lines in (B) and (C) mark cropped area corresponding to empty lanes that were not relevant to the experiment. The entire membrane was processed and imaged under identical conditions, no image processing, rearrangement or alteration of signal intensity was performed. Red lines represent the value 1. Fold change written below each blot represents relative protein level fold change compared to wild-type levels.

Supplementary Figure 4

Phenotypic rescue experiments on inducible lines in ciliation efficiency and cilium length.

(A) RPE1::PCM1 KO cells inducibly expressing GFP-PCM1, GFP-PCM1-N and GFP-PCM1-M were induced by doxycycline for 48 hours, then serum starved for 48 hours. RPE1-WT and RPE1::PCM1 KO cells were serum starved for 48 hours. Cells were fixed and stained with anti-GFP (green), anti-acetylated tubulin (magenta), and DAPI for nucleus(blue). The percentage of ciliated cells was determined from acetylated tubulin signals. Scale bars: 10 µm (main panels), 2 µm (insets).

(B) Quantification of ciliation percentage from (A). Only GFP-positive cells were chosen for the quantification. Data represents the mean from n>40 cells per replicate and three biological replicates. Data are presented as mean ±SD. ***: P<0.001; ns: not significant.

(C) Quantification of cilium length from (A). Only GFP-positive cells were chosen for the quantification. Data represents the mean from n>40 cells per replicate and three biological replicates, green, magenta and orange colored dots representing different replicates. Data are presented as mean ±SD. ***: P<0.001; ns: not significant.

(D) Experiments to assess phenotypic rescue in Hedgehog pathway activation. RPE1::PCM1 KO cells, which inducibly express GFP-PCM1 and GFP-PCM1-N, were treated with doxycycline for 48 hours, then serum-starved for 24 hours, and subsequently treated with 500 nM SAG in serum starvation medium for 24 hours. In parallel, RPE1-WT cells were serum-starved for 24 hours and subsequently treated with 500 nM SAG for 24 hours. Basal activation levels were determined by processing control cells that were not treated with SAG (SAG-). All cells were fixed and stained for GFP (green), Smo (magenta), acetylated tubulin (cyan), and DAPI (blue). Scale bars: 2 µm.

(E) Quantification of Smo recruitment to the cilium as shown in (J). Smo intensity at the cilium was calculated using ImageJ. Only GFP-positive cells were selected for quantification. The data represent the mean from three biological replicates, with n>55 cells per replicate, green, magenta and orange colored dots representing different replicates. Data are presented as mean ±SD. *:P<0.05, **:P<0.01, ***:P<0.001, ****:P<0.0001; ns: not significant.

(F) Experiments to assess phenotypic rescue in recruitment of IFT88 to the cilium and basal body. RPE1::PCM1 KO cells inducibly expressing GFP-PCM1 and GFP-PCM1-N were treated with doxycycline for 48 hours, then serum-starved for 48 hours. In parallel, RPE1-WT cells were serum-starved for 48 hours. All cells were fixed and stained for GFP (green), IFT88 (magenta), acetylated tubulin (cyan), and DAPI (blue). Scale bar: 2 µm.

(G) Quantification of ciliary and centrosomal IFT88 levels from (L). The results shown represent the mean of three independent experiments. The basal body signal was measured from a 3 μm^2 area centered on the centrosome, as identified by the

acetylated tubulin signal. Data are presented as the mean from three biological replicates, with n>55 cells per replicate, green, magenta and orange colored dots representing different replicates. Data are presented as mean ±SD.

Supplementary Figure 5

Spatiotemporal analysis of CS granule properties during mitosis.

(A) Workflow for quantifying CS granule properties. PCM1 granule characteristics were analyzed in both fixed and live-cell images using Imaris software. The analysis was conducted in 3D, with quantifications performed post 3D rendering. Cells were segmented individually per the 'one cell per nucleus' rule using the cell creation tool. The surface creation tool was used to render PCM1 granules, incorporating background subtraction and manual thresholding for granule detection. Centrosomes were identified using centrin-2 or gamma tubulin channels using the spot creation tool, set to a 1 µm XY diameter. All three segmented components were combined to form a 3D rendered image, from which granule properties (volume, fluorescence intensity, average distance from the centrosome) were quantified.

(B) Spatiotemporal analysis of *de novo* assembled PCM1 granules during mitosis. Representative still frames from time-lapse confocal images show RPE1::PCM1 KO cells inducibly expressing GFP-PCM1, GFP-PCM1-N, and GFP-PCM1-M. Cells were imaged after the addition of 1 µM doxycycline and SIR-tubulin. Imaging was conducted every 1.5 minute over 144 minutes. Time "0 min" marks the start of granule nucleation. Red colored time points represent the start of mitosis (GFP-PCM1: 55 min, GFP-PCM1-N-60 min, GFP-PCM1-M:51 min). Centrosomes are indicated by cyan arrows at each time point, and cell boundaries are outlined with white dashed lines. Scale bars: 5 µm.

(C) Quantification of size, fluorescence intensity and number of PCM1 granules from (B). Average distance to centrosome values were quantified from the distance between granules and SIR-tubulin staining for each cell. Images were taken in 1.5 minute intervals for 144 minutes. Mitosis is shown with faded colors for each quantification. Data represents the mean from quantifications from a cell for each line. Results were consistent with three independent experiments. Data are presented as mean ±SD.

Supplementary Figure 6

Spatiotemporal analysis of client recruitment to scaffolds formed by PCM1-N and PCM1-M during CS biogenesis.

(A) Representative images for co-localization of various CS clients with the PCM1-N scaffold in a *de novo* biogenesis assay. RPE1::PCM1 KO cells inducibly expressing GFP-PCM1-N were fixed before induction and 30 min, 2 hours, 8 hours, 16 hours after induction. They were then stained with antibodies for GFP and clients denoted in magenta. Representative confocal images are shown for each client and time point. White dashed boxes highlight zoomed-in regions. Scale bars: 10 µm (main panels), 2 µm (insets).

(B) Pearson correlation coefficient (PCC) analysis of client-scaffold colocalization. PCCs between PCM1-N and client proteins were calculated from 3D images using Imaris Software. They represent colocalization analysis across 30 cells per condition in two independent experiments. The negative control, represented by the PCC between PCM1 and G3BP1 (0.032), indicates the lower detection limit of our colocalization. The positive control, between PCM1 and PCM1 (0.887), represents the upper limit of our colocalization detection.

(C) Classification of client recruitment dynamics based on colocalization strength for B. Recruitment time of each client to scaffold PCM1 was determined by comparing Pearson Correlation Coefficient (PCC) values relative to the 0-minute condition. Colocalization strength was classified as positive if the PCC value at 10 minutes was at least twice that at 0 minutes. Darker magenta color represents up-to 5 times increase in the PCC value compared to 0 minutes.

D) Representative images for co-localization of various CS clients with the PCM1-M scaffold in a *de novo* biogenesis assay. RPE1::PCM1 KO cells inducibly expressing GFP-PCM1-M were fixed before induction and 4 hours and 16 hours after induction. They were then stained with antibodies for GFP and clients denoted in magenta. Representative confocal images are shown for each client and time point. White dashed boxes highlight zoomed-in regions. Scale bars: 10 µm (main panels), 2 µm (insets).

Supplementary Figure 7

PCM1 and clients are organized into subdomains in U2OS cells. (A, B, C)

Validation of antibodies targeting distinct regions of PCM1 by immunofluorescence in PCM1 KO cells expressing specific PCM1 fragments. The specificity of PCM1 antibodies for the N-terminal 1-254 aa (PCM1-N-Ab), middle region 700-1200 aa (PCM1-M-Ab), and C-terminus 1664-2024 aa (PCM1-C-Ab) was confirmed through immunofluorescence experiments. Representative confocal images show HeLa::PCM1 KO cells transfected with GFP-PCM1-N, GFP-PCM1-M, GFP-PCM1-NS, and GFP-PCM1-C plasmids for 24 hours. Cells were fixed with 4% PFA and stained for GFP (green) along with various combinations of antibodies: (A) PCM1-M-Ab (magenta), PCM1-C-Ab (cyan); (B) PCM1-N-Ab (magenta), PCM1-M-Ab (cyan); (C) PCM1-N-Ab (magenta), PCM1-C-Ab (cyan). Scale bars: 10 µm

(D) Validation of antibodies targeting distinct regions of PCM1 by immunoblotting in PCM1 KO cells expressing specific PCM1 fragments. HEK293T::PCM1 KO cells were transfected with GFP-PCM1-FL, GFP-PCM1-N, GFP-PCM1-C, GFP-PCM1-M, and GFP-PCM1-NS plasmids for 48 hours. Following transfection, cells were lysed, and the samples were subjected to SDS-PAGE and immunoblotting. The samples were then blotted with PCM1-N-Ab, PCM1-C-Ab, or PCM1-M-Ab.

(E) Spatial organization within the PCM1 granules. U2OS cells were processed for U-ExM and stained for combinations of PCM1-C-Ab, PCM1-M-Ab and PCM1-N-Ab in green or magenta. Scale bars shown on the images are not adjusted for the expansion factor (4.2x). Insets display 10× magnifications of the cluster or individual CS. 3D representations are rendered from Leica Software. Scale bars: 2 µm (main panels), 200 nm, respectively (insets).

(F) U2OS cells were processed for U-ExM and stained for two clients at the same time (magenta or cyan) anti-CEP131, anti-MIB1, anti-KIAA0753 or anti-OFD1, and anti-PCM1-M-Ab / PCM1-C-Ab mixture (green). Scale bars shown on the images are not adjusted for the expansion factor (4.2x). Insets display10× magnifications of the cluster or individual CS. Arrows indicate the centrioles. Scale bars: 2 µm (main panels), 200 nm (insets).

Supplementary Figure 8

The PCM1 scaffold and its clients are spatially organized into subdomains within CS granules.

(A) Spatial organization of PCM1-N and various CS client proteins revealed by super-resolution microscopy. High-magnification images show granules formed by GFP-PCM1-N colocalizing with different client proteins in RPE1::PCM1-KO cells after doxycycline induction for 24 hours. After fixation, cells were stained with anti-GFP antibody (green) and client proteins (magenta), then imaged using a Zeiss Elyra 7 Lattice SIM super-resolution microscope. Granules with varying diameters, indicated on the left side of each image, were selected as representative. Intensity plot profiles were generated along the yellow arrows for each granule using ImageJ. In the graphs, green represents the fluorescent intensity of PCM1, and magenta represents that of the client proteins. Similar results were obtained from three biological replicates. Scale bars: 0.2 µm.

(B) Spatial organization of PCM1-N and Ninein at different induction time points revealed by super-resolution microscopy. High-magnification images show granules formed by GFP-PCM1-N colocalizing with Ninein in RPE1::PCM1-KO cells after doxycycline induction for indicated time points: 30 min, 1 h, 2 h, 4 h, 8 h and 16 h. After fixation, cells were stained with anti-GFP antibody (green) and Ninein (magenta), then imaged using a Zeiss Elyra 7 Lattice SIM super-resolution microscope. Granules with average size in the corresponding time point were selected as representative. Same parameters and laser power values were used for imaging and image analysis. Intensity plot profiles were generated along the yellow arrows for each granule using ImageJ. In the graphs, green represents the fluorescent intensity of PCM1 and magenta represents that of the client proteins. Similar results were obtained from three biological replicates. Scale bar: 0.2 µm.

Supplementary Figure 9

Colocalization index of PCM1 and clients after DNA damage and different client colocalization of GFP-PCM1 and GFP-PCM1-N during ciliogenesis.

(A) Representative confocal images of co-localization between PCM1 and various clients before and after etoposide treatment. RPE1 cells were treated with 25 uM etoposide for 24 hours, then fixed and stained with antibodies against client proteins (green), PCM1 (magenta), centrin 3 (cyan), and DAPI (blue). White boxes indicate zoomed-in regions. Scale bars: 10 μm (main panels), 5 μm (insets).

(B) Pearson correlation coefficient quantifying colocalization between PCM1 and client proteins after etoposide treatment. Fold change is calculated by comparing the mean value of RNase-treated samples to that of the control. Small circles represent individual cells, while large squares indicate the average per experiment. Data are from 40 cells per replicate, with two independent experiments. Statistical significance was determined using a t-test comparing treatment and control for each colocalization pair (ns > 0.05, **P < 0.01).

(C) Representative images of RPE1::PCM1 KO cells inducibly expressing GFP-PCM1 and GFP-PCM1-N induced by doxycycline for 24 hours, then serum starved for 48 hours. Cells were fixed and stained with anti-GFP (green), anti-CEP290 (magenta), anti-Arl13b (cyan) and DAPI for nucleus(blue). Scale bars: 10 μm (main panels), 2 μm (insets).

(D) Quantification of Pearson correlation coefficient quantifying colocalization between PCM1 and CEP290 staining from (C). Data are from at least 30 cells per replicate, with three independent experiments. Statistical significance was determined using a t-test comparing Non-ciliated and ciliated cells from same images. Green, magenta and orange colored dots represent different replicates. Data are presented as mean ±SD. ns > 0.05, ****P < 0.0001.

(E) Representative images of RPE1::PCM1 KO cells inducibly expressing GFP-PCM1 and GFP-PCM1-N induced by doxycycline for 24 hours, then serum starved for 48 hours. Cells were fixed and stained with anti-GFP (green), anti-MIB1 (magenta), anti-Arl13b (cyan) and DAPI for nucleus(blue). Scale bars: 10 μm (main panels), 2 μm (insets).

(F) Quantification of Pearson correlation coefficient quantifying colocalization between PCM1 and MIB1 staining. Data are from at least 30 cells per replicate, with three independent experiments. Statistical significance was determined using a t-test comparing Non-ciliated and ciliated cells from same images. Green, magenta and orange colored dots represent different replicates. Data are presented as mean ±SD. ns > 0.05

Supplementary Figure 10

Characterization of biophysical properties of CS.

(A) Confirmation of His-MBP-mNG-PCM1 purification. Analysis of purified mNeonGreen-PCM1 separated by SDS-PAGE and either stained with Coomassie dye or immunoblotted with PCM1-C Ab. Arrow indicates full-length PCM1 band.

(B) Confirmation of His-MBP-mNG-PCM1 purification by immunofluorescence. mNeonGreen-PCM1 condensates in phase separation buffer were fixed with 15 % glutaraldehyde, spun on cover slips, fixed with 4% PFA and stained for PCM1 N-term and C-term specific antibodies. 3D images were exported from Imaris software. Scale bar: 5 µm.

(C) PSM, abundance and normalized abundance values from mass spectrometry analysis of purified His-MBP-mNG-PCM1. Abundance of PCM1was normalized to 100% to calculate the other proteins detected from mass spectrometry.

(D) Confirmation of His-MBP-mNG-PCM1 purification by mass spectrometry. Mass spectrometry analysis of purified mNeonGreen-PCM1 for peptide coverage marked on the 2024 aa long human protein sequence. The negative gradient of purple to yellow indicates peptide regions that have been identified 0-10 times on the sequence where purple indicates 0 and yellow indicates 10.

(E) Analysis of His-MBP-mNG tag as a control in phase separation experiments. Purified His-MBP-mNG in phase separation buffer at concentrations 1 and 2 µM observed as soluble protein for control of specificity of PCM1-mediated phase separation. Scale bar: 10 µm.

(F) Confirmation of His-MBP-mScarlet MIB1 purification. Analysis of purified mScarlet-MIB1 separated by SDS-PAGE and immunoblotted with MIB1 Ab. Arrow indicates full-length MIB1 band.

(G) Effect of 10% polyethylene glycol (PEG) crowding agent on phase separation behavior of PCM1 *in vitro*. 1 µM mNeonGreen-PCM1 condensation were induced in phase separation buffer supplemented with 10% polyethylene glycol. Scale bars: 10 µm (upper panel), 5 µm (lower panel).

(H) mNeonGreen-PCM1, and taxol stabilized microtubules polymerized from purified bovine tubulin labeled with Alexa Fluor 568 were set in BRB80 buffer, flown in chambers and imaged. Scale bar, 10 µM for field of view at single z-stack; 2 µM for inset. mNeonGreen-PCM1 and taxol-stabilized microtubules, polymerized from purified bovine tubulin labeled with Alexa Fluor 568, were prepared in BRB80 buffer, introduced into chambers, and imaged. Insets represent specific z-stacks to highlight the spatial organization of PCM1-N. Scale bars: 10 µm (main panels), 2 µm (insets).

(I) PCM1-N granule assembly in nocodazole-treated cells using de novo biogenesis assay. RPE1::PCM1 KO cells inducibly expressing GFP-PCM1-N were pre-treated

with nocodazole prior to the initiation of doxycycline induction. Cells were treated with 5 µg/ml nocodazole for one hour followed by 1 µM doxycycline induction and were visualized by time-lapse imaging. Still images from a representative time-lapse movie are depicted. The timepoint labeled '0 min' denotes the start of granule nucleation. Scale bar: 2 µm

Video 1. Time-lapse confocal microscopy imaging of CS granule (green) behavior during mitosis in control RPE1::PCM1 KO cells stably expressing mNG-PCM1-FKBP(F36V). SiR-tubulin was added to visualize microtubules (magenta). Live imaging was conducted for at least 12 hours, each frame being 3 minutes. Scale bar: 10 μm. Video is 10 frames/second. 0 min represents the start of mitosis. Video is associated with Fig. 2G.

Video 2. Time-lapse confocal microscopy imaging of CS granule (green) behavior during mitosis in dimerizer treated RPE1::PCM1 KO cells stably expressing mNG-PCM1-FKBP(F36V) with multiple granules. SiR-tubulin was added to visualize microtubules (magenta). Live imaging was conducted for at least 12 hours, each frame being 2.5 minutes. Scale bar: 10 μm. Video is 10 frames/second. 0 min represents the start of mitosis. Video is associated with Fig. 2G.

Video 3. Time-lapse confocal microscopy imaging of CS granule (green) behavior during mitosis in dimerizer treated RPE1::PCM1 KO cells stably expressing mNG-PCM1-FKBP(F36V) with single granule. SiR-tubulin was added to visualize microtubules (magenta). Live imaging was conducted for at least 12 hours, each frame being 1.5 minutes. Scale bar: 10 μm. Video is 10 frames/second. 0 min represents the start of mitosis. Video is associated with Fig. 2G.

Video 4. Time-lapse confocal microscopy imaging of CS granule (green) behavior during mitosis in dimerizer treated RPE1::PCM1 KO cells stably expressing mNG-PCM1-FKBP(F36V) with single granule. SiR-tubulin was added to visualize microtubules (magenta). Live imaging was conducted for at least 12 hours, each frame being 1.5 minutes. Scale bar: 10 μm. Video is 10 frames/second. 0 min represents the start of mitosis. Video is associated with Fig. 2G.

Video 5. Time-lapse confocal imaging of RPE1::PCM1 KO cells inducibly expressing GFP-PCM1 (green). SiR-tubulin was added to visualize microtubules (magenta).Cells were imaged following the addition of 1 μM doxycycline. 0 min represents the start of imaging. Live imaging was conducted for at least 10 hours, each frame being 3

minutes. Scale bar: 5 μm. Video is 10 frames/second. Video shows a representative cell for Figure 3D.

Video 6. Time-lapse confocal imaging of RPE1::PCM1 KO cells inducibly expressing GFP-PCM1-N (green). SiR-tubulin was added to visualize microtubules (magenta).Cells were imaged following the addition of 1 μM doxycycline. 0 min represents the start of imaging. Live imaging was conducted for at least 10 hours, each frame being 3 minutes. Scale bar: 5 μm. Video shows a representative cell for Figure 3D.

Video 7. Time-lapse confocal imaging of RPE1::PCM1 KO cells inducibly expressing GFP-PCM1-M (green). SiR-tubulin was added to visualize microtubules (magenta).Cells were imaged following the addition of 1 μM doxycycline. 0 min represents the start of imaging. Live imaging was conducted for at least 10 hours, each frame being 3 minutes. Scale bar: 5 μm. Video shows a representative cell for Figure 3D.

Video 8. Time-lapse confocal imaging of RPE1::PCM1 KO cells inducibly expressing GFP-PCM1 (green) during mitosis. SiR-tubulin was added to visualize microtubules (magenta).Cells were imaged following the addition of 1 μM doxycycline. 0 min represents the start of imaging. Live imaging was conducted for at least 10 hours, each frame being 3 minutes. Scale bar: 5 μm. Video is 10 frames/ second. Video shows a representative cell for Figure S5C.

Video 9. Time-lapse confocal imaging of RPE1::PCM1 KO cells inducibly expressing GFP-PCM1-N (green) during mitosis. SiR-tubulin was added to visualize microtubules (magenta).Cells were imaged following the addition of 1 μM doxycycline. 0 min represents the start of imaging. Live imaging was conducted for at least 10 hours, each frame being 3 minutes. Scale bar: 5 μm. Video is 10 frames/ second. Video shows a representative cell for Figure S5C.

Video 10. Time-lapse confocal imaging of RPE1::PCM1 KO cells inducibly expressing GFP-PCM1-M (green) during mitosis. SiR-tubulin was added to visualize microtubules (magenta).Cells were imaged following the addition of 1 μM doxycycline. 0 min represents the start of imaging. Live imaging was conducted for at least 10 hours, each frame being 3 minutes. Scale bar: 5 μm. Video is 10 frames/second. Video shows a representative cell for Figure S5C.

Figure 1

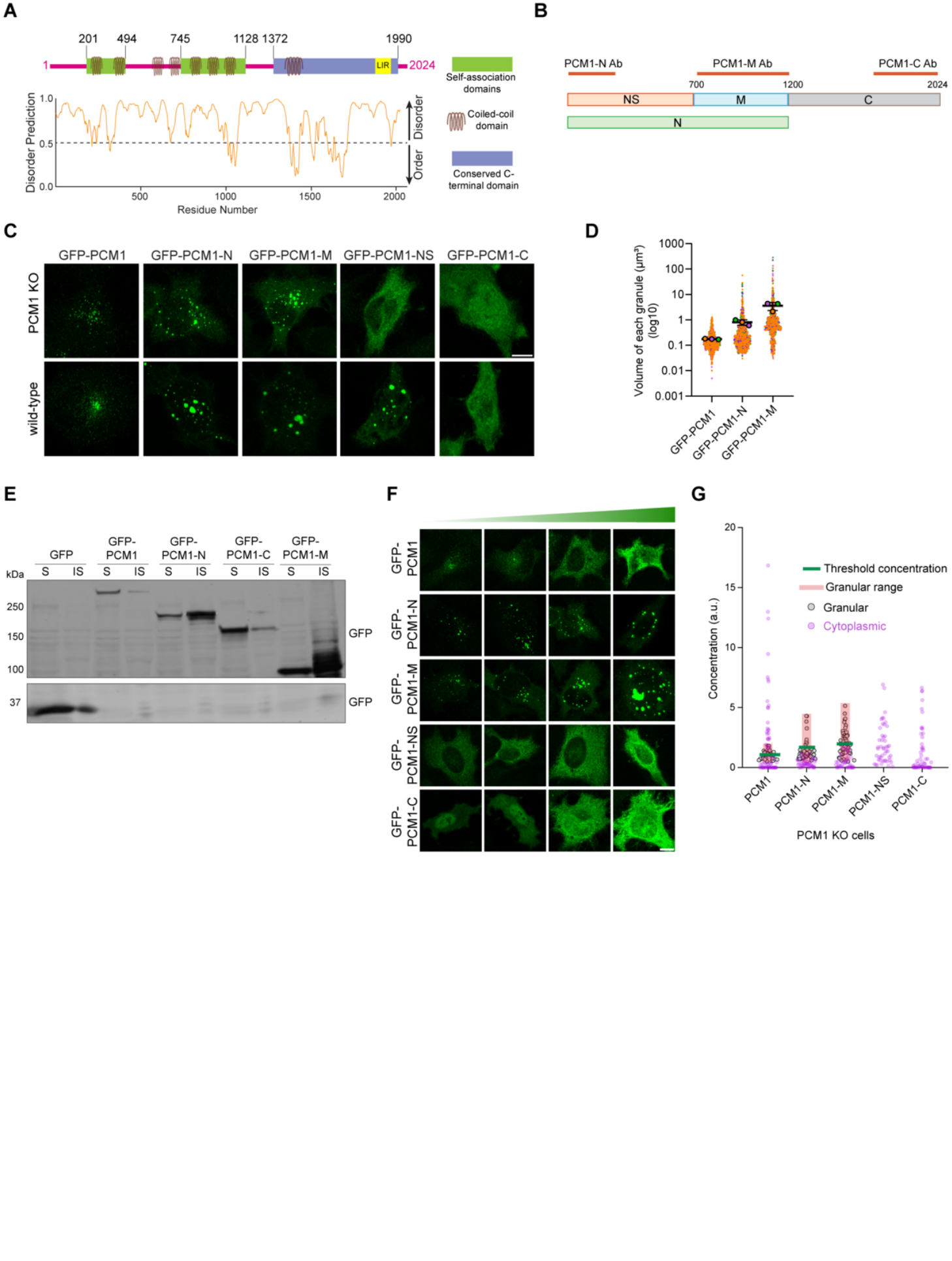

A
201
494
745
1128 1372
1990
1
2024
LIR
Self-association domains
Coiled-coil domain
Conserved C-terminal domain
Disorder Prediction
1.0
0.5
0.0
Disorder
Order
500
1000
1500
2000
Residue Number
B
PCM1-N Ab
PCM1-M Ab
PCM1-C Ab
700
1200
2024
NS
M
C
N
C
GFP-PCM1
GFP-PCM1-N
GFP-PCM1-M
GFP-PCM1-NS
GFP-PCM1-C
PCM1 KO
wild-type
D
Volume of each granule (μm³) (log10)
1000
100
10
1
0.1
0.01
0.001
GFP-PCM1
GFP-PCM1-N
GFP-PCM1-M
E
GFP
GFP-PCM1
GFP-PCM1-N
GFP-PCM1-C
GFP-PCM1-M
S
IS
kDa
250
150
100
37
GFP
GFP
F
GFP-PCM1
GFP-PCM1-N
GFP-PCM1-M
GFP-PCM1-NS
GFP-PCM1-C
G
Threshold concentration
Granular range
Granular
Cytoplasmic
Concentration (a.u.)
20
15
10
5
0
PCM1
PCM1-N
PCM1-M
PCM1-NS
PCM1-C
PCM1 KO cells

Figure 2

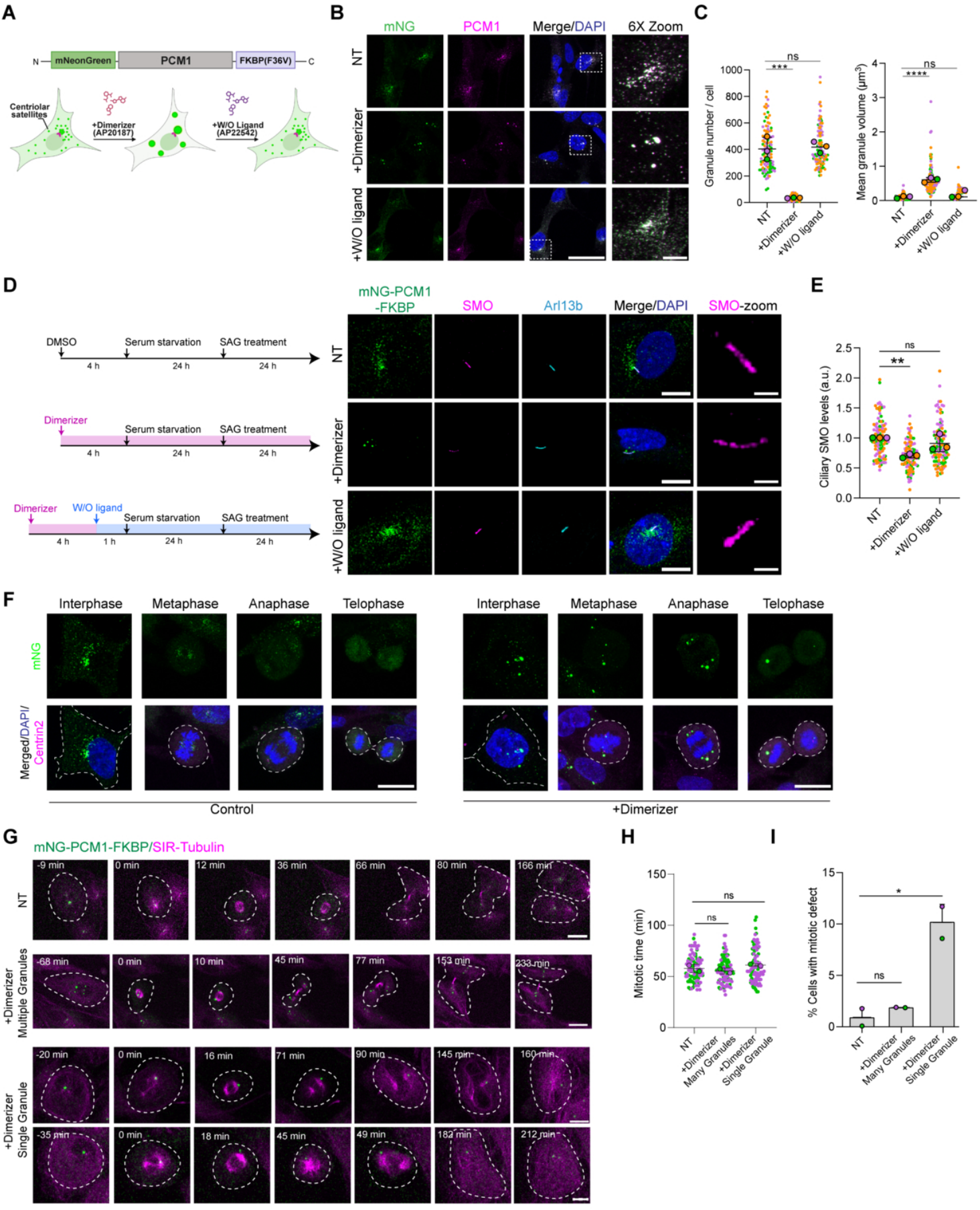

A
N
mNeonGreen
PCM1
FKBP(F36V)
C
Centriolar satellites
+Dimerizer (AP20187)
+W/O Ligand (AP22542)
B
mNG
PCM1
Merge/DAPI
6X Zoom
NT
+Dimerizer
+W/O ligand
C
Granule number / cell
Mean granule volume (µm³)
ns
***
****
NT
+Dimerizer
+W/O ligand
D
mNG-PCM1 -FKBP
SMO
Arl13b
Merge/DAPI
SMO-zoom
DMSO
Serum starvation
SAG treatment
4 h
24 h
Dimerizer
W/O ligand
1 h
E
Ciliary SMO levels (a.u.)
**
F
Interphase
Metaphase
Anaphase
Telophase
mNG
Merged/DAPI/ Centrin2
Control
+Dimerizer
G
mNG-PCM1-FKBP/SIR-Tubulin
+Dimerizer Multiple Granules
+Dimerizer Single Granule
H
Mitotic time (min)
+Dimerizer Many Granules
+Dimerizer Single Granule
I
% Cells with mitotic defect
*

Figure 3

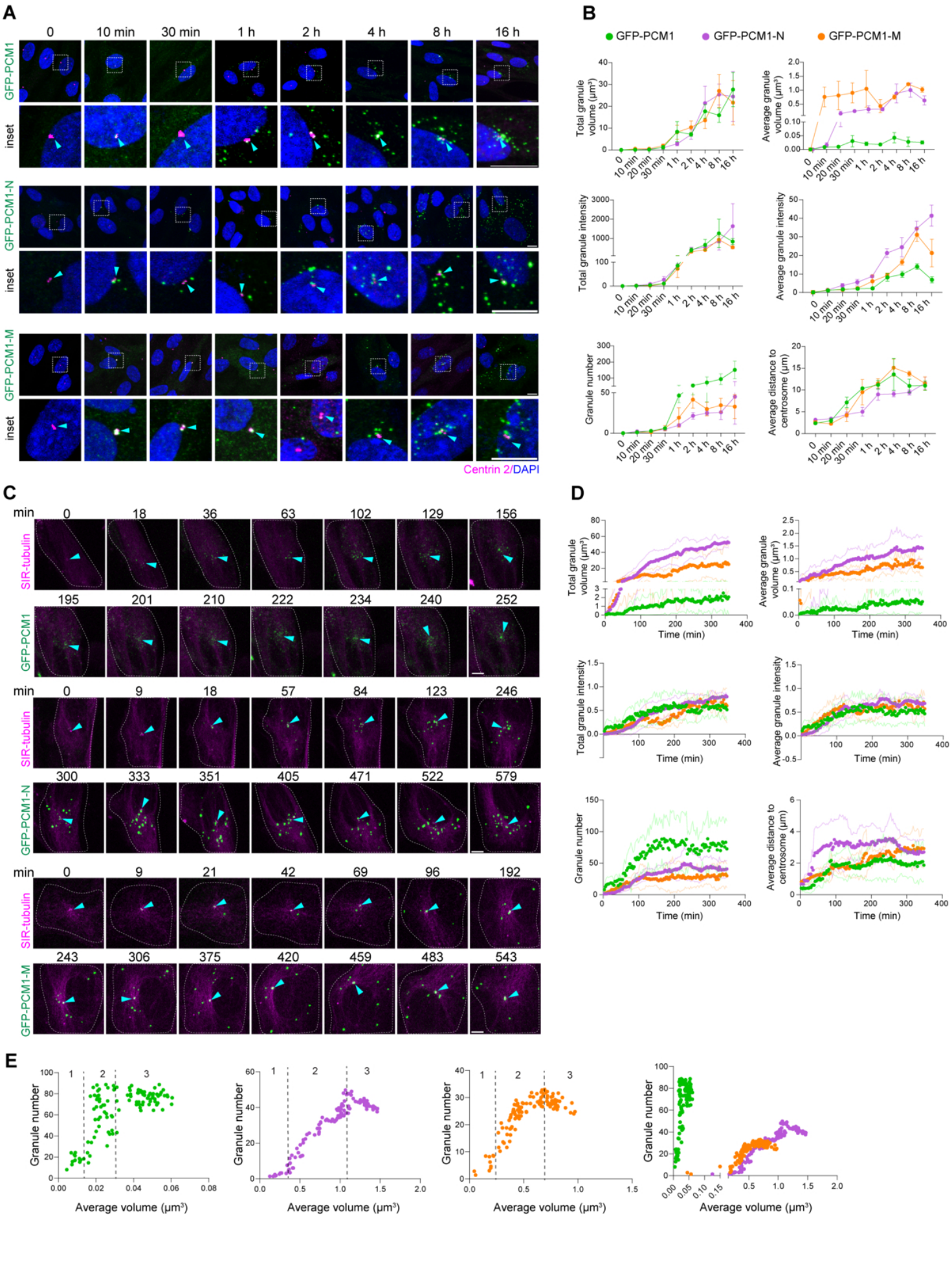

A
0
10 min
30 min
1 h
2 h
4 h
8 h
16 h
GFP-PCM1
GFP-PCM1-N
GFP-PCM1-M
inset
Centrin 2/DAPI
B
GFP-PCM1
GFP-PCM1-N
GFP-PCM1-M
Total granule volume (µm³)
Average granule volume (µm³)
Total granule intensity
Average granule intensity
Granule number
Average distance to centrosome (µm)
C
min
SIR-tubulin
GFP-PCM1
GFP-PCM1-N
GFP-PCM1-M
D
Time (min)
E
Granule number
Average volume (µm³)

Figure 4

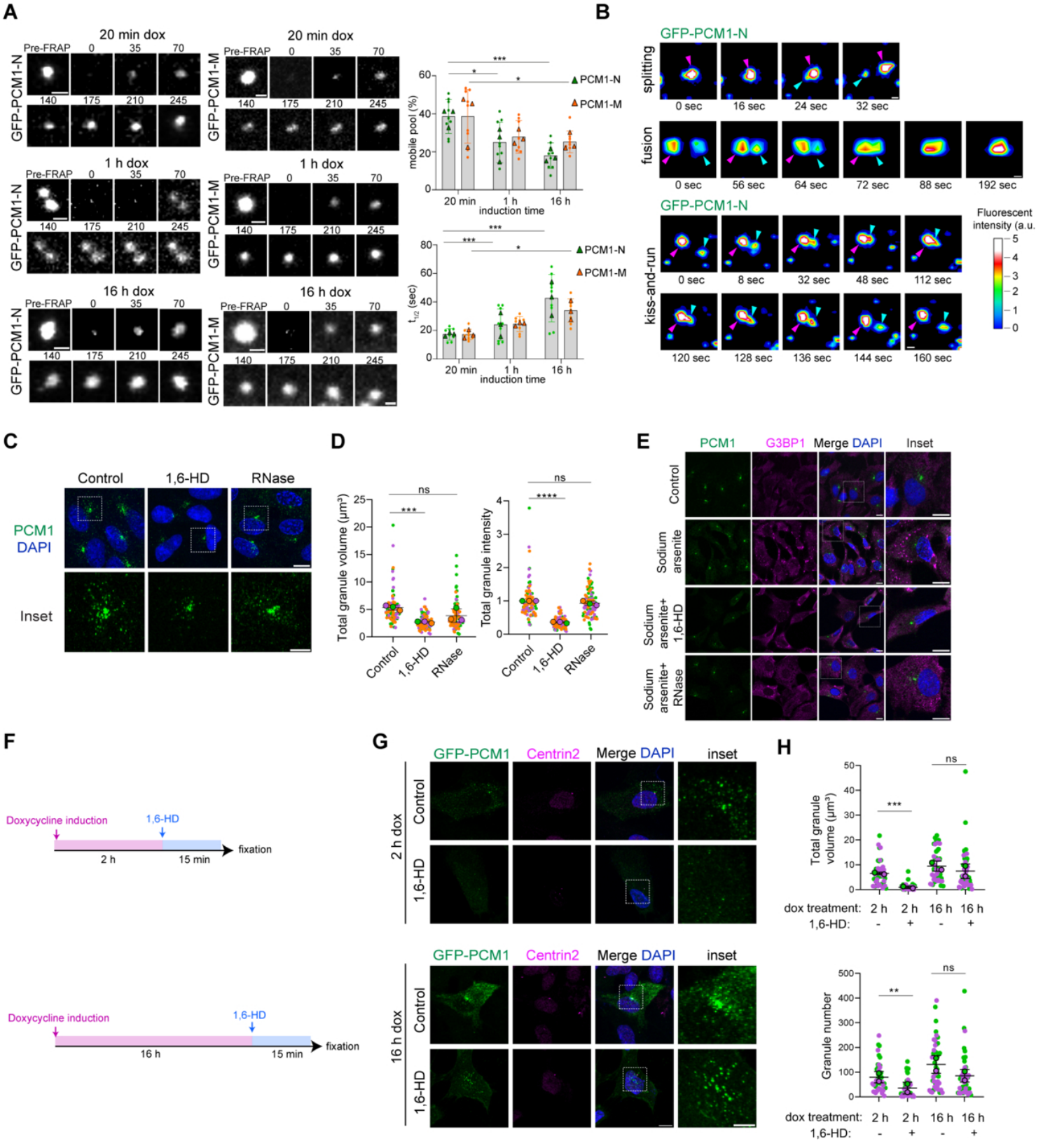
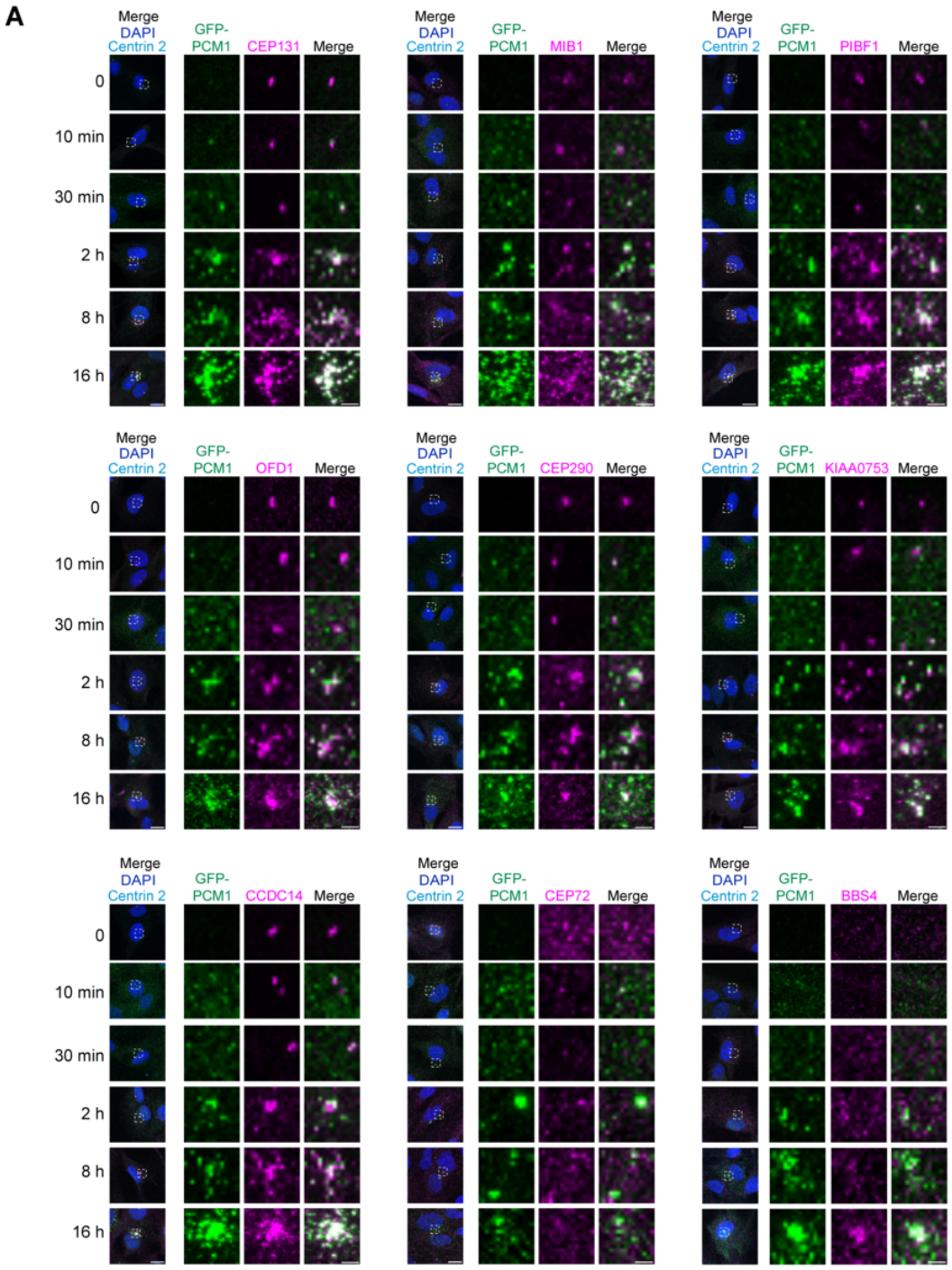
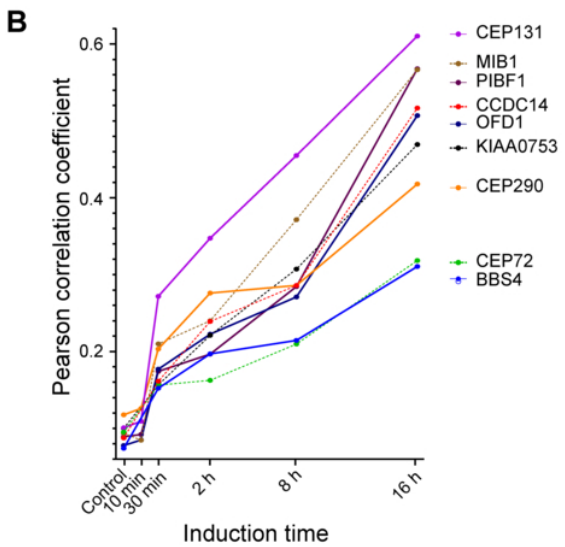

A
20 min dox
1 h dox
16 h dox
Pre-FRAP
GFP-PCM1-N
GFP-PCM1-M
mobile pool (%)
PCM1-N
PCM1-M
20 min
1 h
16 h
induction time
t1/2 (sec)
B
GFP-PCM1-N
splitting
fusion
kiss-and-run
Fluorescent intensity (a.u.)
C
Control
1,6-HD
RNase
PCM1
DAPI
Inset
D
Total granule volume (µm³)
Total granule intensity
E
PCM1
G3BP1
Merge DAPI
Inset
Sodium arsenite
Sodium arsenite+ 1,6-HD
Sodium arsenite+ RNase
F
Doxycycline induction
1,6-HD
fixation
2 h
15 min
16 h
G
GFP-PCM1
Centrin2
Merge DAPI
inset
2 h dox
16 h dox
H
Total granule volume (µm³)
Granule number
dox treatment:
1,6-HD:

Figure 5


A
Merge
DAPI
Centrin 2
GFP-PCM1
CEP131
MIB1
PIBF1
OFD1
CEP290
KIAA0753
CCDC14
CEP72
BBS4
0
10 min
30 min
2 h
8 h
16 h


B
Pearson correlation coefficient
0.6
0.4
0.2
Control
10 min
30 min
2 h
8 h
16 h
Induction time
CEP131
MIB1
PIBF1
CCDC14
OFD1
KIAA0753
CEP290
CEP72
BBS4

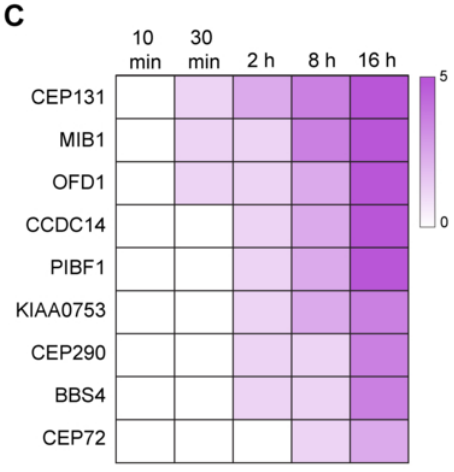
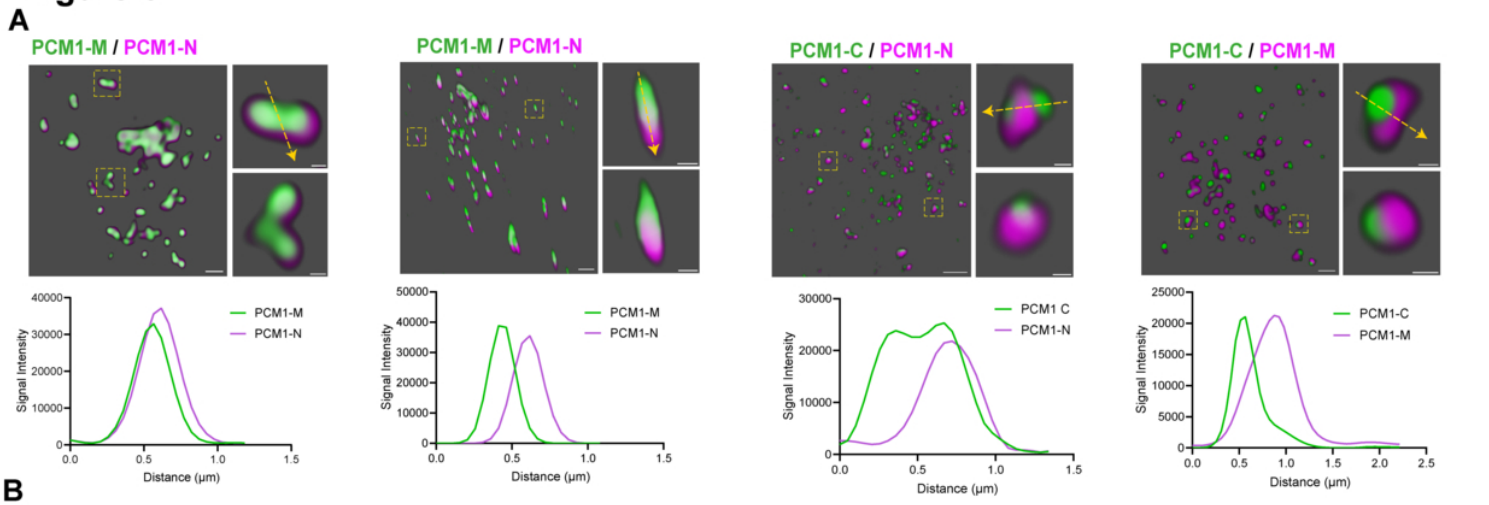
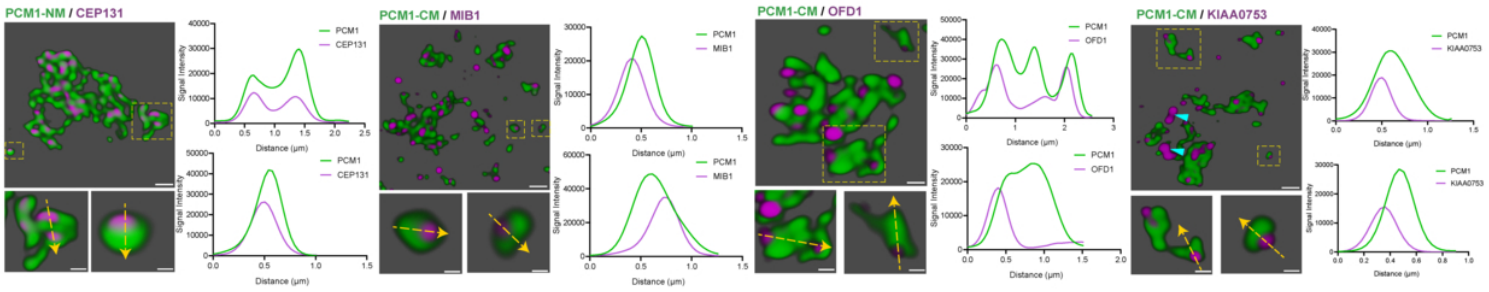
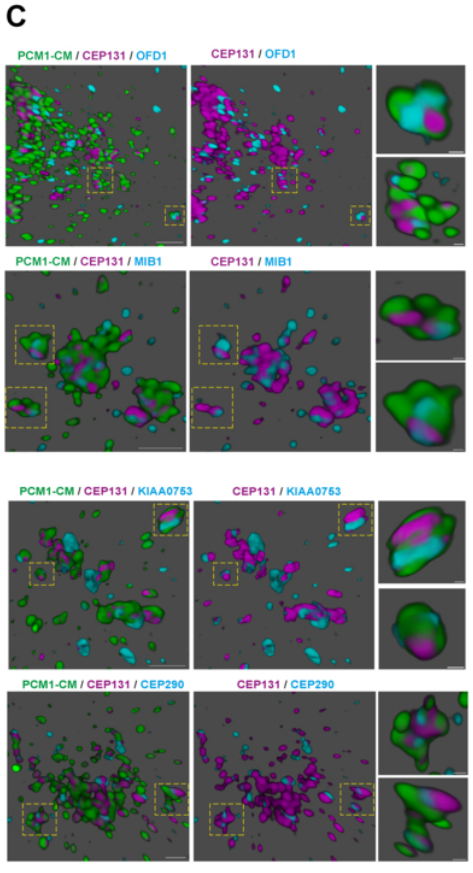
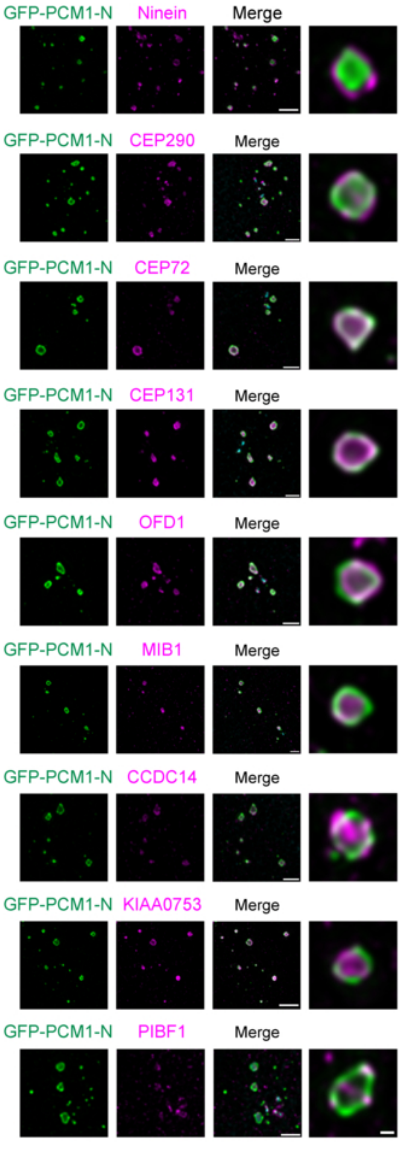

C
10 min
30 min
2 h
8 h
16 h
CEP131
MIB1
OFD1
CCDC14
PIBF1
KIAA0753
CEP290
BBS4
CEP72
5
0

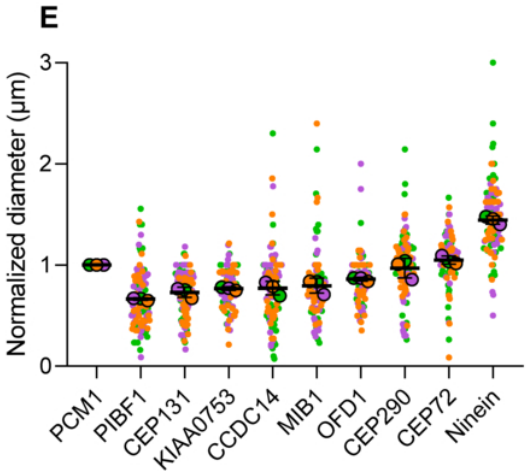
Figure 6











F

Localization	Client Protein	Relative Diameter
Inner Core	PIBF1 CEP131	0.5 - 0.75
Intermediate Core	KIAA0753 CCDC14 MIB1	0.75 - 0.80
Core-Shell Interface	OFD1	0.80 - 0.90
Shell	CEP290 CEP72	0.90 - 1.1
Reference (PCM1)	PCM1	1
Outer Shell	Ninein	1.1 - 1.5

Figure 7

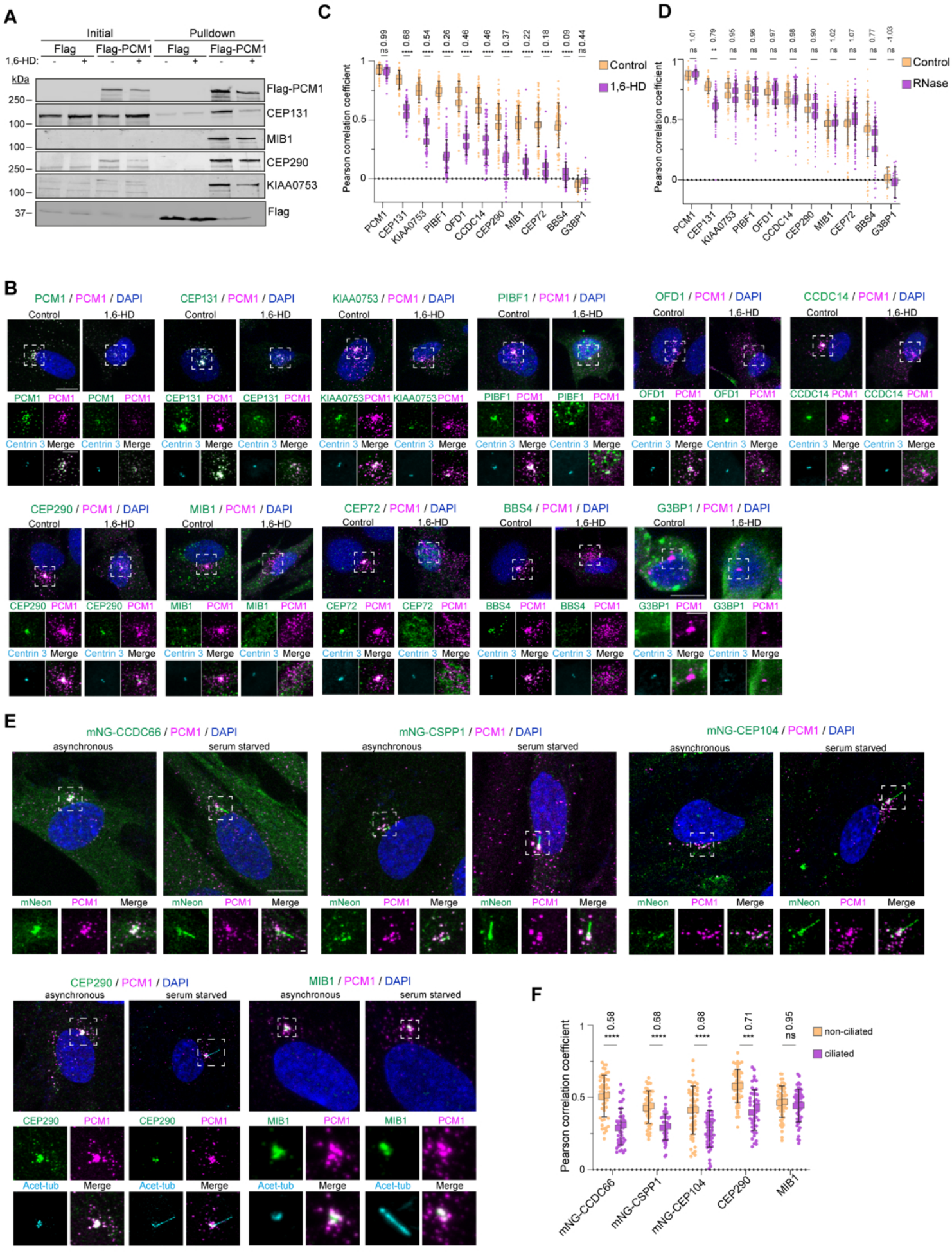

A
Initial
Pulldown
Flag
Flag-PCM1
1,6-HD:
kDa
Flag-PCM1
CEP131
MIB1
CEP290
KIAA0753
Flag
C
Pearson correlation coefficient
Control
1,6-HD
PCM1
CEP131
KIAA0753
PIBF1
OFD1
CCDC14
CEP290
MIB1
CEP72
BBS4
G3BP1
D
Pearson correlation coefficient
Control
RNase
B
PCM1 / PCM1 / DAPI
CEP131 / PCM1 / DAPI
KIAA0753 / PCM1 / DAPI
PIBF1 / PCM1 / DAPI
OFD1 / PCM1 / DAPI
CCDC14 / PCM1 / DAPI
CEP290 / PCM1 / DAPI
MIB1 / PCM1 / DAPI
CEP72 / PCM1 / DAPI
BBS4 / PCM1 / DAPI
G3BP1 / PCM1 / DAPI
Control
1,6-HD
Centrin 3
Merge
E
mNG-CCDC66 / PCM1 / DAPI
mNG-CSPP1 / PCM1 / DAPI
mNG-CEP104 / PCM1 / DAPI
asynchronous
serum starved
mNeon
PCM1
Merge
CEP290 / PCM1 / DAPI
MIB1 / PCM1 / DAPI
Acet-tub
F
Pearson correlation coefficient
non-ciliated
ciliated
mNG-CCDC66
mNG-CSPP1
mNG-CEP104
CEP290
MIB1

Figure 8

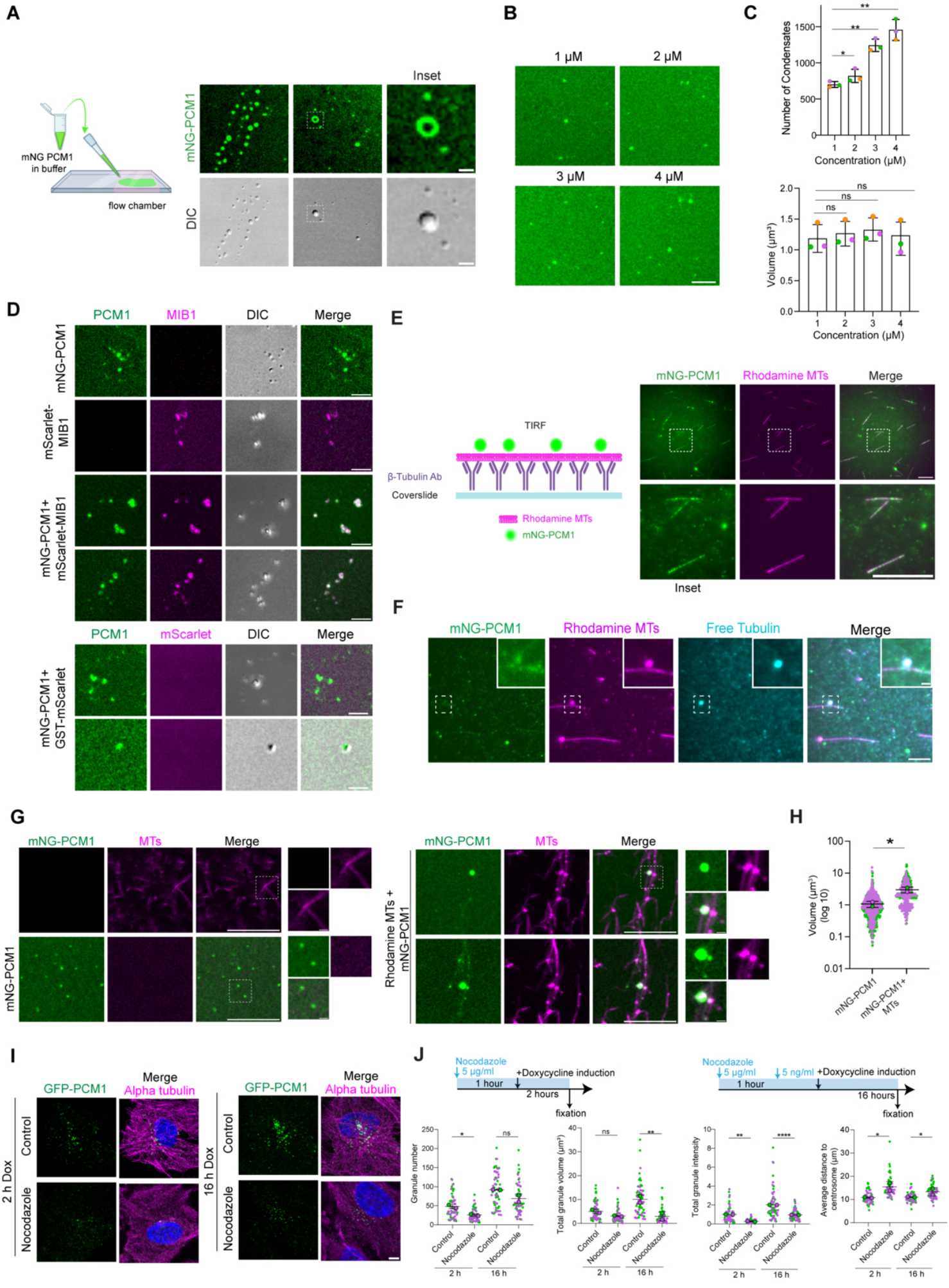

A
mNG PCM1 in buffer
flow chamber
Inset
mNG-PCM1
DIC
B
1 μM
2 μM
3 μM
4 μM
C
Number of Condensates
Concentration (μM)
Volume (μm³)
ns
D
PCM1
MIB1
DIC
Merge
mNG-PCM1
mScarlet-MIB1
mNG-PCM1+ mScarlet-MIB1
mScarlet
mNG-PCM1+ GST-mScarlet
E
TIRF
β-Tubulin Ab
Coverslide
Rhodamine MTs
mNG-PCM1
Inset
F
Free Tubulin
G
MTs
H
Volume (μm³) (log 10)
mNG-PCM1+ MTs
I
GFP-PCM1
Alpha tubulin
Control
Nocodazole
2 h Dox
16 h Dox
J
Nocodazole
5 μg/ml
5 ng/ml
+Doxycycline induction
1 hour
2 hours
16 hours
fixation
Granule number
Total granule volume (μm³)
Total granule intensity
Average distance to centrosome (μm)
2 h
16 h

Figure S1

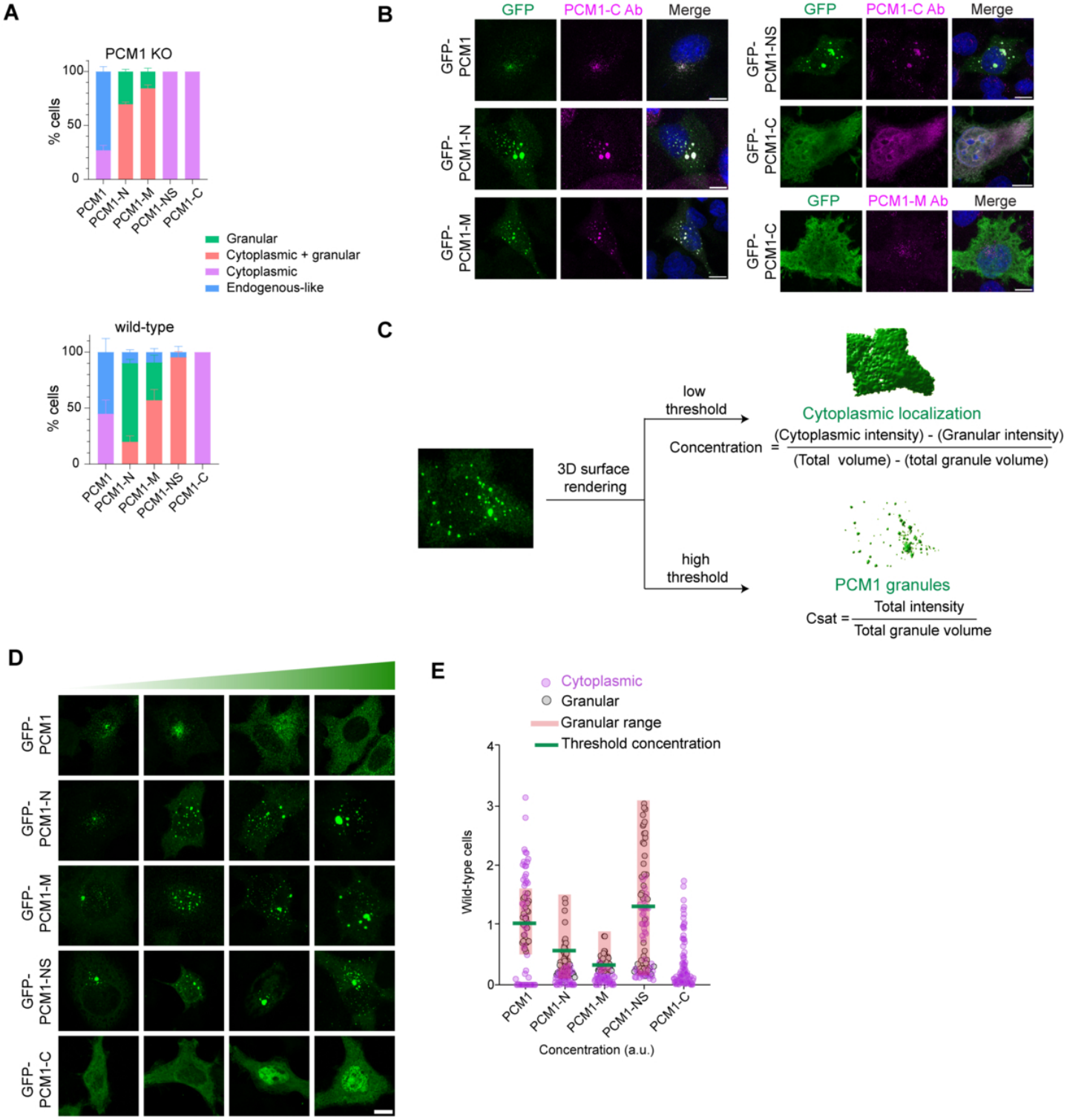

A
PCM1 KO
% cells
100
50
0
PCM1
PCM1-N
PCM1-M
PCM1-NS
PCM1-C
Granular
Cytoplasmic + granular
Cytoplasmic
Endogenous-like
wild-type
B
GFP
PCM1-C Ab
Merge
GFP-PCM1
GFP-PCM1-N
GFP-PCM1-M
GFP-PCM1-NS
GFP-PCM1-C
PCM1-M Ab
C
3D surface rendering
low threshold
high threshold
Concentration = (Cytoplasmic intensity) - (Granular intensity) / (Total volume) - (total granule volume)
Cytoplasmic localization
PCM1 granules
Csat = Total intensity / Total granule volume
D
E
Cytoplasmic
Granular
Granular range
Threshold concentration
Wild-type cells
Concentration (a.u.)

Figure S2

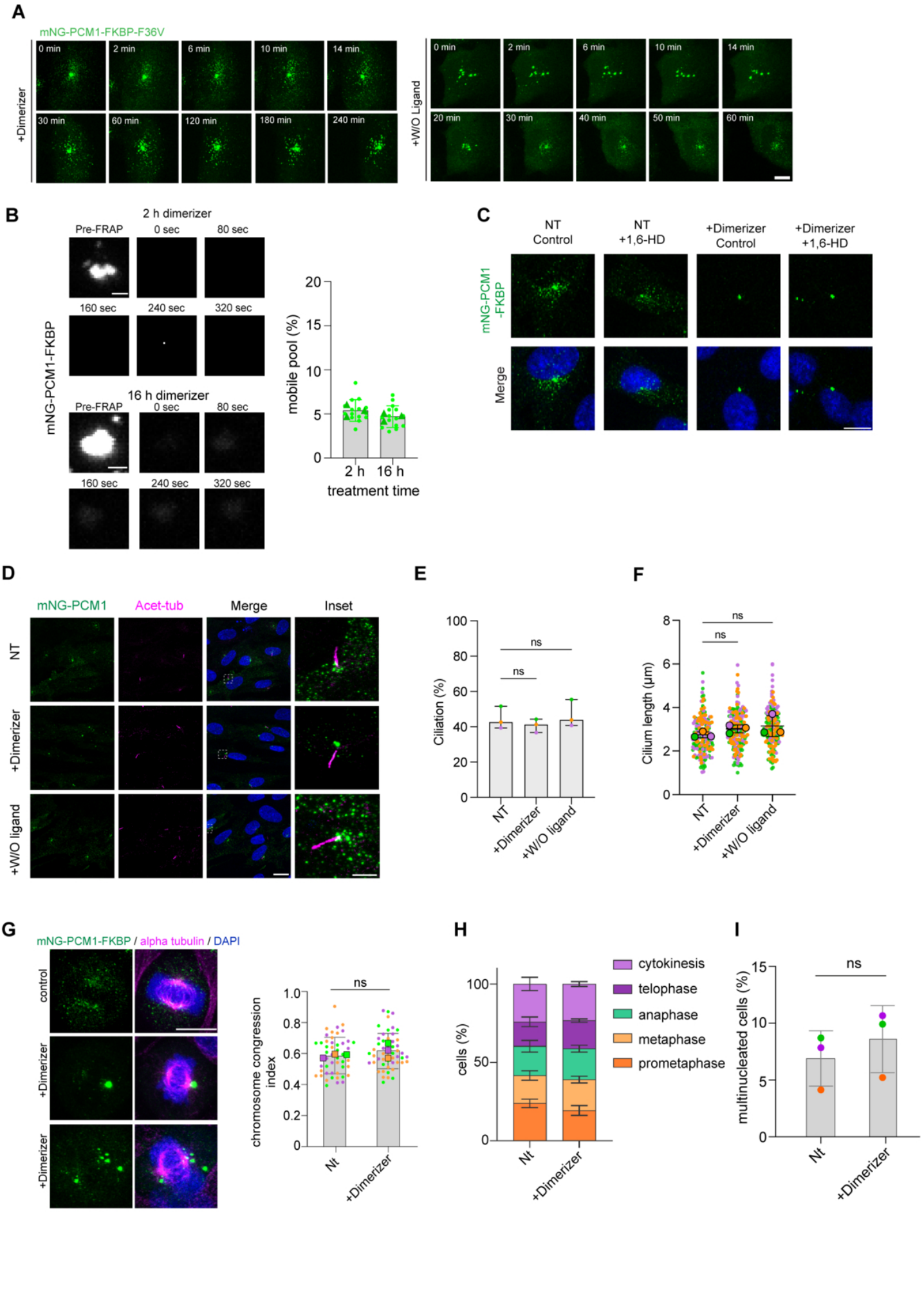

A
mNG-PCM1-FKBP-F36V
+Dimerizer
0 min
2 min
6 min
10 min
14 min
30 min
60 min
120 min
180 min
240 min
+W/O Ligand
0 min
2 min
6 min
10 min
14 min
20 min
30 min
40 min
50 min
60 min
B
2 h dimerizer
Pre-FRAP
0 sec
80 sec
160 sec
240 sec
320 sec
16 h dimerizer
Pre-FRAP
0 sec
80 sec
160 sec
240 sec
320 sec
mNG-PCM1-FKBP
mobile pool (%)
20
15
10
5
0
2 h
16 h
treatment time
C
NT Control
NT +1,6-HD
+Dimerizer Control
+Dimerizer +1,6-HD
mNG-PCM1 -FKBP
Merge
D
mNG-PCM1
Acet-tub
Merge
Inset
NT
+Dimerizer
+W/O ligand
E
Ciliation (%)
100
80
60
40
20
0
ns
ns
NT
+Dimerizer
+W/O ligand
F
Cilium length (µm)
8
6
4
2
0
ns
ns
NT
+Dimerizer
+W/O ligand
G
mNG-PCM1-FKBP / alpha tubulin / DAPI
control
+Dimerizer
+Dimerizer
chromosome congression index
1.0
0.8
0.6
0.4
0.2
0
ns
Nt
+Dimerizer
H
cells (%)
100
50
0
cytokinesis
telophase
anaphase
metaphase
prometaphase
Nt
+Dimerizer
I
multinucleated cells (%)
15
10
5
0
ns
Nt
+Dimerizer

Figure S3

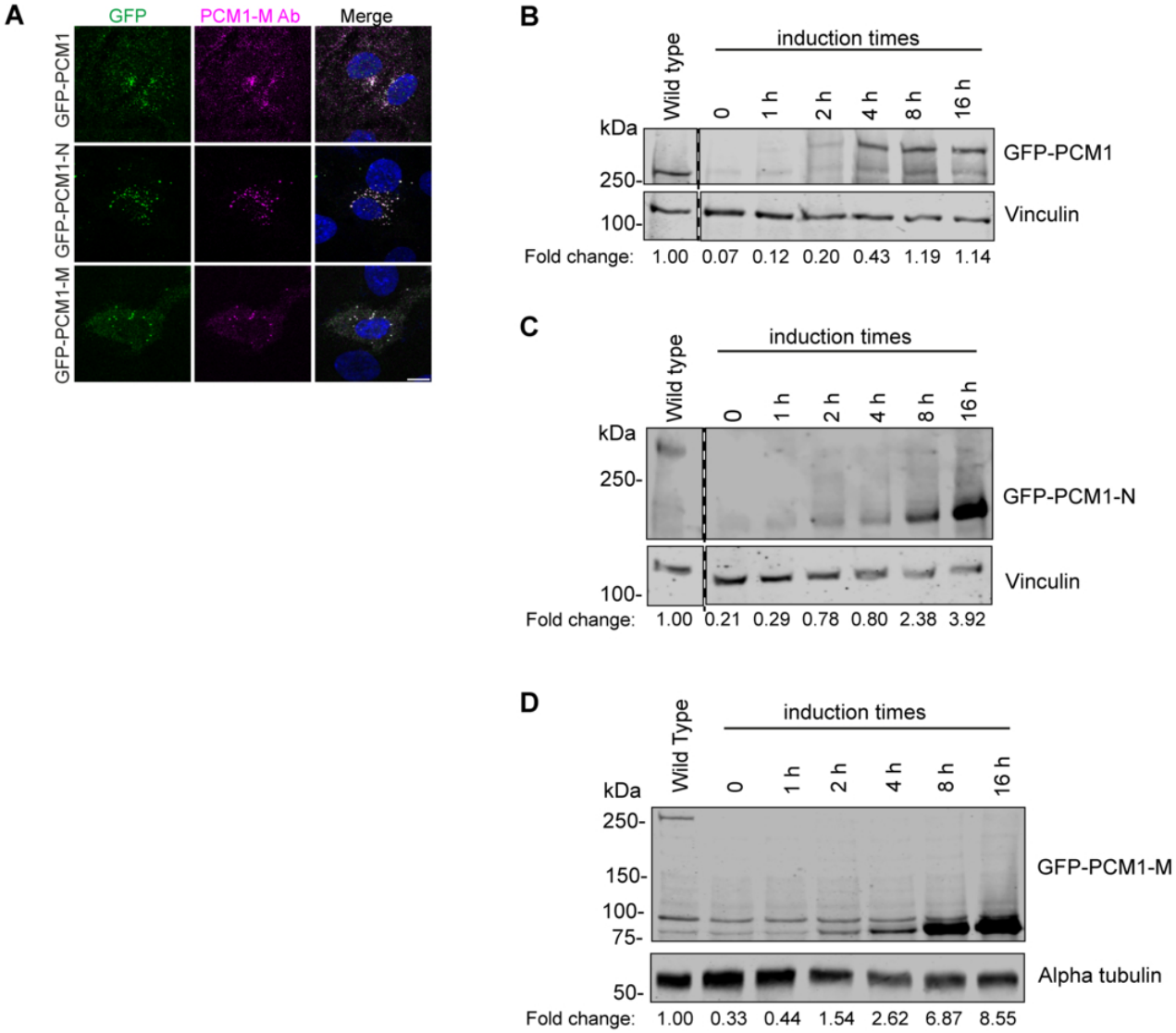

A
GFP
PCM1-M Ab
Merge
GFP-PCM1
GFP-PCM1-N
GFP-PCM1-M
B
induction times
Wild type
0
1 h
2 h
4 h
8 h
16 h
kDa
250-
100-
GFP-PCM1
Vinculin
Fold change: 1.00 0.07 0.12 0.20 0.43 1.19 1.14
C
induction times
Wild type
0
1 h
2 h
4 h
8 h
16 h
kDa
250-
100-
GFP-PCM1-N
Vinculin
Fold change: 1.00 0.21 0.29 0.78 0.80 2.38 3.92
D
induction times
Wild Type
0
1 h
2 h
4 h
8 h
16 h
kDa
250-
150-
100-
75-
50-
GFP-PCM1-M
Alpha tubulin
Fold change: 1.00 0.33 0.44 1.54 2.62 6.87 8.55

Figure S4

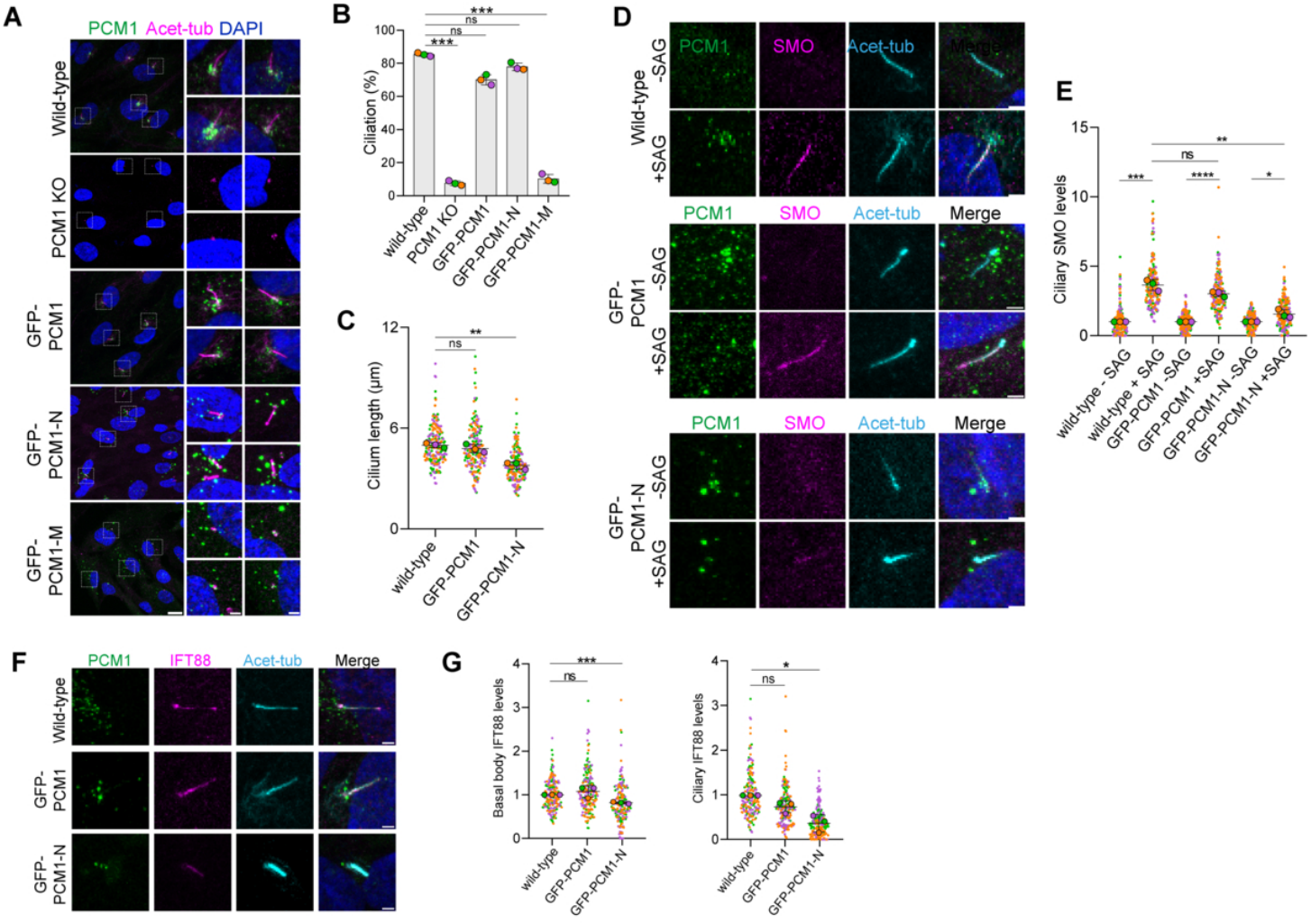

A
PCM1 Acet-tub DAPI
Wild-type
PCM1 KO
GFP-PCM1
GFP-PCM1-N
GFP-PCM1-M
B
Ciliation (%)
wild-type
PCM1 KO
GFP-PCM1
GFP-PCM1-N
GFP-PCM1-M
C
Cilium length (μm)
wild-type
GFP-PCM1
GFP-PCM1-N
D
PCM1
SMO
Acet-tub
Merge
Wild-type -SAG
Wild-type +SAG
GFP-PCM1 -SAG
GFP-PCM1 +SAG
GFP-PCM1-N -SAG
GFP-PCM1-N +SAG
E
Ciliary SMO levels
wild-type - SAG
wild-type + SAG
GFP-PCM1 -SAG
GFP-PCM1 +SAG
GFP-PCM1-N -SAG
GFP-PCM1-N +SAG
F
PCM1
IFT88
Acet-tub
Merge
Wild-type
GFP-PCM1
GFP-PCM1-N
G
Basal body IFT88 levels
Ciliary IFT88 levels
wild-type
GFP-PCM1
GFP-PCM1-N

Figure S5

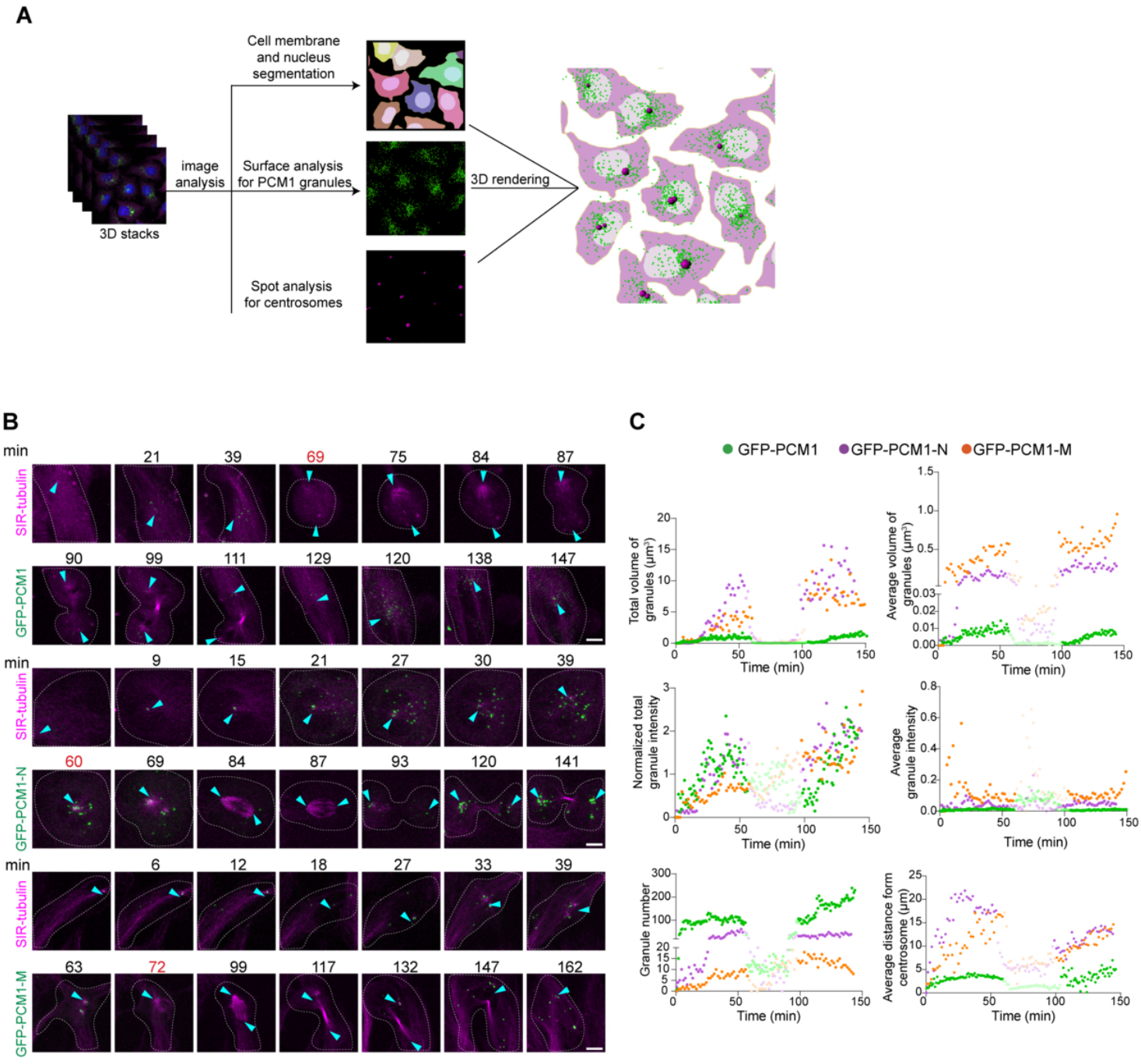
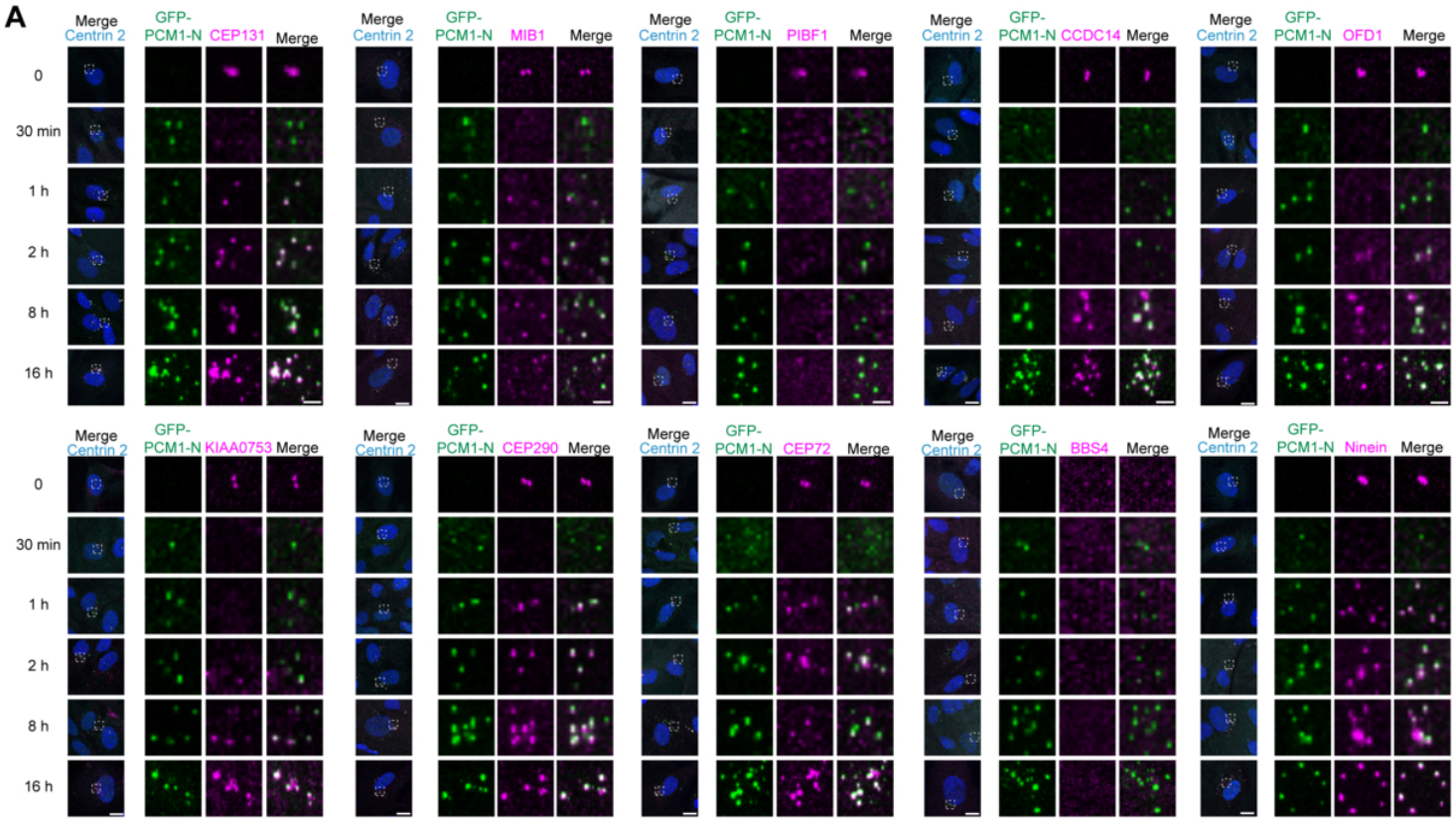
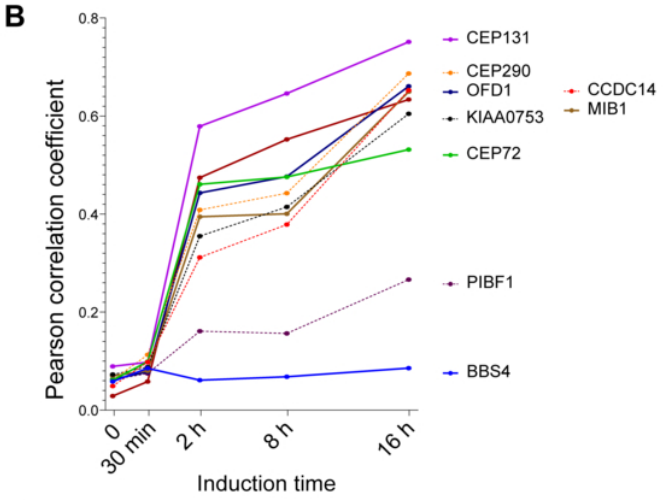
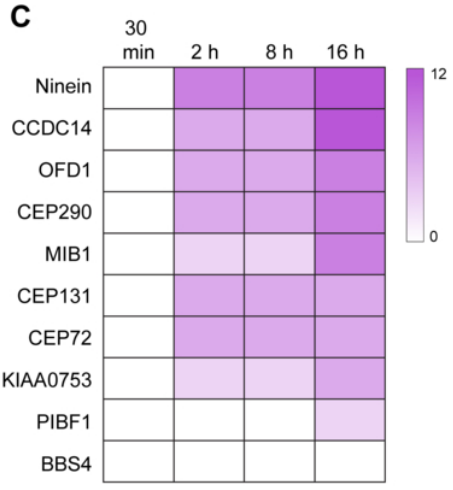

A
Cell membrane and nucleus segmentation
image analysis
Surface analysis for PCM1 granules
Spot analysis for centrosomes
3D stacks
3D rendering
B
min
SIR-tubulin
GFP-PCM1
GFP-PCM1-N
GFP-PCM1-M
C
GFP-PCM1
GFP-PCM1-N
GFP-PCM1-M
Total volume of granules (μm³)
Average volume of granules (μm³)
Normalized total granule intensity
Average granule intensity
Granule number
Average distance form centrosome (μm)
Time (min)

Figure S6


A
Merge
Centrin 2
GFP-
PCM1-N
CEP131
MIB1
PIBF1
CCDC14
OFD1
KIAA0753
CEP290
CEP72
BBS4
Ninein
0
30 min
1 h
2 h
8 h
16 h


B
Pearson correlation coefficient
0.0
0.2
0.4
0.6
0.8
0
30 min
2 h
8 h
16 h
Induction time
CEP131
CEP290
OFD1
KIAA0753
CEP72
PIBF1
BBS4
CCDC14
MIB1


C
30 min
2 h
8 h
16 h
Ninein
CCDC14
OFD1
CEP290
MIB1
CEP131
CEP72
KIAA0753
PIBF1
BBS4
12
0

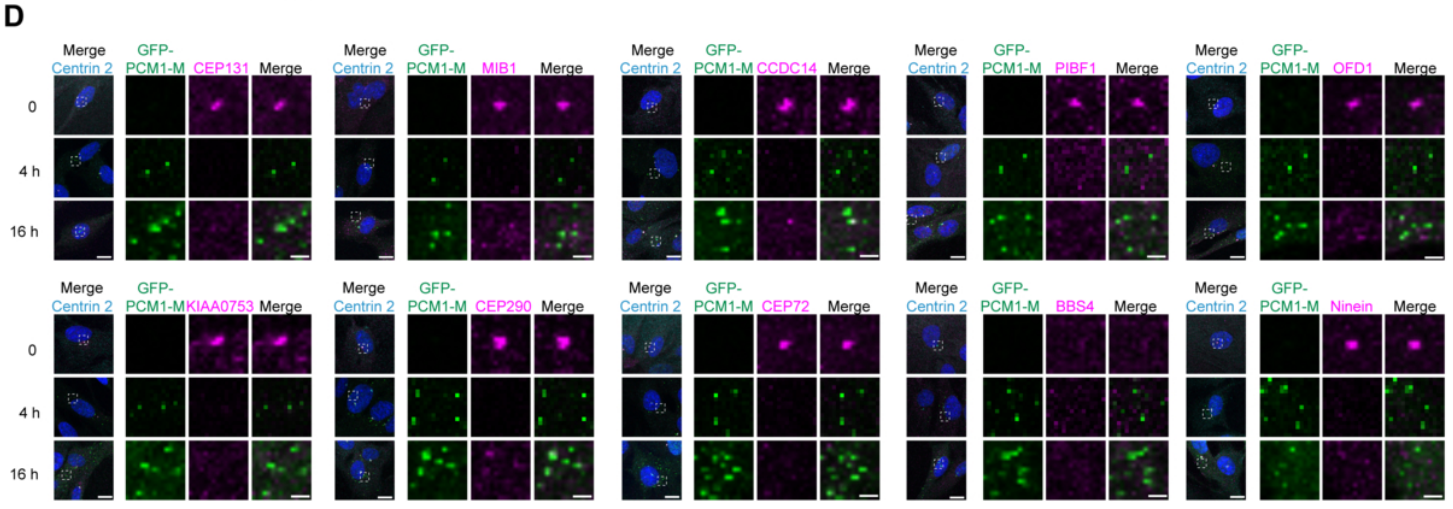
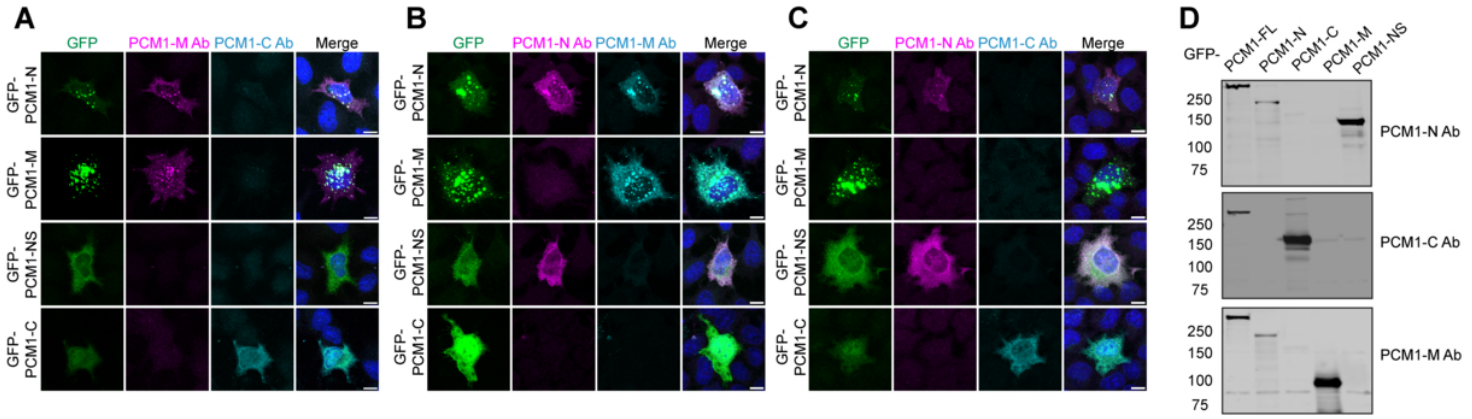
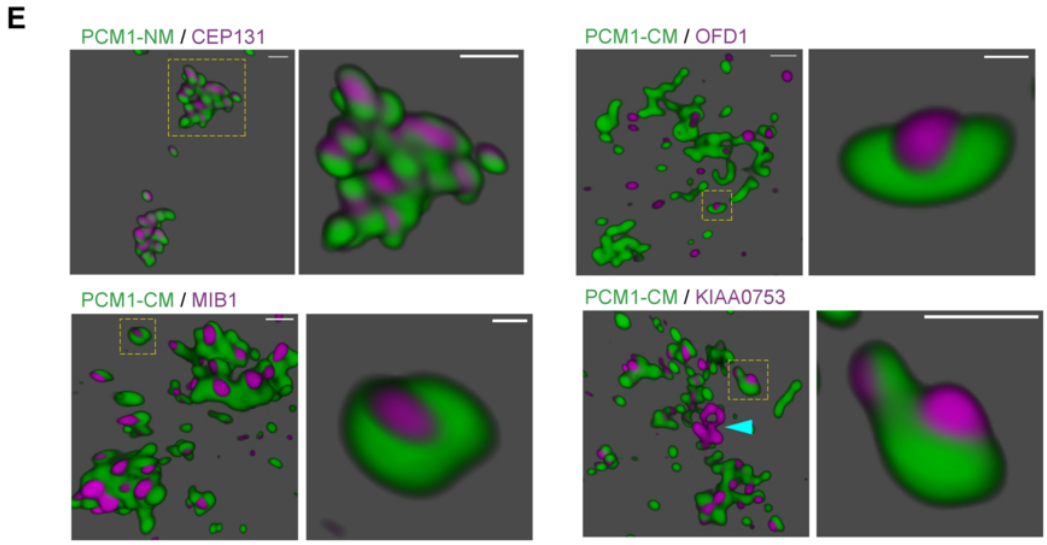

D
Merge
Centrin 2
GFP-
PCM1-M
CEP131
MIB1
CCDC14
PIBF1
OFD1
KIAA0753
CEP290
CEP72
BBS4
Ninein
0
4 h
16 h

Figure S7


A
GFP
PCM1-M Ab
PCM1-C Ab
Merge
GFP-PCM1-N
GFP-PCM1-M
GFP-PCM1-NS
GFP-PCM1-C
B
GFP
PCM1-N Ab
PCM1-M Ab
Merge
GFP-PCM1-N
GFP-PCM1-M
GFP-PCM1-NS
GFP-PCM1-C
C
GFP
PCM1-N Ab
PCM1-C Ab
Merge
GFP-PCM1-N
GFP-PCM1-M
GFP-PCM1-NS
GFP-PCM1-C
D
GFP-
PCM1-FL
PCM1-N
PCM1-C
PCM1-M
PCM1-NS
250
150
100
75
PCM1-N Ab
PCM1-C Ab
PCM1-M Ab


E
PCM1-NM / CEP131
PCM1-CM / OFD1
PCM1-CM / MIB1
PCM1-CM / KIAA0753

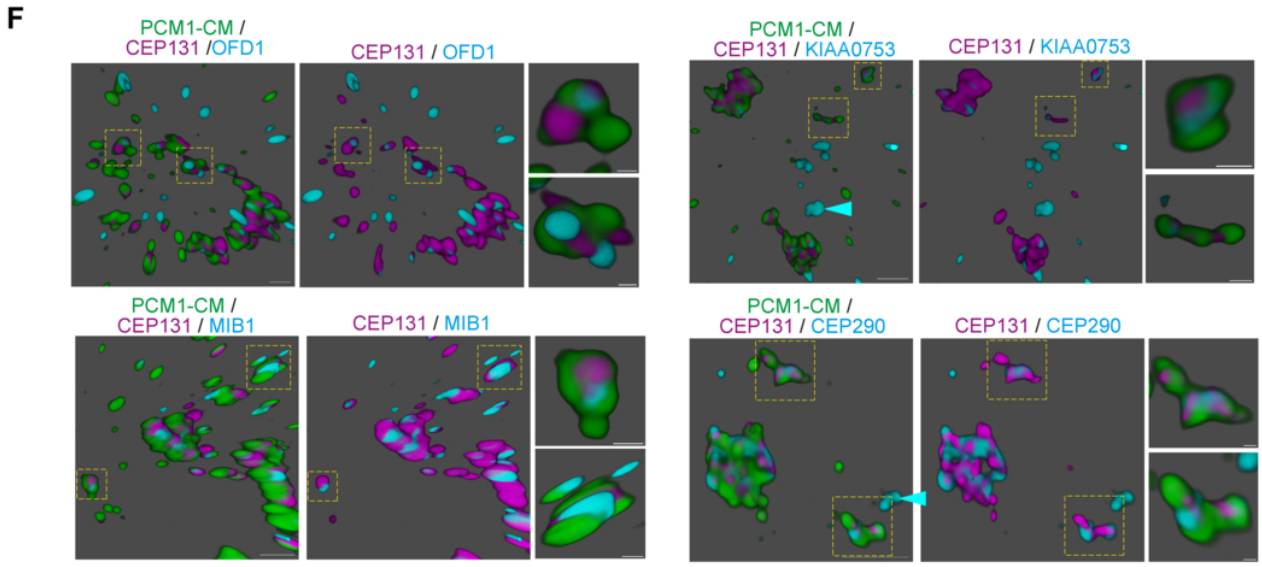

F
PCM1-CM / CEP131 /OFD1
CEP131 / OFD1
PCM1-CM / CEP131 / KIAA0753
CEP131 / KIAA0753
PCM1-CM / CEP131 / MIB1
CEP131 / MIB1
PCM1-CM / CEP131 / CEP290
CEP131 / CEP290

Figure S8

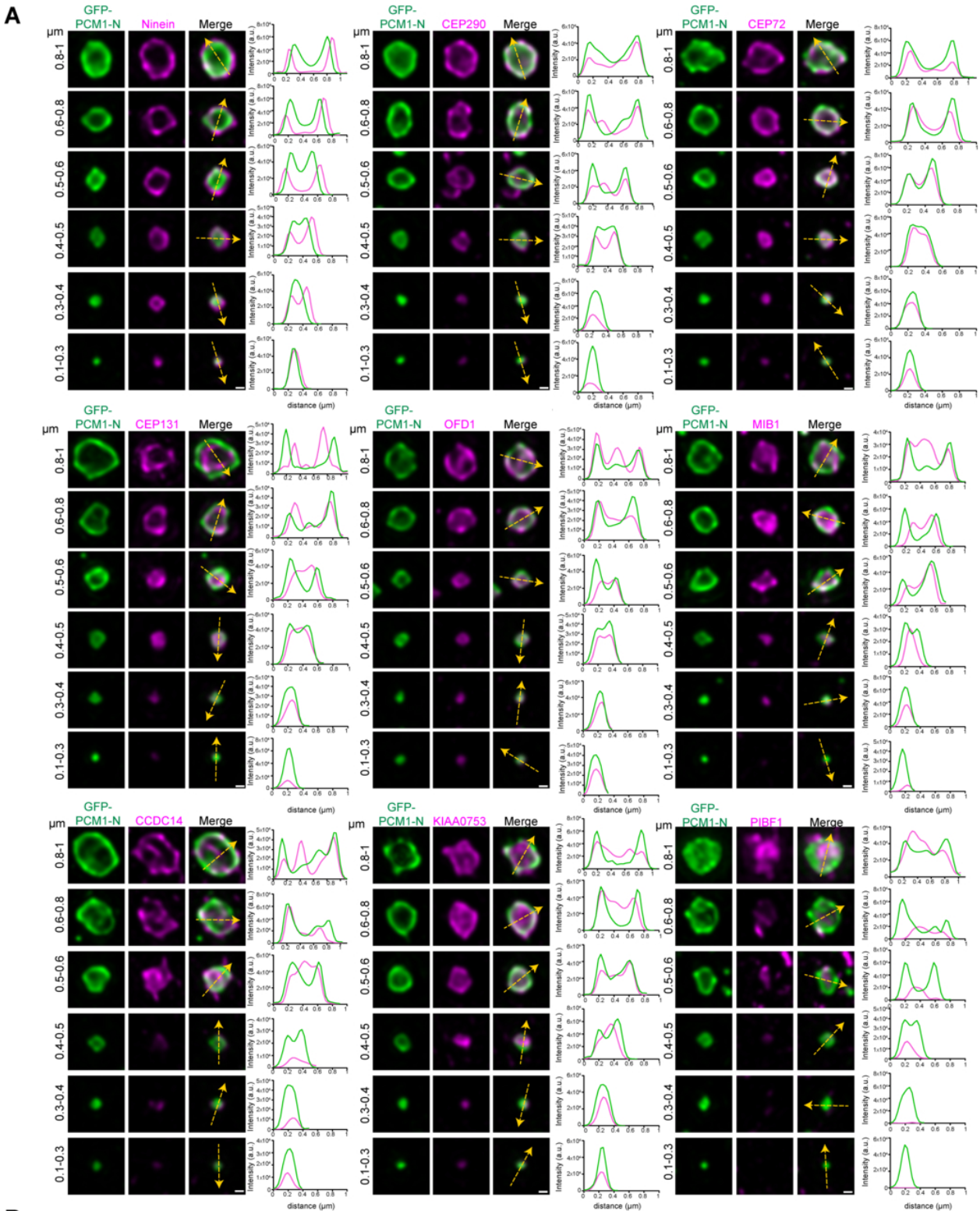
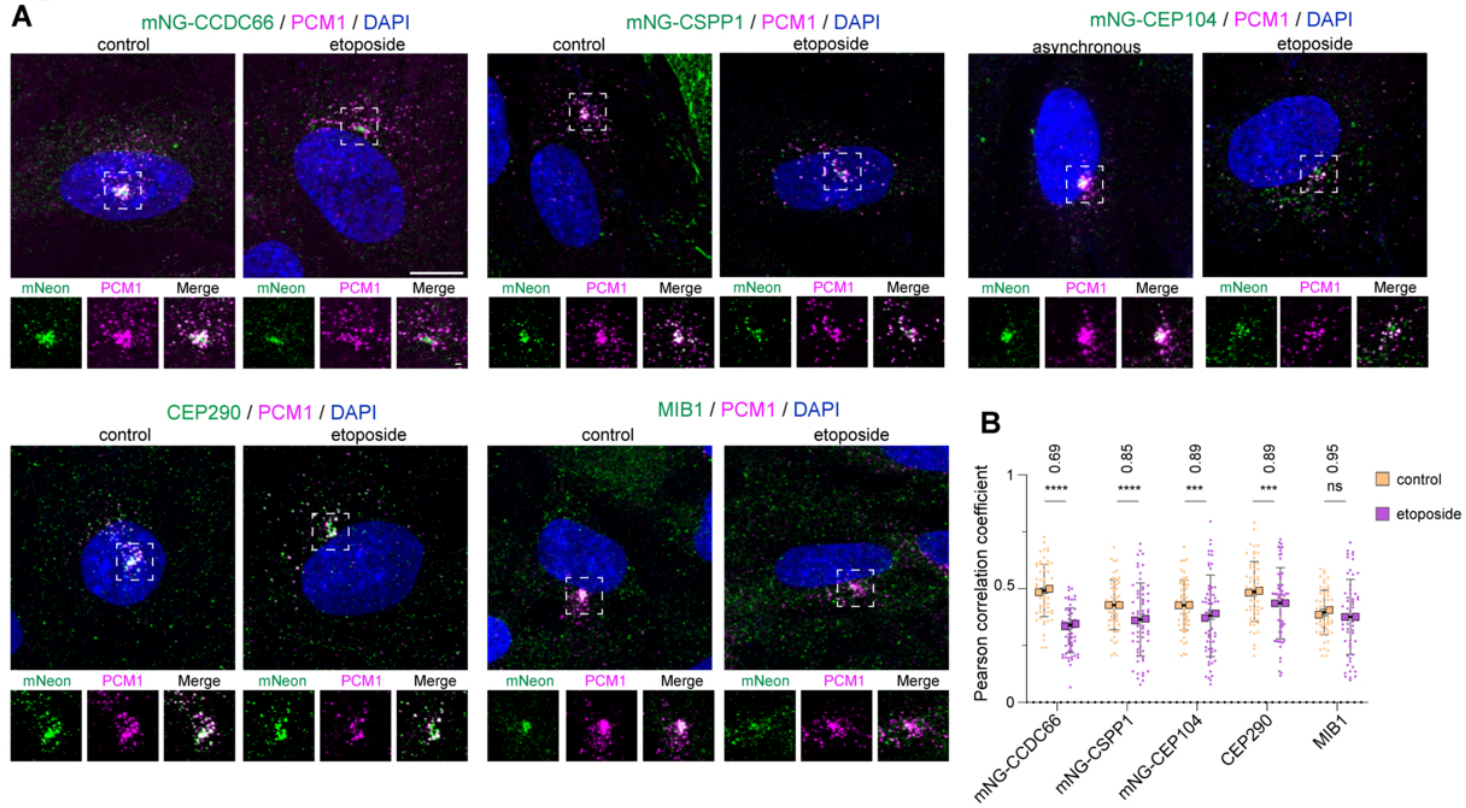
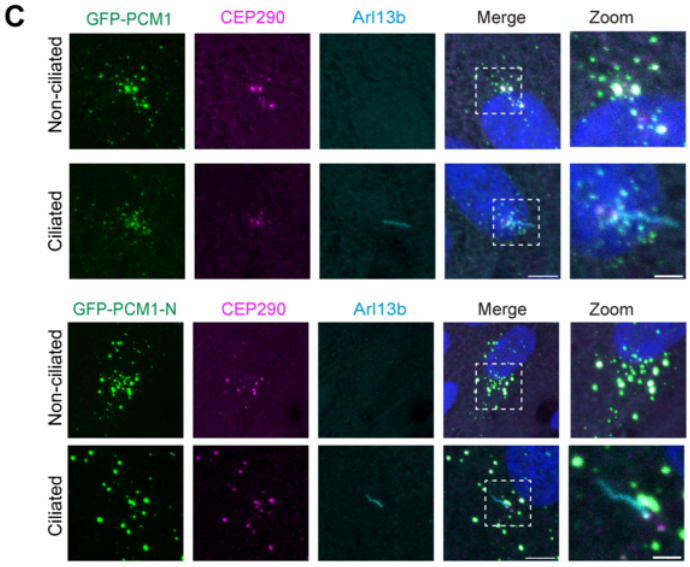
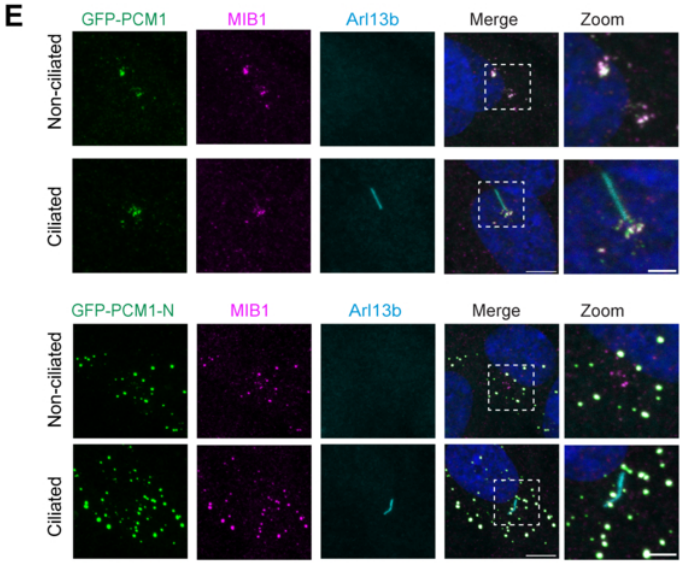

A
GFP-PCM1-N
Ninein
CEP290
CEP72
CEP131
OFD1
MIB1
CCDC14
KIAA0753
PIBF1
Merge
μm
0.8-1
0.6-0.8
0.5-0.6
0.4-0.5
0.3-0.4
0.1-0.3
Intensity (a.u.)
distance (μm)
B
Induction Time
30 min
1 h
2 h
4 h
8 h
16 h
PCM1
Ninein
Signal Intensity
Distance

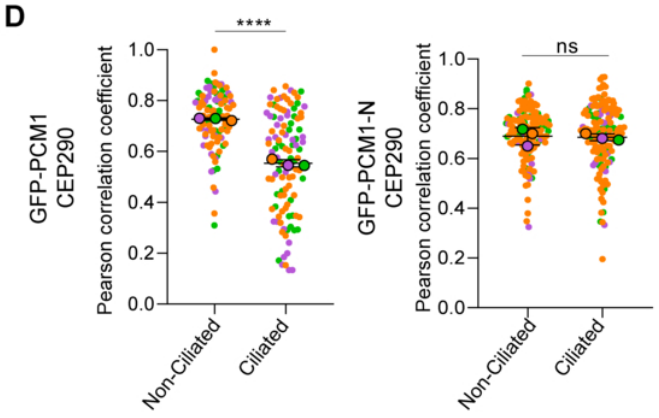
Figure S9


A
mNG-CCDC66 / PCM1 / DAPI
control
etoposide
mNG-CSPP1 / PCM1 / DAPI
control
etoposide
mNG-CEP104 / PCM1 / DAPI
asynchronous
etoposide
mNeon
PCM1
Merge
CEP290 / PCM1 / DAPI
control
etoposide
MIB1 / PCM1 / DAPI
control
etoposide

B
Pearson correlation coefficient
0.69
0.85
0.89
0.89
0.95
****
****
***
***
ns
control
etoposide
mNG-CCDC66
mNG-CSPP1
mNG-CEP104
CEP290
MIB1


C
GFP-PCM1
CEP290
Arl13b
Merge
Zoom
Non-ciliated
Ciliated
GFP-PCM1-N


E
GFP-PCM1
MIB1
Arl13b
Merge
Zoom
Non-ciliated
Ciliated
GFP-PCM1-N


D
GFP-PCM1
CEP290
Pearson correlation coefficient
****
ns
Non-Ciliated
Ciliated
GFP-PCM1-N
CEP290

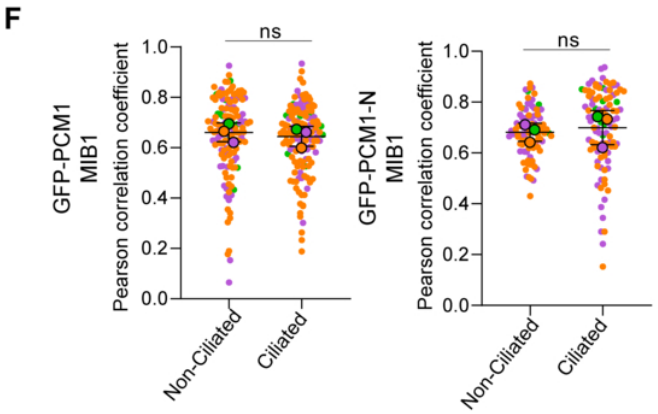
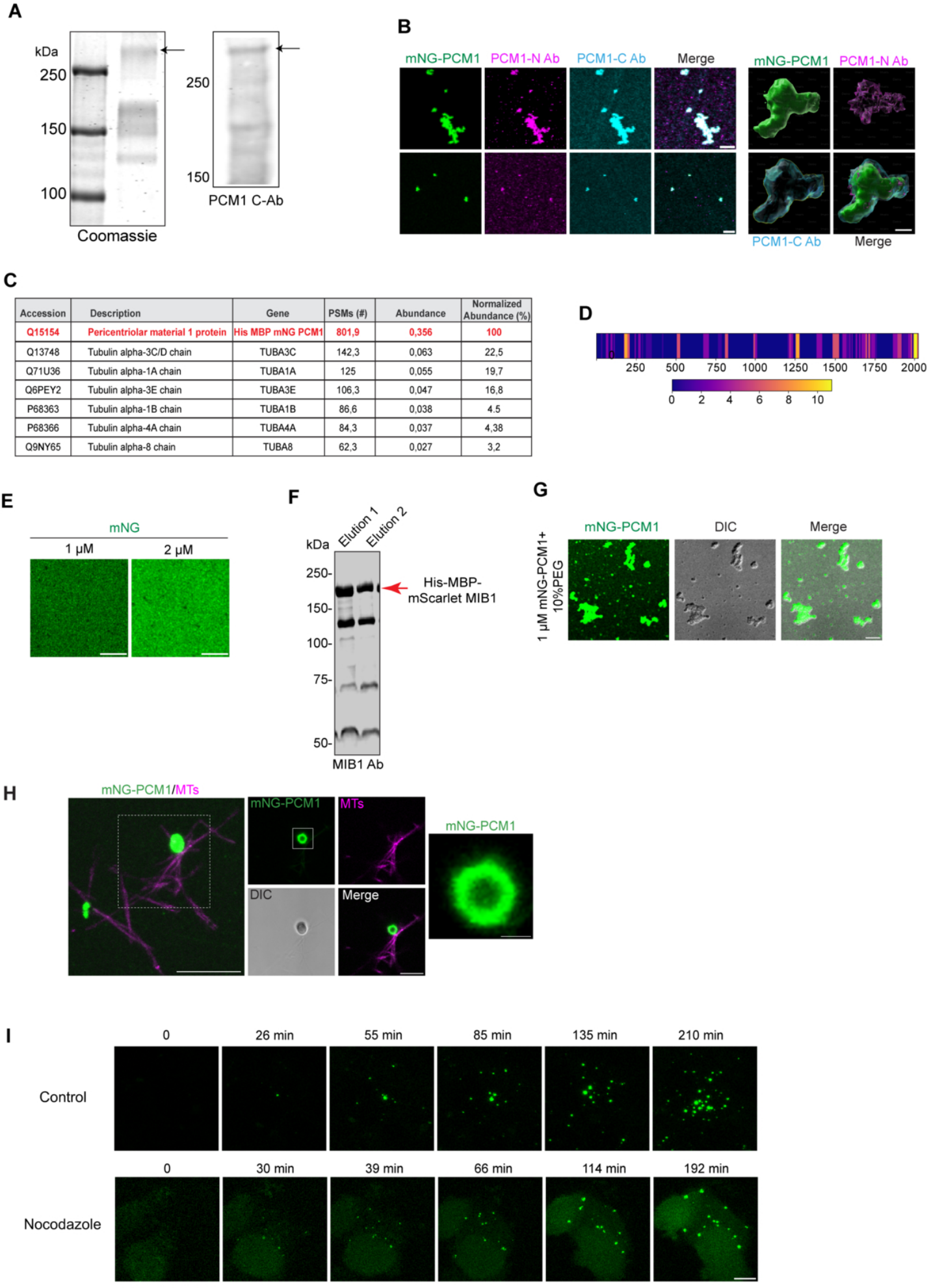

F
GFP-PCM1
MIB1
Pearson correlation coefficient
ns
Non-Ciliated
Ciliated
GFP-PCM1-N
MIB1

Figure S10



C

Accession	Description	Gene	PSMs (#)	Abundance	Normalized Abundance (%)
Q15154	Pericentriolar material 1 protein	His MBP mNG PCM1	801,9	0,356	100
Q13748	Tubulin alpha-3C/D chain	TUBA3C	142,3	0,063	22,5
Q71U36	Tubulin alpha-1A chain	TUBA1A	125	0,055	19,7
Q6PEY2	Tubulin alpha-3E chain	TUBA3E	106,3	0,047	16,8
P68363	Tubulin alpha-1B chain	TUBA1B	86,6	0,038	4.5
P68366	Tubulin alpha-4A chain	TUBA4A	84,3	0,037	4,38
Q9NY65	Tubulin alpha-8 chain	TUBA8	62,3	0,027	3,2